





This is to certify that the  
dissertation entitled

STUDY OF PROXIMITY-INDUCED SPIN-TRIPLET PAIR  
CORRELATIONS IN FERROMAGNETIC JOSEPHSON  
JUNCTIONS

presented by

Trupti S. Khaire

has been accepted towards fulfillment  
of the requirements for the

Ph.D. degree in Physics and Astronomy

*Norman O. Bize*

Major Professor's Signature

*June 24, 2010*

Date

**PLACE IN RETURN BOX** to remove this checkout from your record.  
**TO AVOID FINES** return on or before date due.  
**MAY BE RECALLED** with earlier due date if requested.

DATE DUE	DATE DUE	DATE DUE

STUDY OF PROXIMITY-INDUCED SPIN-TRIPLET PAIR CORRELATIONS IN  
FERROMAGNETIC JOSEPHSON JUNCTIONS

By

Trupti S. Khaire

A DISSERTATION

Submitted to  
Michigan State University  
in partial fulfillment of the requirements  
for the degree of

DOCTOR OF PHILOSOPHY

Physics and Astronomy

2010

## ABSTRACT

### STUDY OF PROXIMITY-INDUCED SPIN-TRIPLET PAIR CORRELATIONS IN FERROMAGNETIC JOSEPHSON JUNCTIONS

By

**Trupti S. Khaire**

In conventional superconductors, superconducting correlations are due to *spin-singlet* Cooper pairs that are correlations between electrons of opposite spin, whereas ferromagnetism on the other hand favors parallel alignment of electron spins. When a superconductor is placed in contact with a ferromagnet, Cooper pairs can cross the interface into the ferromagnet. When they do so, the two electrons from the spin-singlet Cooper pair enter different spin bands and rapidly lose phase coherence over a short length scale. This is called the conventional spin-singlet proximity effect. In contrast, *spin-triplet* Cooper pairs are not subject to this constraint, and hence the spin-triplet proximity effect should extend much further into ferromagnet. The generation of spin-triplet correlations has been predicted to occur in superconducting/ferromagnetic hybrid systems, but is known to be very sensitive to the presence of magnetic inhomogeneities in the ferromagnet. The major part of this work was aimed at studying materials and conditions necessary for the generation of long range triplet correlations. Once generated, there are several factors that pose difficulty in their long-range propagation. Our major task therefore was to separate the “generation” and “propagation” of the triplet correlations in our system. All these studies implement Superconductor/Ferromagnet/Superconductor Josephson junction as a tool for the observation of the long-range effect.

We have observed a long-range spin-triplet supercurrent in S/F/S Josephson junctions containing Co(d)/Ru(0.6 nm)/Co(d) trilayers as thick as  $2d = 50$  nm. The spin-triplet pair correlations are induced only when a thin layer of Pd<sub>0.88</sub>Ni<sub>0.12</sub> alloy is placed between the central Co and outer Nb layers. The spin-triplet critical super-

current in our Josephson junctions was nearly 100 times greater than the supercurrent in similarly-prepared junctions without PdNi alloy. This provides strong evidence of long-range triplet correlations in our system.

## DEDICATION

To the reader

## ACKNOWLEDGMENT

I am thankful to many people who I have come across all these years.

I am very thankful to my advisor, Prof. Norman O. Birge for everything. I admire your systematic approach in all things professional and personal. Thanks for seeing it through all the ups and downs and the worst struggle during my primitive years. The gradual change from being there for us to letting us decide what to do next, was indeed nice.

Also, many thanks to Prof. William Pratt, Jr. your enthusiasm is always contagious. Your excitement while looking at some of my worst possible measurements, really helped me in keeping my spirits high.

Thanks to Dr. Reza Loloee for making the basement a place to learn and laugh, a second home in every sense. Thanks for helping me even during odd hours. Apart from the technical expertise, I thank Dr. Baokang Bi for helping me see the fun behind “problem-solving”.

Thanks to my senior colleagues, to Ion Moraru for introducing me to experimental techniques, and thanks to Gassem Alzoubi, the little time we overlapped was fun indeed. I would also like to thank to my current lab colleagues Mazin, Yixing, and Kurt for keeping me company. Special thanks to Yixing for the Fraunhofer-analysis program you made for us. Many thanks to my friends Sheenu, Neelam and Poonam for being there with me all these years. And special thanks to my best friend - my Mom.

Thanks to Machine shop personnel Tom Palazzolo, Jim Muns and Tom Hudson. I also thank the Keck Microfabrication Facility for its extensive use in our sample fabrication process. This work was supported by DOE grant DE-FG02-06ER46341.

# TABLE OF CONTENTS

<b>List of Tables</b> . . . . .	ix
<b>List of Figures</b> . . . . .	x
<b>1 Introduction</b> . . . . .	<b>1</b>
1.1 Proximity Induced Odd Triplet Superconductivity . . . . .	2
1.2 This Work . . . . .	3
<b>2 Theoretical Background</b> . . . . .	<b>5</b>
2.1 Superconductivity . . . . .	5
2.1.1 London Penetration Depth . . . . .	6
2.2 Proximity effect . . . . .	7
2.2.1 Superconductor/Normal metal (S/N) . . . . .	7
2.2.2 Superconductor/Ferromagnet (S/F) . . . . .	9
2.3 Short Range Correlations . . . . .	11
2.4 Long Range Triplet Correlations (LRTC) . . . . .	12
2.4.1 What are LRTCs? . . . . .	12
2.4.2 A Simplified Picture of Triplet Generation Mechanism . . . . .	13
2.4.3 Previous Experimental Hints of LRTC . . . . .	17
2.4.4 Ways to induce LRTC in S/F Systems . . . . .	18
2.4.5 Ways to detect LRTC . . . . .	19
2.5 Theoretical Predictions for LRTC . . . . .	19
2.6 Josephson Junctions . . . . .	21
2.6.1 Definition . . . . .	21
2.6.2 Resistively Shunted Junction (RCSJ) . . . . .	23
2.6.3 Effect of Magnetic Field . . . . .	27
2.6.4 Josephson Penetration Depth . . . . .	30
2.7 Ferromagnetic $0-\pi$ Josephson Junctions . . . . .	30
2.8 Domain Structure of Ferromagnetic Interlayer . . . . .	32
2.9 Our Approach . . . . .	35
<b>3 Experimental Methods</b> . . . . .	<b>37</b>
3.1 Sample Fabrication . . . . .	37
3.1.1 Sputtering . . . . .	38
3.1.2 Photolithography . . . . .	42
3.1.3 Ion Milling . . . . .	43
3.1.4 $\text{SiO}_x$ Deposition . . . . .	44
3.1.5 Liftoff . . . . .	45

3.1.6	Top Leads . . . . .	45
3.2	Fabrication Issues . . . . .	46
3.2.1	Undercut . . . . .	46
3.2.2	Back Sputtering . . . . .	47
3.2.3	Dust particles . . . . .	48
3.3	Reactive Ion Etching (RIE) . . . . .	48
3.4	Magnetic Force Microscopy (MFM) . . . . .	50
3.5	Measurements . . . . .	52
3.5.1	Energy Dispersive X-ray Spectroscopy (EDS) . . . . .	52
3.5.2	Magnetic Measurements . . . . .	53
3.5.3	Resistivity Measurements . . . . .	54
3.5.4	Temperature Variation Measurements . . . . .	56
<b>4</b>	<b>Spin-Singlet Superconductivity . . . . .</b>	<b>59</b>
4.1	CuNi Josephson Junctions: (Nb/CuNi/Nb) . . . . .	59
4.1.1	Characterization of CuNi Josephson Junctions . . . . .	59
4.1.2	Magnetizing CuNi Josephson Junctions . . . . .	61
4.1.3	Disadvantages of CuNi Alloy . . . . .	63
4.2	PdNi Josephson Junctions (Nb/PdNi/Nb) . . . . .	64
4.2.1	Characterization of PdNi Alloy . . . . .	65
4.2.2	Characterization of PdNi Josephson Junctions . . . . .	67
4.2.3	Magnetizing PdNi Josephson Junctions . . . . .	70
4.2.4	Critical Current vs Thickness: $0 - \pi$ Josephson Junction . . . . .	72
4.2.5	Resistivity of PdNi . . . . .	74
4.3	Theoretical Analysis of PdNi Josephson Junctions . . . . .	76
4.4	Discussion of Results . . . . .	78
4.4.1	Estimate of Mean Free Path in PdNi . . . . .	78
4.4.2	Estimate of Exchange Energy in PdNi . . . . .	79
4.4.3	Comparison to Other Experiments . . . . .	79
4.4.4	$0 - \pi$ Josephson Junction: Temperature Dependence . . . . .	80
4.5	No Sign of LRTC! . . . . .	84
4.6	Conclusion . . . . .	85
<b>5</b>	<b>GMR Experiments . . . . .</b>	<b>87</b>
5.1	Magnetoresistance (MR) . . . . .	87
5.2	GMR Theory . . . . .	87
5.2.1	Simplified GMR Model . . . . .	88
5.2.2	Two-Current Series-Resistor Model (2CSR) . . . . .	90
5.3	Spin Diffusion Length in PdNi Alloy . . . . .	94
5.3.1	Spin Valves: Py/Cu/PdNi . . . . .	94
5.3.2	Spin Valves (Spoiler Geometry) . . . . .	98
5.3.3	Discussion of the Results . . . . .	100
5.3.4	Strong spin orbit coupling in PdNi alloy . . . . .	101
5.4	Spin Diffusion Length in PdFe . . . . .	103

5.4.1	Characterization of PdFe Alloy . . . . .	104
5.4.2	Magnetic Anisotropy . . . . .	104
5.4.3	Double Exchange Biased Spin Valves . . . . .	106
5.4.4	Discussion of Results . . . . .	107
<b>6</b>	<b>Spin-Triplet Superconductivity . . . . .</b>	<b>109</b>
6.1	Ferromagnetic Josephson Junctions using Ni . . . . .	110
6.2	Reduction of Flux . . . . .	113
6.3	Synthetic Antiferromagnet (SAF) . . . . .	115
6.3.1	Josephson Junctions using SAF of the form Co/Ru/Co . . . . .	116
6.3.2	Other Experiments using SAF Configuration . . . . .	119
6.4	Long-Range Triplet Correlations in Our Experiment . . . . .	121
6.4.1	Strength of Triplet Correlations . . . . .	127
6.4.2	Where are the Triplets Generated? . . . . .	129
6.4.3	Temperature Dependence of the Triplet Samples . . . . .	130
6.4.4	Discussion of the Results . . . . .	131
6.4.4.1	Comparison between Theory and Experiment . . . . .	131
6.4.4.2	Confirmation of Triplet Correlations . . . . .	133
<b>7</b>	<b>Discussion and Further Work . . . . .</b>	<b>135</b>
7.1	Our Aim . . . . .	135
7.2	Overview of Our Work . . . . .	136
7.3	Future Directions . . . . .	137
7.4	A Year of Triplet Correlations! . . . . .	139
<b>A</b>	<b>Appendices . . . . .</b>	<b>140</b>
A.1	Photolithography Recipes . . . . .	140
A.1.1	Single Layer Photolithography . . . . .	141
A.1.2	Bilayer Photolithography . . . . .	142
A.1.3	Trilayer Photolithography . . . . .	143
A.1.4	Image Reversal Photolithography . . . . .	144
	<b>Bibliography . . . . .</b>	<b>147</b>
	<b>Bibliography . . . . .</b>	<b>147</b>

## LIST OF TABLES

2.1	Exchange symmetry for 2-particle fermionic correlation function . . .	13
4.1	Summary of PdNi parameters, $v_F$ , $\rho l_e$ , $\rho$ and $l_e$ . . . . .	80
4.2	Summary of PdNi parameters $\xi_{F1}$ , $\xi_{F2}$ , $E_{ex}$ and $T_{Curie}$ . . . . .	81

## LIST OF FIGURES

Images in this dissertation are presented in color

2.1	Andreev Reflection . . . . .	7
2.2	Simplistic electron dispersion explanation . . . . .	9
2.3	Triplet generation mechanism . . . . .	14
2.4	Equivalent circuit of RCSJ model . . . . .	24
2.5	Tilted washboard potential . . . . .	26
2.6	Underdamped and Overdamped Josephson junctions . . . . .	27
2.7	Josephson junction schematic . . . . .	28
2.8	Airy pattern for circular Josephson junction . . . . .	30
2.9	$0 - \pi$ Josephson junctions . . . . .	31
2.10	Ferromagnetic domain structure . . . . .	33
2.11	Neel and Bloch domain walls . . . . .	34
2.12	Our approach for the study of LRTC . . . . .	36
3.1	Overall fabrication process . . . . .	38
3.2	Sputtering chamber . . . . .	40

3.3	Sputtering holder and mask . . . . .	40
3.4	Sputtering gun . . . . .	41
3.5	A special alloy target . . . . .	42
3.6	Photolithography . . . . .	43
3.7	Baffled-box . . . . .	45
3.8	Nb top leads . . . . .	46
3.9	Back-sputtering . . . . .	47
3.10	Issue of dust particles. . . . .	48
3.11	Magnetic Force Microscopy (MFM) on Ni film . . . . .	51
3.12	SQUID magnetometry . . . . .	53
3.13	Current comparator circuit . . . . .	55
3.14	Lead configuration . . . . .	56
3.15	Temperature variation measurement set-up . . . . .	57
4.1	Fraunhofer for CuNi Josephson junction . . . . .	60
4.2	Magnetizing CuNi Josephson junction . . . . .	62
4.3	Curie temperature of PdNi . . . . .	65
4.4	M vs H for 100 nm PdNi film . . . . .	66
4.5	$I$ - $V$ characteristics of PdNi . . . . .	68
4.6	$I_c$ vs $H$ for PdNi Josephson junctions . . . . .	69
4.7	Magnetizing PdNi Josephson junctions . . . . .	70
4.8	Magnetic field shift ( $H_{shift}$ ) vs. PdNi thickness ( $d_{PdNi}$ ) . . . . .	71
4.9	Critical current density ( $J_c$ ) vs PdNi thickness ( $d_{PdNi}$ ) . . . . .	72

4.10	Linear Plot: $J_c$ vs. $d_{PdNi}$ for 32.5 to 58 nm . . . . .	73
4.11	Linear Plot: $J_c$ vs. $d_{PdNi}$ for 55 to 85 nm . . . . .	74
4.12	$AR_N$ vs. $d_{PdNi}$ . . . . .	75
4.13	Temperature dependence of critical current for PdNi Josephson junction	82
4.14	Anomalous temperature dependence of critical current for a PdNi Josephson junction using 47.5 nm thick PdNi . . . . .	83
5.1	Giant Magnetoresistance . . . . .	88
5.2	Schematic for a Py/Cu/PdNi spin valve . . . . .	94
5.3	$AR$ vs. $H$ for a Py/Cu/PdNi spin valve . . . . .	96
5.4	$A\Delta R$ vs. $d_{PdNi}$ for a Py/Cu/PdNi spin valve . . . . .	97
5.5	Schematic for a Py/Cu/PdNi/Py/FeMn spin valve . . . . .	99
5.6	$A\Delta R$ vs. $d_{PdNi}$ for a Py/Cu/PdNi/Py/FeMn spin valve . . . . .	100
5.7	Spin-orbit coupling . . . . .	102
5.8	Curie temperature of PdFe alloy . . . . .	105
5.9	$M$ vs $H$ for 80 nm thick PdFe film . . . . .	105
5.10	Schematic for FeMn/Py/Cu/PdFe/Cu/Py/FeMn spin valve . . . . .	107
5.11	$A\Delta R$ vs. $d_{PdFe}$ for the double exchange biased spin valve . . . . .	107
6.1	Fraunhofer for SFS junction using Nickel . . . . .	111
6.2	Oscillatory Exchange Coupling . . . . .	115
6.3	Schematic for Josephson junction using SAF configuration . . . . .	117
6.4	$I_c R_N$ vs. $D_{Co}$ for Josephson junction using SAF configuration . . . . .	118
6.5	SEMPA picture for Co/Cu/Co . . . . .	119
6.6	Fraunhofer for Josephson junction using Co/Cu/Co . . . . .	120

6.7	Generation and Propagation of Triplet correlations . . . . .	122
6.8	Schematic of Triplet sample . . . . .	123
6.9	Fraunhofers for Triplet samples . . . . .	125
6.10	$I_c R_N$ vs $D_{Co}$ for Triplet samples . . . . .	126
6.11	Effect of PdNi thickness variation in Triplet samples . . . . .	128
6.12	$I_c$ vs $H$ (Fraunhofers) measured at different temperatures . . . . .	130
6.13	Temperature Dependence of critical current in Triplet samples . . . . .	131
A.1	Single layer Photolithography . . . . .	141
A.2	Bilayer Photolithography . . . . .	143
A.3	Trilayer Photolithography . . . . .	144
A.4	Image Reversal Process . . . . .	145

# Chapter 1

## Introduction

According to the Bardeen, Cooper and Schrieffer (BCS) theory [1], superconductivity in conventional metals and their alloys is due to s-wave spin-singlet pair correlations. For several decades this type of superconductivity was the only one observed experimentally. In the last two decades several other types of superconductivity have been discovered. In particular, the high-Tc superconductivity discovered by Bednorz and Muller [2] in cuprates is still an extensively studied area, where the pairing is now believed to be an s-wave or a mixture of s-wave and d-wave. Both the s-wave and d-wave ordering usually imply spin-singlet pair correlations. Recently a p-wave spin-triplet pair correlations have been found in strontium ruthenate  $\text{Sr}_2\text{RuO}_4$  [3] and in heavy fermion intermetallic compounds. Because of the p-wave symmetry, these materials are highly sensitive to the presence of impurities. But what strikes our interest here are a new form of spin-triplet correlations, which are symmetric in momentum (s-wave) and hence insensitive to impurities. The novelty of these new type of superconducting correlations lies in the fact that they satisfy the spin-statistics theorem of quantum mechanics by being *odd* under time-reversal (or odd in frequency) and hence they are also known as “*odd-triplet correlations*”. This type of pairing correlations were first proposed by Berezinskii [4] in 1975 as a possible explanation for

superfluidity in  $\text{He}^3$ . However, later years saw that the superfluidity in  $\text{He}^3$  was in fact a result of p-wave spin triplet correlations, which are *even* under time-reversal. The odd-triplet correlations therefore remained a theoretical possibility that had no counterpart in the real world. But a series of experiments performed in the late 1990's [5, 6, 7] renewed the possibility of observing odd-triplet superconductivity in real systems. These were experiments conducted by different groups studying the proximity effect in superconductor/ferromagnet (S/F) structures.

## 1.1 Proximity Induced Odd Triplet Superconductivity

The word *proximity effect* defines an interplay between a superconductor and any other metal brought in close contact with each other. When a BCS superconductor is placed next to a normal metal, the superconducting correlations are known to penetrate the normal metal over a distance as large as few microns at low temperatures. If instead of a normal metal, a ferromagnet is placed next to a conventional superconductor, the spin-singlet correlations are known to oscillate and decay rapidly inside the ferromagnet on a length scale of just few nanometers. This short length-scale of decay was known to be a general characteristic of the S/F proximity effect until some unusually long range effects were observed by a few groups in the late 1990's [5, 6, 7]. In 2001, two theoretical groups [8, 9] published papers indicating proximity-induced odd-triplet correlations in S/F systems, provided that the F-layer has magnetic inhomogeneities. It is now believed that the long-range proximity effect observed in S/F systems is a result of proximity-induced odd triplet correlations. Another promising hint of these spin-triplet correlations was reported recently in a half-metallic ferromagnet  $\text{CrO}_2$  by Keizer *et al.* Since  $\text{CrO}_2$  [10] is a fully spin-polarized magnet (where the electron transport is metallic for spin-up electrons, while it is insulating for spin-

down electrons), the observation of long-range proximity effect was considered an unequivocal indication of triplet correlations. However, there was no confirmation of these results for a long time. The difficulties in reproducing the result lie in the complex nature of CrO<sub>2</sub> that is sensitive to its growth conditions. Bergeret *et al.* [8, 11] recently proposed several mechanisms that lead to inhomogeneous magnetism in S/F systems, such as: magnetic disorder, non-collinear magnetic domains, spin active interfaces, etc. Since then several other theory papers suggesting different ways to study proximity-induced odd-triplet superconductivity have emerged in this area.

## 1.2 This Work

The presence of proximity-induced odd-triplet correlations can be tested either by measuring the density of states or by measuring the Josephson effect. Each method has its own pros and cons, however in our search for this new symmetry prediction, we have chosen to work with Superconductor/Ferromagnet/Superconductor (S/F/S) Josephson junctions. Our experiments were aimed at studying the conditions and materials suitable for the observation of odd-triplet correlations. In this thesis I will explain the various considerations that went into creating the final S/F/S Josephson junction which showed strong evidence of odd-triplet correlations.

The brief outline of this thesis is as follows– *Chapter 2* focuses on the physics behind the S/F proximity effect. It also discusses in detail the conditions necessary for the generation and observation of long-range odd-triplet correlations. *Chapter 3* gives the details of the fabrication procedure and the measurement techniques used in our experiments. *Chapter 4* shows the results of our first Josephson junction experiment using a weakly ferromagnetic alloy- PdNi. The absence of odd-triplet correlations in this experiment led us to investigate the spin memory length in this alloy using standard Giant Magnetoresistance techniques, which are described in *Chapter 5*. *Chapter*

6 talks about our much awaited results—the observation of spin-triplet superconductivity in our Co-based Josephson junctions using PdNi alloy near the Nb interface. The final device modeled and reported in this chapter is a result of a series of conclusions drawn from different experiments performed in Prof. Birge’s group, I will therefore also give a brief overview of those experiments in this chapter. Finally in *Chapter 7*, I will discuss the possible mechanism behind the generation of odd-triplet correlations in our experiment. I will also talk about the interesting experiments that are currently in progress in the group. We believe these experiments will help us improve our understanding of the microscopic mechanism behind the generation of odd-triplet correlations.

# Chapter 2

## Theoretical Background

### 2.1 Superconductivity

Superconductivity is manifested as a sudden drop in resistivity below a certain critical temperature ( $T_c$ ). It was discovered in 1911 by Heike Kamerlingh Onnes in mercury at liquid helium temperatures [12]. Later many materials were found to show a similar transition at various temperatures. The superconducting material we use in our work is Niobium; it undergoes a superconducting transition at a temperature of about 9.25 K.

Among the most striking properties of the superconductors are: 1) Ideal diamagnetism that leads to magnetic flux expulsion from the superconductor (Meissner effect); 2) Macroscopic quantum nature of superconductivity including phase coherence that leads to zero resistivity and the Josephson effect; 3) Quantization of magnetic flux passing through a superconducting loop, a practical application of which is SQUID (Superconducting QUantum Interference Device).

A microscopic explanation for superconductivity was not fully known until John Bardeen, Leon Cooper and Robert Schrieffer [1] put forth their epoch-making theory of superconductivity called *BCS theory* in 1957. In this theory it was shown that

a phonon-mediated weak attractive interaction between electrons can lead to the formation of bound pair of electrons with opposite momenta and spin. Such pairs of electrons act as superconducting charge carriers in the material and are known as *Cooper pairs*. The BCS ground state wave function consisting of the bound state electrons (Cooper pairs) is given in terms of the electron creation operator  $c^\dagger$  as follows,

$$|\Psi_G\rangle = \prod_{k=k_1, k_2, \dots, k_M} (u_k + v_k c_{k\uparrow}^\dagger c_{k\downarrow}^\dagger) |\phi_0\rangle \quad (2.1)$$

with  $|u_k|^2 + |v_k|^2 = 1$ . Here  $|v_k|^2$  is the probability that the pair state  $(k \uparrow, -k \downarrow)$  is occupied,  $|u_k|^2$  is the probability that it is unoccupied and  $|\phi_0\rangle$  is the vacuum state. Using this ground state, the single particle excitation spectrum is given by,

$$E_k^2 = \epsilon_k^2 + |\Delta_k|^2 \quad (2.2)$$

where,  $\Delta_k$  is the minimum excitation energy or the superconducting energy gap and  $\epsilon_k$  is the kinetic energy measured from the Fermi energy. An excitation in a superconductor is described in terms of a quasiparticle (electron-like or hole-like) excitation above the gap in the superconductor. The gap,  $\Delta_k$  is determined by the self-consistency equation,

$$\Delta_k = - \sum_{k'} \frac{V_{k,k'} \Delta_{k'}}{2E_{k'}} \quad (2.3)$$

where,  $V$  is the weak negative constant interaction that leads to pairing of electrons.

### 2.1.1 London Penetration Depth

When a superconductor is placed in a uniform magnetic field of flux density  $B_a$  applied parallel to its surface, the flux density at distance  $x$  inside the superconductor is given

by,

$$B(x) = B_a \exp\left(\frac{-x}{\lambda_L}\right) \quad (2.4)$$

where,  $B_a$  is the flux density at the surface of the superconductor. The equation shows that the flux density decays exponentially inside a superconductor falling  $1/e$  of its value at the surface at a distance  $\lambda_L$ . This distance is called the *London penetration depth* and is given by,

$$\lambda_L = \sqrt{\frac{m}{\mu_0 n_S e^2}} \quad (2.5)$$

where,  $n_S$  is the density of Cooper pairs,  $m$  is the mass, and  $e$  is the charge.

## 2.2 Proximity effect

### 2.2.1 Superconductor/Normal metal (S/N)

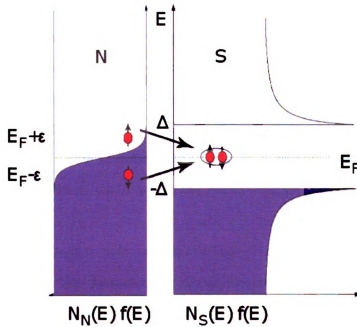


Figure 2.1: *Andreev reflection. A process by which electrons penetrates from N to S at energies less than the superconducting gap,  $\Delta$ .*

When a superconductor (S) is placed in good electrical contact with a non-superconducting, non-magnetic (N) metal, the properties of both the metals are modified. The appearance of superconducting correlations in the N metal near N/S interface is called the *proximity effect*. The weakening of superconductivity in the S-metal near the interface is sometimes referred to as the *inverse proximity effect*. The microscopic mechanism responsible for the proximity effect is *Andreev reflection*. The schematic of this process is shown in Fig. 2.1. When an electron near the Fermi energy approaches the S/N interface from the N-side, it cannot find a single-particle state with the same energy on the S-side due to the energy gap  $\Delta$ . If the initial electron with energy  $\epsilon$  (measured with respect to the Fermi energy) can find a time-reversed partner with energy  $-\epsilon$ , then the two electrons can enter the superconductor as a Cooper pair. The disappearance of the partner can be viewed as creation of a hole on the N-side, which follows the time-reversed trajectory of the incident electron in the limit  $\epsilon \rightarrow 0$ .

In a simple language, Andreev reflection can be viewed as penetration of two electrons from N-side to S-side to form a Cooper pair, whereas inverse Andreev reflection can be viewed as “leakage” of a Cooper pair from S-side to N-side. The two electrons of the Cooper pair enter N-side with nearly opposite momenta as seen in Fig. 2.2a. The wavefunctions of the two electrons in N-side remain in phase with each other for times of order  $\hbar/\epsilon$ . This translates into the length  $\hbar v_F/\epsilon$  in the clean limit or  $\sqrt{\hbar D_F/\epsilon}$  in the dirty limit, where  $v_F$  is the Fermi velocity and  $D$  is the diffusion constant.

Andreev reflection leads to pair correlations in the N-metal near the S/N interface. At finite temperature, the characteristic decay length of these correlations in the normal metal is called the *normal metal coherence length*  $\xi_N$ . In the clean limit it is given by [13],

$$\xi_N = \frac{\hbar v_F}{2\pi k_B T} \quad (2.6)$$

In the dirty limit it is given by,

$$\xi_N = \sqrt{\frac{\hbar D}{2\pi k_B T}} \quad (2.7)$$

The *clean limit* here is defined as a regime when  $l_N > \xi_N$  and the *dirty limit* is a regime when  $l_N < \xi_N$ , where  $l_N$  is the electron mean free path in the N-metal. The spatial extent of the correlations depends on whether the system is clean or diffusive. At low enough temperatures it can be  $\sim$  few microns.

### 2.2.2 Superconductor/Ferromagnet (S/F)

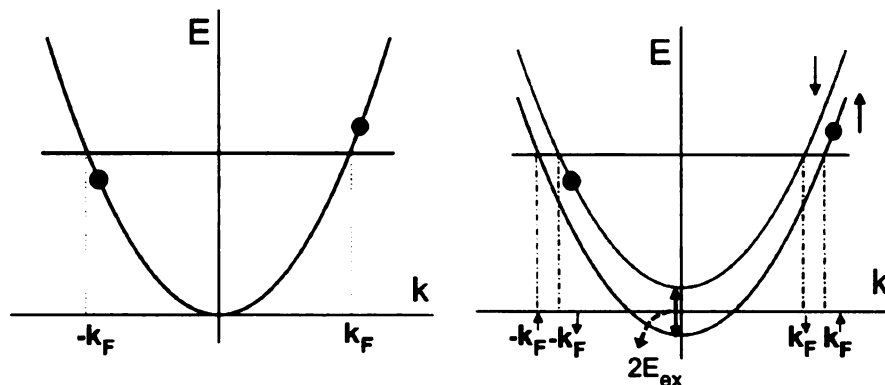


Figure 2.2: (a) 1D free-electron dispersion relation in a normal metal, showing two electrons that have "leaked" into N from S (In the Andreev reflection picture, the electron below the Fermi surface would be shown as a hole). (b) Same situation in a ferromagnet. In this case there is a shift between the Fermi wavevectors of the two electrons due to the exchange energy of the ferromagnet.

The main difference between the proximity effect in N/S and F/S systems can be illustrated using the simplistic model of a ferromagnet shown in Fig. 2.2. On a microscopic level, a Cooper pair is transferred from S to F in the absence of significant spin-orbit coupling. When a Cooper pair leaks from S to F, the two electrons must enter opposite spin bands. Due to the exchange energy  $E_{ex}$ , the Fermi wavevector

of the spin-down band is different from the spin-up band. In a Cooper pair, the electron with spin parallel to the exchange field is decreased in potential energy, and the electron with spin anti-parallel to the exchange field is increased in energy by the same amount. The conservation of total energy requires,

$$\left| \frac{\hbar^2 k'^2}{2m} - \frac{\hbar^2 k^2}{2m} \right| = 2E_{ex} \quad (2.8)$$

As a result the total momentum of the Cooper pair is not zero but is given as  $Q = k_F^\uparrow - k_F^\downarrow \approx 2E_{ex}/v_F$ . The order parameter acquires a term proportional to  $\exp(iQx/\hbar)$ . Fermionic antisymmetry requires consideration of the above pair as well as the pair which has the down-spin and up-spin electrons interchanged in momentum space, the latter gaining a center of mass momentum  $-Q$ . Now, if one considers the effect of Cooper pairs incident on the interface at an arbitrary angle  $\theta$ , then the net gain of momentum of these pairs will be  $2Q/\cos\theta$ . In 1D clean limit this leads to the oscillation of the superconducting correlations. In 3D clean limit, averaging over all possible angles leads to an oscillation as well as an algebraic decay of the superconducting correlations, given by  $\sin(x/\xi_F)/(x/\xi_F)$ , where  $\xi_F = \hbar v_F/2E_{ex}$ . In dirty limit in the presence of strong disorder scattering, the superconducting pair correlations oscillate and decay exponentially as  $\sin(x/\xi_F^*)\exp(-x/\xi_F^*)$ , where  $\xi_F^* = \sqrt{\hbar D/E_{ex}}$  [14]. Thus the S/F proximity effect is characterized by a decaying, but oscillating, order parameter. The characteristic decay length of these correlations in the ferromagnet is called the *superconducting coherence length in ferromagnet* and is given by  $\xi_F$  in the clean limit and  $\xi_F^*$  in the dirty limit. For strong ferromagnets such as Fe, Co or Ni, the large exchange energy causes the coherence length  $\xi_F^*$  to be around 1 nm in the dirty limit, whereas in weak ferromagnets the coherence length can be relatively longer  $\sim$  few nm. Thus the proximity effect in S/F systems can be considered to be an extremely short ranged effect in comparison to the proximity

effect in S/N systems.

## 2.3 Short Range Correlations

Although the penetration depth of the superconducting pair correlations in F-metals is small, the physics of the proximity effect in S/F structures is not exhausted by this suppression. In fact, the oscillatory nature of this short ranged proximity effect has been reported to give rise to very interesting effects in S/F experiments. For example, these oscillations are known to result in,

- Oscillation of critical superconducting temperature ( $T_c$ ) as a function of F-layer thickness ( $d_F$ ) in S/F structures [15, 16, 17, 18, 19, 20].
- Oscillation of Josephson critical current as a function of F-layer thickness [21, 22, 23, 24, 25, 26, 27, 28, 29, 30].
- Oscillation in the sign of the proximity effect corrections to the density of states (DOS) [31].

However interesting may be the effects seen in the above experiments, the short ranged nature of the S/F proximity effect in these systems is a well known and an extensively studied area. Studying these effects therefore was not the prime goal of our project. Our interest in S/F systems on the other hand stems from an exotic long-range proximity effect that is predicted to occur in such systems under certain conditions. The next section will describe more about this effect.

## 2.4 Long Range Triplet Correlations (LRTC)

### 2.4.1 What are LRTCs?

A new exotic type of proximity induced superconductivity is predicted to occur in S/F systems in the presence of magnetic inhomogeneities and is called “*odd-triplet superconductivity*” [9, 8]. This type of superconductivity, causes a long-range proximity effect which is not governed by the strength of the exchange field but is only limited by the temperature and could be as long as that in the case of S/N systems.

The long-range proximity effect occurs in S/F systems only under certain conditions. In the case of homogeneous magnetization in F-layer only a singlet component ( $s = 0, m = 0$ ) and a short range triplet ( $s = 1, m = 0$ ) component of the pair correlations arises in the structure. These components decay very fast in the F-layer because the strong magnetization makes the spins of a pair to be parallel to each other, thus destroying the superconducting correlations over the length,  $\xi_F^{Singlet} = \sqrt{\hbar D/E_{ex}}$  in dirty limit. However in the case of inhomogeneous magnetization in F-layer, alongside with the singlet component, all types of triplet Cooper pairs arise ( $s = 1; m = 0, \pm 1$ ). The components with  $s = 0, m = \pm 1$  can penetrate longer distances in a ferromagnet since both electrons in the Cooper pair can enter the same spin band in the ferromagnet. In addition, the superconducting correlations with non-zero orbital momentum are generally sensitive to disorder, whereas the s-wave ( $l = 0$ ) nature of such triplet correlations should be robust even in the presence of disorder (according to Anderson’s theorem). This component ( $s = 1, m = \pm 1$  and  $l = 0$ ) therefore penetrates much longer distance in ferromagnet, over the length,  $\xi_F^{Triplet} = \sqrt{\hbar D/2\pi kT}$  in dirty limit and is referred to as *Long-Range Triplet Component (or correlations), LRTC*.

According to the spin-statistics theorem of quantum mechanics, two spin half particles, i.e. fermions, should have a wavefunction that is antisymmetric under the exchange of particles. Conventional BCS superconductivity is attributed to spin

singlet correlations (antisymmetric spin part) which obey this fermionic antisymmetry by being *even* in orbital angular momentum state ( $l = 0$ ). Similarly there exists a ‘p-type’ superconductivity that is attributed to triplet correlations (symmetric spin part) and which obeys the fermionic antisymmetry by being *odd* in orbital angular momentum state ( $l = 1$ ). This is seen in materials like  $\text{Sr}_2\text{RuO}_4$  and  $\text{UPt}_3$ . The odd nature of triplet superconductivity we are studying here, lies in pair correlations that have an even orbital angular momentum ( $l = 0$ ) while still being spin triplets ( $s = 1, m = \pm 1$ ). This may seem like a violation of the Pauli exclusion principle which demands an overall antisymmetry of the wavefunction. However it turns out that the Pauli exclusion principle is not violated, because the overall antisymmetry of the wavefunction in this case is maintained by pair correlations that are odd under time reversal and hence the name “*odd-triplet superconductivity*”. The blank boxes in Table 2.1 indicate the “rare” cases that are allowed only if the pair correlations are odd under time reversal.

	s=0 (antisymmetric)	s=1 (symmetric)
l=0	BCS superconductors	–
l=1	–	$\text{SrRuO}_4$
l=2	High-Tc superconductors	–

Table 2.1: *Combinations of 2-particle fermionic correlation functions allowed by the exchange symmetry. The blank combinations are not allowed normally, but they become available if pair correlations are odd under time (or frequency)*

## 2.4.2 A Simplified Picture of Triplet Generation Mechanism

The following section gives a simplified picture of the triplet generation mechanism. This however is not a rigorous derivation, but is a mere attempt in explaining the importance of non-collinear magnetization or magnetic inhomogeneities in the generation of long-range triplet correlations.

As discussed earlier, when a Cooper pair enter a ferromagnetic region, it acquires

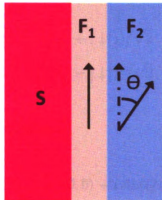


Figure 2.3: A ferromagnet( $F_1$ ) placed next to superconductor generates spin-singlet( $s = 0, m = 0$ ) as well as short range spin-triplet ( $s = 1, m = 0$ ) correlations in the system. In presence of magnetic inhomogeneities (shown by a second ferromagnet  $F_2$  with a rotated magnetic moment), rotation of short range spin-triplet component into long-range triplet-components ( $s = 1, m = \pm 1$ ).

a center of mass momentum  $Q$ . The fermionic antisymmetry requires us to consider this pair along with a pair which has down spin and up spin electrons interchanged in the momentum space [14] with a center of mass momentum  $-Q$ . One can therefore write down the following wavefunction,

$$|\chi_m\rangle = \frac{1}{\sqrt{2}} [exp(iQx) | \uparrow \downarrow \rangle - exp(-iQx) | \downarrow \uparrow \rangle] \quad (2.9)$$

$$|\chi_m\rangle = \cos(Qx) \frac{(| \uparrow \downarrow \rangle - | \downarrow \uparrow \rangle)}{\sqrt{2}} + i \sin(Qx) \frac{(| \uparrow \downarrow \rangle + | \downarrow \uparrow \rangle)}{\sqrt{2}} \quad (2.10)$$

$|\chi_m\rangle$  is not the full wavefunction. It only shows the spin part and the center of mass part. If  $x_1$  and  $x_2$  are the co-ordinates of two electrons, then  $x = (x_1 + x_2)/2$ .

For two spin-1/2 particles one can also use eigenstates of total spin and its  $z$ -

component,

$$|1, 0\rangle = (|\uparrow\downarrow\rangle + |\downarrow\uparrow\rangle)/\sqrt{2} \quad (2.11)$$

$$|0, 0\rangle = (|\uparrow\downarrow\rangle - |\downarrow\uparrow\rangle)/\sqrt{2} \quad (2.12)$$

One can rewrite the Eqn. 2.9 as follows,

$$|\chi_m\rangle = \cos(Qx)|0, 0\rangle + i \sin(Qx)|1, 0\rangle \quad (2.13)$$

The above shows that in case of homogeneous magnetization in the F-layer, not only spin-singlet correlations ( $s = 0, m = 0$ ) but also short-range triplet correlations ( $s = 1, m = 0$ ) are generated by the virtue of exchange field. This can be explained by the schematic shown in Fig. 2.3. The  $F_1$  layer in the figure represents the ferromagnet with homogeneous magnetization, whereas the  $F_2$  layer represents the ferromagnet with inhomogeneous magnetization. The presence of homogeneous ferromagnet  $F_1$  induces spin-singlet as well as short-range triplet correlations. However, it is this  $s = 1, m = 0$  triplet component that in the presence of non-uniform magnetization gives rise to long-range triplet components ( $s = 1, m = \pm 1$ ). This inhomogeneity is provided by a different orientation of magnetization, present either in the same ferromagnet or provided artificially by placing a separate ferromagnet with different direction of magnetization (as shown by layer  $F_2$  in Fig. 2.3). To understand the role of short range triplet component and the magnetic inhomogeneities better, let us consider the rotation matrix for total angular momentum  $j = 1$  case,

$$R(\beta) = \exp\left(\frac{-iJ_y\beta}{\hbar}\right) = \begin{bmatrix} \frac{1}{2}(1 + \cos \beta) & -\frac{1}{\sqrt{2}} \sin \beta & \frac{1}{2}(1 - \cos \beta) \\ \frac{1}{\sqrt{2}} \sin \beta & \cos \beta & -\frac{1}{\sqrt{2}} \sin \beta \\ \frac{1}{2}(1 - \cos \beta) & \frac{1}{\sqrt{2}} \sin \beta & \frac{1}{2}(1 + \cos \beta) \end{bmatrix} \quad (2.14)$$

The components  $s = 1, m = 0, \pm 1$  can be written down in the matrix form as follows,

$$|1, 1\rangle = |\uparrow\uparrow\rangle = \begin{bmatrix} 1 \\ 0 \\ 0 \end{bmatrix} \quad (2.15)$$

$$|1, 0\rangle = (|\uparrow\downarrow\rangle + |\downarrow\uparrow\rangle)/\sqrt{2} = \begin{bmatrix} 0 \\ 1 \\ 0 \end{bmatrix} \quad (2.16)$$

$$|1, -1\rangle = |\downarrow\downarrow\rangle = \begin{bmatrix} 0 \\ 0 \\ 1 \end{bmatrix} \quad (2.17)$$

Consider rotation of the state  $|1, 0\rangle$  gives,

$$R(\beta) \begin{bmatrix} 0 \\ 1 \\ 0 \end{bmatrix} = \begin{bmatrix} \frac{1}{2}(1 + \cos \beta) & -\frac{1}{\sqrt{2}} \sin \beta & \frac{1}{2}(1 - \cos \beta) \\ \frac{1}{\sqrt{2}} \sin \beta & \cos \beta & -\frac{1}{\sqrt{2}} \sin \beta \\ \frac{1}{2}(1 - \cos \beta) & \frac{1}{\sqrt{2}} \sin \beta & \frac{1}{2}(1 + \cos \beta) \end{bmatrix} \begin{bmatrix} 0 \\ 1 \\ 0 \end{bmatrix} \quad (2.18)$$

$$R(\beta) \begin{bmatrix} 0 \\ 1 \\ 0 \end{bmatrix} = \begin{bmatrix} -\frac{1}{\sqrt{2}} \sin \beta \\ \cos \beta \\ \frac{1}{\sqrt{2}} \sin \beta \end{bmatrix} \quad (2.19)$$

Setting  $\beta = \pi/2$  gives,

$$R(\beta) \begin{bmatrix} 0 \\ 1 \\ 0 \end{bmatrix} = \begin{bmatrix} -1/\sqrt{2} \\ 0 \\ 1/\sqrt{2} \end{bmatrix} = -\frac{1}{\sqrt{2}} \begin{bmatrix} 1 \\ 0 \\ 0 \end{bmatrix} + \frac{1}{\sqrt{2}} \begin{bmatrix} 0 \\ 0 \\ 1 \end{bmatrix} \quad (2.20)$$

From above, one can see that under rotation the triplet components ( $s = 1, m = 0, \pm 1$ ) transform amongst themselves just like the three components of a vector. The presence magnetic inhomogeneities in S/F systems serves as a mechanism that causes the rotation of short range triplet component ( $s = 1, m = 0$ ) into long-range triplet components ( $s = 1, m = \pm 1$ ).

It is instructive to notice that the Eqn. 2.10 has a symmetric and an antisymmetric spin part, according to Pauli exclusion principle the overall antisymmetry of the total wavefunction is satisfied by a conjugate antisymmetric and symmetric spacial part respectively. However, this is not necessarily true since the Pauli exclusion principle can also be satisfied by demanding that both the spacial and spin part have an identical symmetry (either both even or both odd) under the interchange of particles, and that the fermionic antisymmetry is respected by being odd under time reversal (or odd in frequency). A detailed theoretical analysis is beyond the scope of the simplified picture explained above and needs to be worked upon in the future.

### **2.4.3 Previous Experimental Hints of LRTC**

This phenomenon of LRTC as described above cannot be expected from the simple picture of a superconductor in contact with a ferromagnet. As we said before, LRTCs are predicted to occur only when the exchange field is not homogeneous. However in 1990's, much before this prediction, three groups observed an unexpected decrease of the resistance of a micron sized ferromagnetic wire attached to a superconductor, when the temperature was lowered below the superconducting transition temperature  $T_c$  [7, 5, 6]. Given the short-range nature of spin-singlet correlations, this long-range proximity effect was initially a surprise and was attributed to anomalous interface effects. However, in later studies theorists [8, 9] pointed out that the long-range effect in these experiments was a natural outcome of proximity-induced odd spin-triplet correlations rather than spin-singlet correlations. In addition to these experiments,

similar long-range effect were observed by Klapwijk's group [10] working on S/F/S Josephson junctions using NbTiN as the S-layer and CrO<sub>2</sub> as the F-layer. Since CrO<sub>2</sub> is a half-metallic ferromagnet (fully spin-polarized ferromagnet), it was considered as an unequivocal experiment ruling out all the other explanations. However, large sample-to-sample variations seen in this experiment made it difficult to analyze their result. Another experiment reporting phase-dependent conductance oscillations of a Holmium (Ho) wire attached to superconducting electrodes on its both side were attributed to the presence of triplet correlations [32]. It was believed that the spiral magnetization in Ho is responsible for triplet correlations.

After the above mentioned experiments, there was a huge surge in the number of theory papers suggesting possible ways to generate LRTC. In spite of such large number of possibilities suggested by these papers, it is not only difficult to find new systems that generate LRTC, but it is also equally difficult to reproduce the results of the handful of experiments that are mentioned above.

#### 2.4.4 Ways to induce LRTC in S/F Systems

If magnetic inhomogeneities exist one should be able to see long-range effects in the S/F structures. These magnetic inhomogeneities needed for the generation of LRTC can be provided by any of the following mechanisms,

1. **Intrinsic Inhomogeneity:** Intrinsic magnetic inhomogeneities provided by the domains and/or the domain walls at the S/F interface [8, 33, 34] or the spiral magnetic order in certain ferromagnets (For e.g. Holmium), are predicted to result in LRTC. [35, 36, 37, 38]
2. **Extrinsic Inhomogeneity:** Magnetic inhomogeneities can be induced experimentally by manipulating the multilayers such that different F-layers have different directions of magnetization. For example, it has been suggested to use

F/S/F trilayer structures such that magnetization in two F-layers are inclined at an angle  $\pm\alpha$  with respect to the z-axis. If the distance between the two F-layers is less than the superconducting coherence length,  $\xi_s$ , then the triplet correlations can get induced in the central layer. [39]

3. **Spin Active Interfaces:** Inhomogeneous magnetization can also be obtained through a spin active interface that allows for spin-flip processes. [40, 41, 42, 43, 44, 45]

### 2.4.5 Ways to detect LRTC

A reliable experimental signature of induced triplet superconductivity can be obtained by doing one of the following experiments,

1. By measuring the proximity-induced changes in density of states (DOS). However since such changes in DOS are extremely small [31], we have chosen not to use this method for the detection of LRTC.
2. By measuring the Josephson effect in S/F/S junctions. For all the experiments described in this thesis, we have chosen to work with Josephson junctions.[10]

## 2.5 Theoretical Predictions for LRTC

A large amount of theoretical work devoted to the study of odd-triplet correlations uses equations based on the quasi-classical Green's function formalism that was first recognized by Eilenberger [46]. In the dirty limit, these equations are simplified further by Usadel [47] and are therefore known as Usadel equations. There are some excellent review articles that discuss various types of S/F structures suitable for the generation of LRTC [48, 11].

In some papers, special attention is paid to the nature of the S/F interface. In particular a large number of theory papers are devoted to the study of LRTC generated by the spin-active interfaces [40, 41, 42]. The approach used in these papers describes the spin-active interface by a scattering matrix, the elements of which are considered as phenomenological parameters, i.e., in this approach one does not need to know a lot about the detailed structure of the interface, but one can proceed with the calculations based on these phenomenological parameters. Materials with large spin-orbit scattering can be treated as forming a spin-active interface. Also, there is another point of view which considers an interface with domain walls smaller than the Fermi wavelength as a spin-active interface. This allows to invoke the quasi-classical approximation and simplifies solving the problem. This point of view was taken by various theorist in Ref. [33, 49].

Similarly, there is a huge amount of literature devoted to the study of LRTC based on the domain structure in the F-layer. In particular, Ref. [8] discusses the generation of LRTCs in diffusive S/F structures with a Bloch-type domain wall. The LRTC in Neel-type domain wall was analyzed in Ref. [33] A general case of domain wall with a width arbitrary with respect to the mean free path and an arbitrary impurity concentration, was studied in Ref. [34].

The interface transparency has been treated differently in several of these papers. For example, Braude and Nazarov have studied LRTC in S/F structures with highly transparent interfaces. This is termed as strong proximity effect. In other papers, LRTC has been studied assuming weak proximity effect. This assumption allows one to linearize the Usadel equations which simplifies the calculations [50, 49].

A lot of stress has been laid on generating the inhomogeneities by creating artificial structures using F/S/F trilayers such that different F layers have different direction of magnetization. In particular the Ref. [39] studies F/S/F/S/F structure with different magnetic orientation of F and F' layers. Similarly structures of the

form of S/F/I/F/S have been analyzed when the magnetic moments in the F-layers are antiparallel and parallel. A larger critical current is predicted for the antiparallel case than the parallel case [11]. In addition, the critical current in antiparallel case was found to be larger than for the case without any ferromagnets, indicating that ferromagnetism can enhance critical current [51]. Also, diffusive Josephson junctions of the form of S/F/F'/S are studied in Ref. [52, 53]. Since it is not possible to have Josephson current due to the interference between the singlet and triplet components, two sources of triplet components are needed in Josephson junctions to observe the long-range Josephson effect. Accordingly the long-range Josephson effect is not possible in Josephson junctions with only two F-layers. This led two groups to suggest the geometries of the Josephson junction of the form S/F'/F/F''/S [54, 49]. We find this geometry most relevant to our triplet experiment discussed later in Chapter 6.

Temperature dependence of the LRTC has also been studied by some papers for the triplet case [40, 41, 50, 49]. The nature of triplet dependence is sensitive to the relative magnitudes of various energies. If  $E_{ex} > E_F$ , anomalous temperature dependence is expected, whereas standard temperature dependence is expected if  $E_{ex} < E_F$ . However, a few experiments performed in this category do not seem to follow these predictions.

## 2.6 Josephson Junctions

### 2.6.1 Definition

A Josephson junction consists of two superconductors separated by a non-superconducting layer which is so thin that electrons can tunnel through the barrier. A number of interesting phenomenon occur in such a junction. The simple analysis given in the following section is taken from *The Feynman's Lectures on Physics-Volume III*.

Consider a macroscopic superconducting wavefunction,  $\psi_1$ , as a common wave

function of all the electrons on one side, and  $\psi_2$  as the corresponding wavefunction on the other side. These superconducting wavefunctions satisfy the Schrodinger equations,

$$i\hbar \left( \frac{\partial \psi_1}{\partial t} \right) = E_1 \psi_1 + K \psi_2 \quad (2.21)$$

$$i\hbar \left( \frac{\partial \psi_2}{\partial t} \right) = E_2 \psi_2 + K \psi_1 \quad (2.22)$$

where,  $E_1$  and  $E_2$  are ground state energies of two superconductors, and  $K$  is a real coefficient that describes the coupling between two superconducting wavefunctions. If a constant potential difference  $V$  is applied between the two superconductors, the ground state energies are shifted such that,

$$E_1 - E_2 = e^* V \quad (2.23)$$

where,  $e^* = 2e$  is the charge carried by a Cooper pair. For the ease of calculations let us redefine the zero of energy mid-way between  $E_1$  and  $E_2$ , then the shift caused by applied voltage is such that  $E_1 = eV$  and  $E_2 = -eV$ . The resulting Eqns. 2.21 and 2.22 can be re-written as,

$$i\hbar \left( \frac{\partial \psi_1}{\partial t} \right) = eV \psi_1 + K \psi_2 \quad (2.24)$$

$$i\hbar \left( \frac{\partial \psi_2}{\partial t} \right) = -eV \psi_2 + K \psi_1 \quad (2.25)$$

Substituting the superconducting wavefunctions of the form,  $\psi_1 = |\psi_1| \exp(i\theta_1)$  and  $\psi_2 = |\psi_2| \exp(i\theta_2)$ , where  $\theta_1$  and  $\theta_2$  are the macroscopic phases in superconductor 1

and 2 respectively; and separating the real and imaginary parts one gets,

$$\hbar \frac{\partial |\psi_1|^2}{\partial t} = 2K |\psi_1| |\psi_2| \sin \varphi \quad (2.26)$$

$$\hbar \frac{\partial |\psi_2|^2}{\partial t} = -2K |\psi_1| |\psi_2| \sin \varphi \quad (2.27)$$

$$\hbar \frac{\partial \theta_1}{\partial t} = -K \left| \frac{\psi_2}{\psi_1} \right| \cos \varphi - eV \quad (2.28)$$

$$\hbar \frac{\partial \theta_2}{\partial t} = -K \left| \frac{\psi_1}{\psi_2} \right| \cos \varphi + eV \quad (2.29)$$

where we have used  $\varphi = \theta_2 - \theta_1$ . The current densities flowing into each superconductor are given by,

$$J_1 = 2e \frac{\partial |\psi_1|^2}{\partial t} \quad (2.30)$$

$$J_2 = 2e \frac{\partial |\psi_2|^2}{\partial t} \quad (2.31)$$

$$J_1 = -J_2 = J_c \quad (2.32)$$

If we substitute the density of Cooper pairs in each superconductor equal to  $\rho_0$ , i.e.  $|\psi_1|^2 = |\psi_2|^2 = \rho_0$  and  $J_c = 2e \frac{2K |\psi_1| |\psi_2|}{\hbar} \approx 2e \frac{2K \rho_0}{\hbar}$ . Equation 2.26 and 2.27 yield the *first Josephson relation*,

$$J_s(\varphi) = J_c \sin \varphi \quad (2.33)$$

Equation 2.28 and 2.29 yield the *second Josephson relation*,

$$\frac{\partial \varphi}{\partial t} = 2e \frac{V}{\hbar} \quad (2.34)$$

## 2.6.2 Resistively Shunted Junction (RCSJ)

The first Josephson relation gives the current-phase relation for a Josephson junction,

$$I_s = I_c \sin \varphi \quad (2.35)$$

where  $I_c$  is the maximum supercurrent that a junction can withstand. According to this equation, the applied current controls the phase-difference between the two superconductors. For  $I < I_c$ , the phase-difference stays constant, but for  $I > I_c$ , a voltage  $V$  appears across the junction as the phase evolves according to the second Josephson relation,

$$\dot{\varphi} = \frac{2eV}{\hbar} = \frac{2\pi V}{\Phi_0} \quad (2.36)$$

A typical I-V characteristics of a Josephson junction is shown in Fig. 2.6b. Even

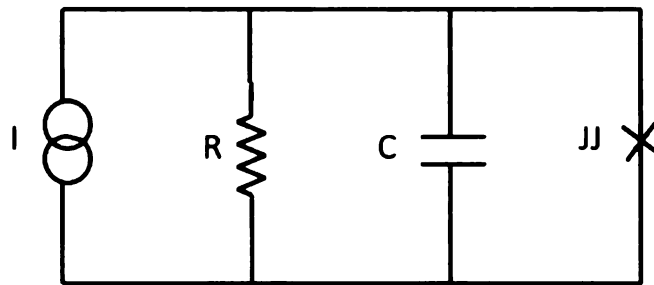


Figure 2.4: The equivalent circuit of RCSJ model. The cross in the figure represents Josephson junction (JJ).

a high quality tunnel junction sometimes shows a hysteretic I-V characteristics. For most of the practical applications of a Josephson junction it is important to eliminate the hysteresis, which is done by shunting the junction with an external shunt resistor. The resulting circuit is called *Resistively Shunted Junction (RSJ)* model. The equivalent circuit of RCSJ model is shown in Fig. 2.4. The self-capacitance of the junction is indicated by the capacitance  $C$ . If one assumes a current noise  $I_N(t)$  associated with the resistor, the resulting equation of motion is given by,

$$C\dot{V} + \frac{V}{R} + I_c \sin \varphi = I + I_N(t) \quad (2.37)$$

Setting  $V = \hbar\dot{\phi}/2e$ , and ignoring the noise yields,

$$\frac{C\hbar}{2e}\ddot{\phi} + \frac{\hbar}{2eR}\dot{\phi} = I - I_c \sin \varphi = -\frac{2e}{\hbar} \frac{\partial U_J}{\partial \varphi} \quad (2.38)$$

where,

$$U_J = \frac{\Phi_o}{2\pi} [I_c(1 - \cos \varphi) - I\varphi] \quad (2.39)$$

$$U_J = E_J(1 - \cos \varphi - i\varphi) \quad (2.40)$$

where  $\Phi_o = h/2e$  is the magnetic flux quantum,  $E_J = I_c\Phi_o/2\pi$  is the Josephson energy, and  $i = I/I_c$ . The dynamics of the Josephson junction given by the above equations is analogous to the motion of a ball of mass  $m$  and friction  $\eta$  moving on a tilted washboard potential.  $F_d$  is the external driving force that tilts the potential  $w(x)$  [55].

$$m\ddot{x} + \eta\dot{x} = -\frac{\partial w(x)}{\partial x} + F_d = -\frac{\partial[w(x) - F_dx]}{\partial x} \quad (2.41)$$

Comparing Eqn. 2.38 and Eqn. 2.41, one can say that the Eqn. 2.38 represents the equation of motion of a ball of mass  $C\hbar/2e$  moving along  $\varphi$  axis and subjected to a viscous drag force given by  $(\hbar/2e)^2(1/R)d\varphi/dt$ . The effective potential experienced by the ball is given by  $U_J$ . The form of  $U_J$  is sketched in Fig. 2.5. One can also write Eqn 2.38 as,

$$\frac{\ddot{\varphi}}{\omega_p^2} + \frac{\dot{\varphi}}{\omega_c} = i - \sin \varphi = -\frac{\partial u_J}{\partial \varphi} \quad (2.42)$$

OR

$$\beta_c \frac{\ddot{\varphi}}{\omega_c^2} + \frac{\dot{\varphi}}{\omega_c} = i - \sin \varphi = -\frac{\partial u_J}{\partial \varphi} \quad (2.43)$$

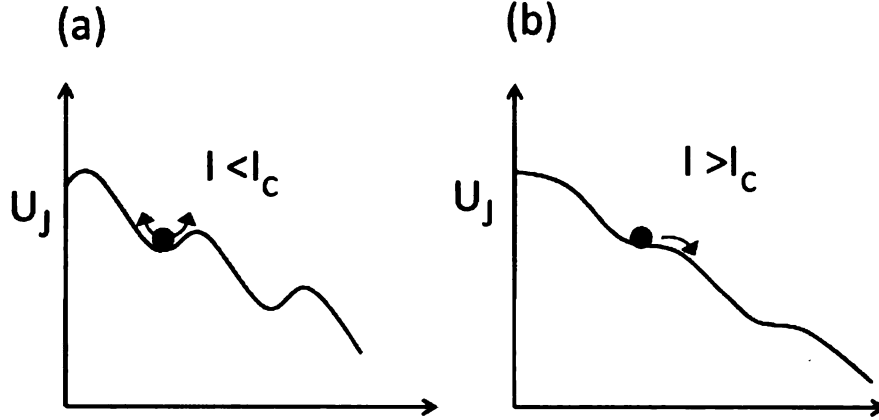


Figure 2.5: (a) When  $I < I_c$ , it is a static case where the particle is confined to one well and it oscillates back and forth with plasma frequency,  $\omega_p$ . (b) When  $I > I_0$ , the local minima disappears and the phase evolves in time. This dynamic case is what is associated with a finite DC voltage  $V$  across the junction which increases with increasing bias current.

where, we introduced Stewart McCumber parameter  $\beta_c$ ,

$$\beta_c = \left( \frac{\omega_c}{\omega_p} \right)^2 = \frac{2\pi}{\Phi_0} I_c R^2 C \quad (2.44)$$

with  $\omega_p = \sqrt{(2\pi I_c)/\Phi_0 C}$  as the plasma frequency,  $\omega_c = (2\pi I_c R)/\Phi_0$  as the Josephson frequency at the characteristic voltage  $V_c \equiv I_c R$  and  $u_J = U_J/E_J$  as the normalized potential. In the static case,  $I < I_c$ , the particle is confined to one well and it oscillates back and forth with plasma frequency  $\omega_p$ . If  $I > I_c$ , the local minima disappears and the phase evolves in time. This dynamic case is what is associated with a finite DC voltage  $V$  across the junction which increases with increasing bias current.

### Overdamped vs Underdamped Junctions

Based on the relative size of  $\omega_p$  and  $\omega_c$ , one can identify two different kind of Josephson junctions.

- **Underdamped Josephson Junctions:** When the barrier is an insulator, the

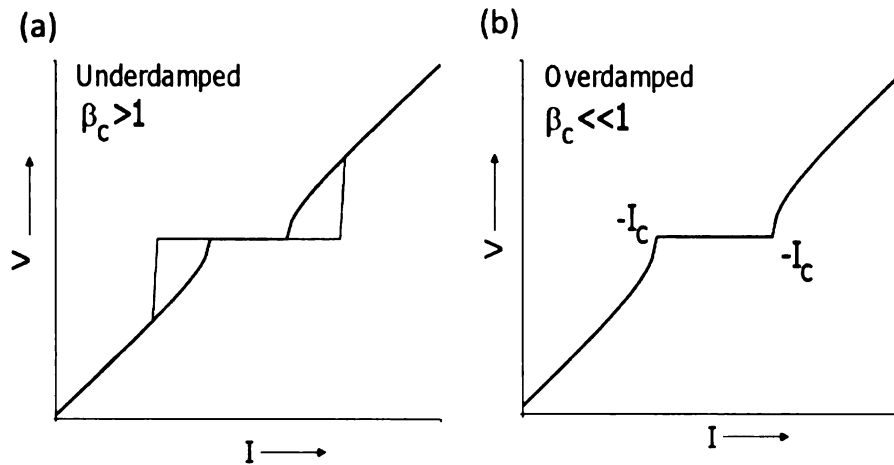


Figure 2.6: (a)  $I$ - $V$  characteristics of a hysteretic underdamped junction ( $\beta_c > 1$ ). (b)  $I$ - $V$  characteristics of an overdamped junction ( $\beta_c \ll 1$ ).

junction's internal resistance is very large. In this case  $\beta_c > 1$  and the junction characteristic is hysteretic. This is also shown in Fig. 2.6.

- **Overdamped Josephson Junctions:** When the barrier is conducting, the effect of the junction's internal resistance will be large compared to its small capacitance. In this case  $\beta_c \ll 1$  and the Josephson effect looks like as shown in Fig. 2.6b. All of the Josephson junctions studied in this thesis showed overdamped junction characteristics.

### 2.6.3 Effect of Magnetic Field

#### Fraunhofer Pattern for a Circular Josephson Junction

To understand the effect of an applied magnetic field on the Josephson effect, we will consider a circular Josephson junction with a non-superconducting layer i.e. with an insulating or a normal barrier. Apply a magnetic field of induction  $B(x)\hat{z}$  along the  $z$ -axis in the plane of the junction as shown in Fig. 2.7. The vector potential in

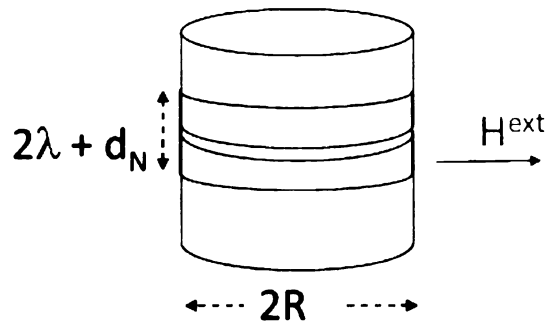


Figure 2.7: *Circular Josephson junction in a magnetic field. Field applied in the plane of the junction penetrates the London penetration depth  $\lambda_L$  into both the superconductors.*

London's gauge is,

$$\mathbf{A} = -B(x)y\hat{\mathbf{x}} \quad (2.45)$$

In the insulating layer,  $B(x)$  varies only slightly, and so one can consider  $B(x) \approx B(0)$ . Whereas, in the superconducting layer, magnetic field decreases as  $\exp(-x/\lambda_L)$ . The phase difference induced by the magnetic field is therefore given by,

$$\int_B^A A_x dx = B(0)yl \quad (2.46)$$

with  $l = 2\lambda_L + d$ , where  $\lambda_L$  is the London penetration length and  $d$  is the thickness of the insulating layer. The total phase difference across the junction is therefore given by,

$$\gamma = \Delta\theta + \frac{2\pi}{\Phi_o} \int_B^A A_x dx \quad (2.47)$$

where  $\Delta\theta = \theta_1 - \theta_2$  and  $\Phi_o = h/2e$ . The Josephson supercurrent density is therefore

given by,

$$J(y) = J_c \sin(\gamma) = J_c \sin\left(\Delta\theta + \frac{2\pi}{\Phi_0} \int_B^A A_x dx\right) \quad (2.48)$$

$$J(y) = J_c \sin\left(\Delta\theta + \frac{2\pi B y l}{\Phi_0}\right) \quad (2.49)$$

The critical current that we measure is given by,

$$I = \int J(y) dy dz \quad (2.50)$$

$$I = 2 \int_{-R}^R \sqrt{R^2 - y^2} J(y) dy \quad (2.51)$$

Substituting Eqn.2.49 in the above equation gives,

$$I = 4J_c \int_0^R \sqrt{R^2 - y^2} \sin\left(\Delta\theta + \frac{2\pi B y l}{\Phi_0} u\right) dy \quad (2.52)$$

For simplification let us substitute  $u = y/R$ ,

$$I = 4J_c R^2 \int_0^1 \sqrt{1 - u^2} \sin\left(\Delta\theta + \frac{2\pi R l B}{\Phi_0} u\right) du \quad (2.53)$$

$$I/I_c = \left| \frac{J_1(RlB/\Phi_0)}{RlB/\Phi_0} \right| \quad (2.54)$$

where,  $J_1$  is the Bessel's function of first kind and  $I_c = J_c \pi R^2$ . The resulting pattern is called an *Airy pattern*, and it is as shown in Fig. 2.8.

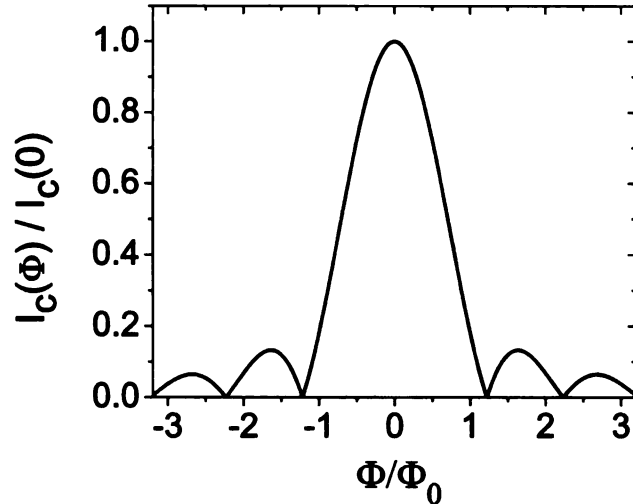


Figure 2.8: *Dependence of the critical current on enclosed flux for a circular Josephson junction yields an Airy diffraction pattern.*

### 2.6.4 Josephson Penetration Depth

$I_c(H)$  can be also modeled for non-uniform current flow, which is an important case when the junction dimensions are greater than the *Josephson penetration depth*,  $\lambda_J$ .

$$\lambda_J = \frac{\Phi_0}{\sqrt{2\pi\mu_0 J_c (2\lambda_L + d_F)}} \quad (2.55)$$

If  $\lambda_J < w/4$ , where  $w$  is the junction diameter, then the flux is screened from the center of the junction, and the effect of self field of the current cannot be neglected [56]. The  $I_c(H)$  can become asymmetric, and deviate from an ideal Fraunhofer-Airy pattern.

## 2.7 Ferromagnetic 0- $\pi$ Josephson Junctions

The current-phase relation of a conventional Superconductor/Insulator/Superconductor (SIS) Josephson junction is given by,  $I_s = I_c \sin\varphi$ , where  $\varphi = \theta_1 - \theta_2$  is the phase difference between the macroscopic superconducting wavefunction in each supercon-

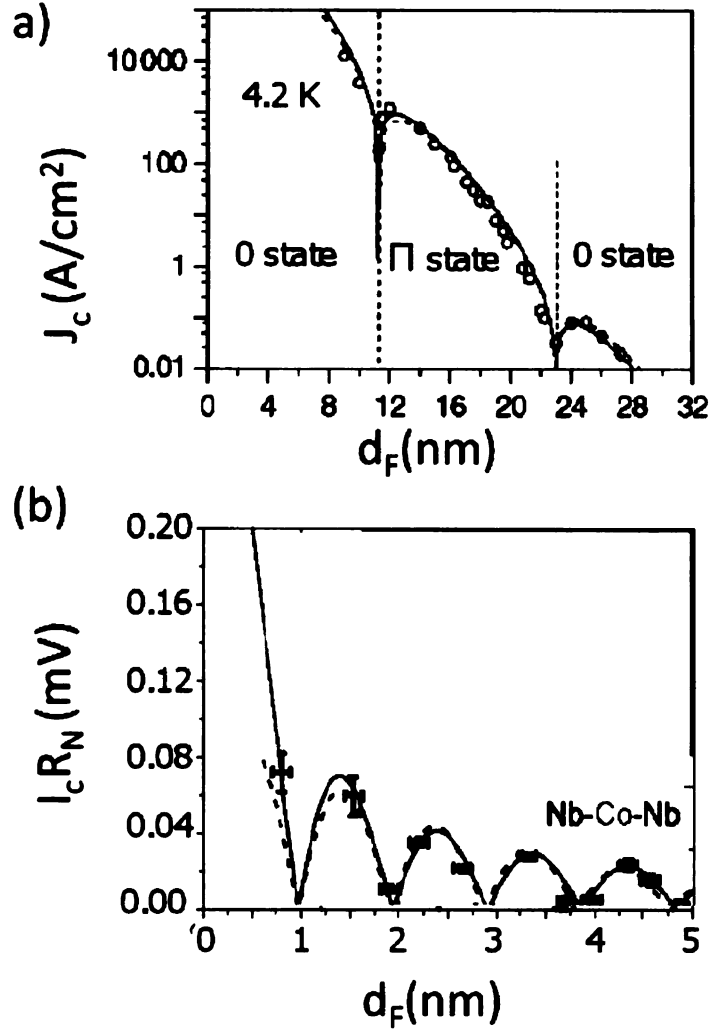


Figure 2.9: (a) Oscillatory dependence of critical current density as a function of CuNi thickness, (Taken from Oboznov et al. [26]). (b) Oscillatory  $I_c R_N$  as a function of Co thickness. (Taken from Robinson et al. [27])

ductor and  $I_c$  is the critical current. The Josephson coupling energy is given by  $U = -E_J \cos \varphi$ , where,  $E_J = (I_c \varphi_0)/2\pi$  is the *Josephson energy*. For conventional Josephson junctions the minimum Josephson energy occurs at  $\varphi = 0$ . In 1977, Bulaevskii *et al.* [57] calculated the critical current through a Josephson junction with magnetic impurities in the barrier and predicted a  $\pi$ -shift in the current phase relation for the certain concentration of impurities. The current phase relation of such junction is then given by  $I_s(\varphi) = -I_c \sin \varphi = I_c \sin(\varphi + \pi)$  and the Josephson energy is given by  $U = -E_J \cos(\varphi + \pi) = E_J \cos(\varphi)$ , indicating the existence of  $\varphi = \pi$  in the

ground state. Such a junction is called a  $\pi$ -junction.

The transition from 0 to  $\pi$  state in a S/F/S junction is the consequence of change in the sign of the oscillating pair correlations in the F layer. This leads to oscillation in the critical current as a function of ferromagnet thickness. This was first observed by Ryazanov and his co-workers [21, 26] using a weak ferromagnetic alloy CuNi, and later by Kontos *et al.* [23] using another weak ferromagnetic alloy, PdNi. Recently Blamire and his co-workers [27, 28] have published data showing the oscillatory Josephson critical current  $I_c$  as function of F-layer thickness using strong ferromagnets, Ni, Co, Fe, Py. Figure 2.9 shows oscillatory critical current as a function of F-layer thickness for the case of weak ferromagnet, CuNi [21], and for the case of a strong ferromagnet Co [27]. The data clearly show the transitions between the “0-state” and “ $\pi$ -state” as the F-layer thickness is increased.

## 2.8 Domain Structure of Ferromagnetic Interlayer

For quite a long time theoretical studies of ferromagnetic Josephson junctions and the effect of the exchange field disregarded the domain structure of the ferromagnetic interlayer. But recently there have been studies on how the domain structure would affect the junction properties. Throughout the course of this project our idea was to work with macroscopic samples. We believed that the multidomain structure in macroscopic samples can provide us the magnetic inhomogeneities necessary for the generation of LRTC. In this section I will talk about the domain structure in a ferromagnetic layer.

In a ferromagnet, the exchange energy tends to align the electron spins and hence the magnetic moments parallel to each other. A magnetized ferromagnetic material containing a single domain has a macroscopic magnetization, as shown in Fig. 2.10(a). It causes the block to behave as a magnet with a magnetic field around it.

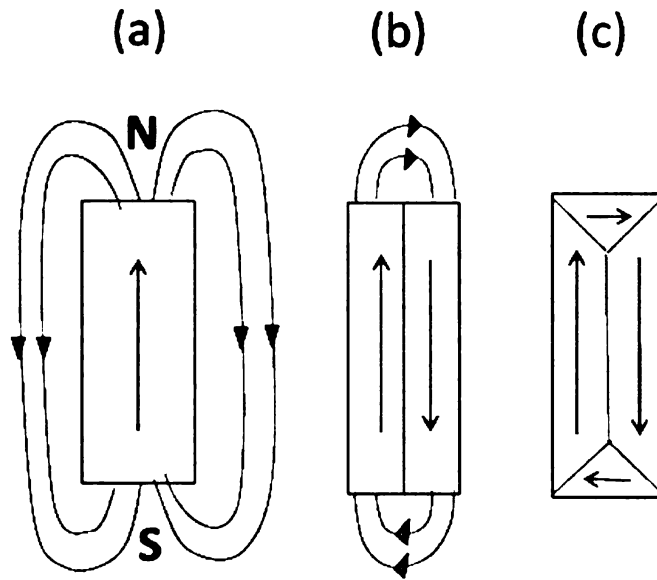


Figure 2.10: *Reduction of the magnetostatic energy by domain formation in a ferromagnet.*

This configuration has large magnetostatic energy. The magnetostatic energy can be reduced by formation of domains as shown in Fig. 2.10(b). This increases the exchange energy as the neighboring electron spins in the interface between the two domains cannot point in the same direction. To reduce the magnetostatic energy further, one needs the magnetic pattern as shown in Fig. 2.10(c). The domains near the end are called *closure domains*. Various other contributions to the total energy such as magnetocrystalline and magnetostrictive energy also influence the shape and the size of the domains.

The boundaries between the adjacent domains are called *domain walls*. The width of the wall is determined by the competition between the various energies. The exchange energy is optimized if adjacent spins are parallel and so the system tries to minimize the angle of moments between adjacent planes of atoms, thus forming a wide wall in which the angle changes gradually. But magnetocrystalline energy tends to point the magnetic moments along certain preferred directions called *easy axes*

and hence prefers to have an abrupt change in the direction of magnetization.

There are two kinds of domain walls, Bloch walls and Neel walls. In a Bloch wall the magnetization rotates around the axis perpendicular to the domain wall, whereas in a Neel wall, the spins rotate around the axis normal to the surface of the film. This is shown in Fig. 2.11. The existence of one of the two kinds of walls depends on factors such as magnetostatic energy, thickness of the film, anisotropy of the film, etc.

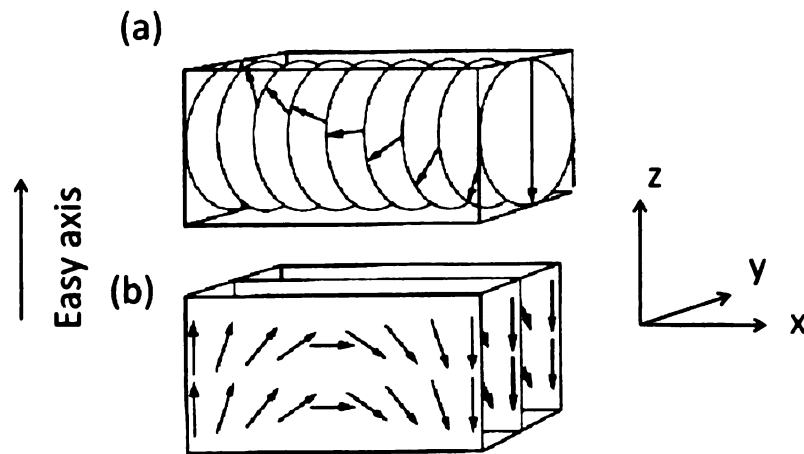


Figure 2.11: Assume that  $X$ - $Z$  is the plane of the film. Schematic of (a) Bloch Wall and (b) Neel wall.

As the thickness of a magnetic film decreases, the magnetostatic energy of a Bloch wall that extends through the thickness of the sample increases as a result of free poles at the top and bottom of the wall. To reduce this magnetostatic energy, the spins in the domain wall rotate parallel to the film plane. Although this indicates that Neel walls are more likely in the thin films we are studying, there is no way to know definitely the exact nature of the domain walls in our sample. Generation of LRTC in various S/F structures with Neel and Bloch-type domain walls has been studied theoretically [33, 8].

Thus in a realistic situation, the magnetization of any ferromagnet can be quite inhomogeneous due to the existence of domain walls. Existence of such inhomogeneities can cause triplet correlations to arise in the domain walls and spread into the domains over a distance of the order  $\xi_T = \sqrt{\hbar D / (2\pi k_B T)}$ , as predicted in Ref. [8]. The correlations are very sensitive to the thickness of the wall. A very thin domain wall will cause the magnetization vectors in the adjacent domains to be nearly collinear and will lead only to the penetration of singlet and short-range triplet component. A very thick wall on the other hand causes the magnetization that is nearly uniform on the scale of superconducting coherence length ( $\xi_S$ ). It is therefore important to have a wall thickness of an order of the superconducting coherence length for the odd triplet correlations to occur in the superconductor.

## 2.9 Our Approach

Our primary strategy in the detection of long-range triplet correlations was to create S/F/S Josephson junctions and systematically increase the F-layer thickness to the point where the conventional spin-singlet correlations are exponentially small. If we observe a supercurrent that continues to persist for thicker F-layers, it will be a strong evidence of spin-triplet correlations. Since the length-scale of decay for singlet correlations is different from the length scale of decay for triplet correlations, one should also observe a clear change in slope as is shown in Fig. 2.12. In the absence of magnetic inhomogeneities in the F-layer, no LRTC will be generated and consequently there will be no change in slope. Also, as said earlier, the spin singlet correlations are known to show an oscillatory behavior of critical current as a function of F-layer thickness, however no oscillations will be observed when the supercurrent is dominated by spin-triplet correlations.

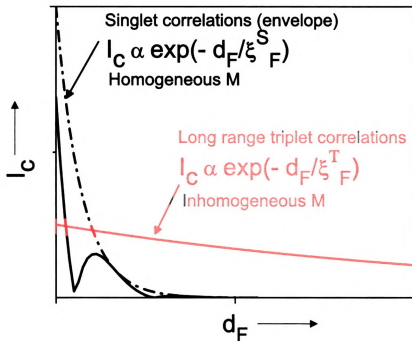


Figure 2.12: Our approach for the study of LRTC using S/F/S Josephson junctions. For small thickness of F-layer,  $I_C$  oscillates and decays on a short length scale  $\xi_F$ . For large thickness of F-layer and in the presence of magnetic inhomogeneities, LRTC takes over and  $I_C$  decays over a longer length scale without any oscillations. A change of slope would be a clear indication of LRTC. In absence of magnetic inhomogeneities in F-layer only short-scale oscillatory decay will be observed.

# Chapter 3

## Experimental Methods

This chapter will discuss the details of the sample fabrication process. During the course of this work several different kinds of sample were made - but here, I will specifically discuss the sample fabrication process used in making Josephson junctions. As for the GMR samples, the sample fabrication process has already been discussed in recently published theses [58, 59].

### 3.1 Sample Fabrication

The sample fabrication process can be roughly divided into following parts (See Fig.3.1),

1. Sputtering the multilayer
2. Photolithography
3. Ion milling
4. Silicon monoxide ( $\text{SiO}_x$ ) deposition
5. Lift-off

## 6. Sputtering top leads

A 3" Si (100) wafer is obtained from Silicon Quest International. It has a thickness of around 400  $\mu\text{m}$  and resistivity of about 1-10  $\Omega\text{cm}$  at room temperature. The wafer is spin coated with S1813 resist at 4000 RPM for 40 sec and baked at 95°C on a hotplate for 2 minutes. The resist layer in this step just acts as a protective layer, protecting the samples against any damage during the wafer cutting process. The 3" wafer is cut then into 0.5" x 0.5" substrates. The substrates are then ultrasonically cleaned in hot acetone (60 °C) to remove the resist, followed by an ultrasonic cleaning in alcohol and DI water. The substrates are then blow-dried using nitrogen gas.

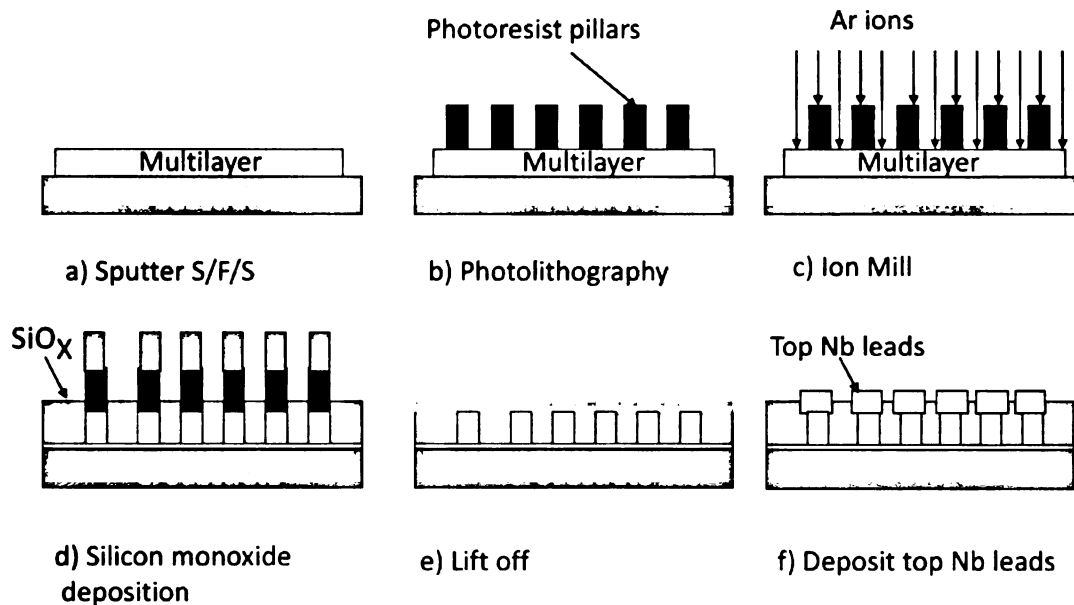


Figure 3.1: (a) *Sputtering Multilayer*, (b) *Photolithography*, (c) *Ion milling*, (d)  *$\text{SiO}_x$  Deposition*, (e) *Lift-off*, (f) *Top-Leads Sputtering*

### 3.1.1 Sputtering

We use the sputtering method to create a thin film multilayer of S/F/S type. Our sputtering chamber has six gun positions that allow us to sputter six different mate-

rials in a single pump-down. Four out of the six gun positions are large triode sources whereas the remaining two are small magnetron sources. The required sputtering targets and the target housings are mounted into the chamber as shown in Fig. 3.2. The sputter confining chimneys are placed over the target housings to avoid any cross contamination between different targets. A computer controlled rotating target plate is placed just above the chimneys which either opens or closes all the target positions simultaneously. Another computer controlled rotating substrate plate (called SPAMA plate) hangs upside down from the top of the chamber. This substrate plate has 8 substrate-holder positions. The typical substrate holder used for making Josephson junctions is shown in Fig. 3.3. A metallic multilayer of any desired shape and size can be made by placing a thin metallic mask (shadow mask) in close proximity with the substrate. The shadow mask used for creating Josephson junctions is a long rectangular strip of size 10.10 mm x 0.16 mm. Each substrate holder has a rotating mask that can be rotated in-situ. This allows us to selectively open a single substrate at a time while still protecting the rest. The SPAMA plate also has two Sycon Instruments quartz crystal monitors that are used to monitor the deposition rates prior to deposition of each individual sample. The entire sample cleaning and loading procedure is done in a Class-100 clean room to avoid any dust particles on the substrate, which if present could possibly lead to shorts in the multilayer. Prior to the sputtering, the system is baked for 10-12 hours and pumped for 1-2 days. The base pressure thus obtained using a CTI Cryo-Torr high vacuum pump is about  $3-4 \times 10^{-8}$  torr. In addition, a cold trap (Meissner trap) operating at liquid nitrogen temperatures (77 K) is used to freeze most of the water vapor in the system an hour before sputtering. This achieves a pressure of  $2 \times 10^{-8}$  torr or better. A capillary tube in contact with the trap carries 750 - 1000 psi of cold nitrogen to heat exchangers on the substrate plate, thus maintaining the temperature of the substrate between  $-30$  and  $+30^\circ\text{C}$ .

After achieving the desired base pressure, argon gas is slowly leaked into the



Figure 3.2: *The sputtering chamber showing six gun positions- four of them are large triode sources whereas the remaining two are small magnetron sources. In order to avoid the cross contamination, the plasma is confined using chimneys.*



Figure 3.3: *This figure shows a typical substrate holder and a mask used in the Sputtering chamber. The substrate holder (shown on the right-hand-side) has two sample positions, only one sample is opened during the sputtering using the rotating mask (shown on the left-hand-side).*

chamber at a rate enough to maintain the pressure at about  $2.5 \times 10^{-3}$  torr. The sputter guns are then turned on and stabilized for 25-30 minutes. A side cross-sectional view of typical sputtering gun set-up is shown in Fig.3.4. Once the current is

passed through the tungsten coil, the magnets confine and direct the flow of electrons towards the anode. On their way to anode, the electrons strip the Ar gas atoms of the orbital electrons thus ionizing the gas and creating a plasma close to the target to be sputtered. Once the plasma is stabilized, a large negative voltage is applied to the target. This causes the positive ions of Argon to accelerate towards the target. This high-speed bombardment of Argon ions causes the sputtering (ejection) of target atoms. The resulting material gets deposited on the substrate when both the target plate and the mask of the substrate holder are opened and when it is sitting right above the desired target.

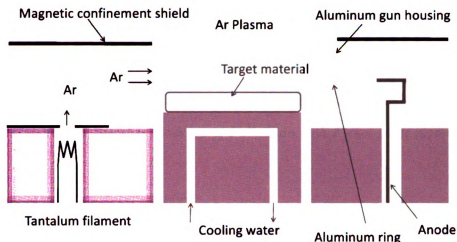


Figure 3.4: Side cross-sectional view of typical sputtering gun set up, consisting of filament (cathode), anode, and target. The magnets are placed on the sides (not shown here) such that the magnetic field is perpendicular to the plane of the paper.

### Special Alloy Targets

When using alloys like PdNi or PdFe, the target material is in itself not an alloy of desired combination. Special kind of targets were designed for such alloys. A base target of Palladium was drilled with holes of varied sizes. Ni (or Fe) and Pd plugs of the right dimension are then inserted into these holes to get the alloy with desired concentration. One can easily change the concentration of the alloys by replacing

some Ni plugs with Pd shots or vice versa. One such specially designed sputter-target is shown in Fig. 3.5. Our large triode source as opposed to the magnetron source of any form ensures the uniform mixing of the alloy components when they reach the substrate.



Figure 3.5: *The base target is made up of Palladium with Nickel plugs placed into the holes.*

### 3.1.2 Photolithography

After sputtering the S/F/S multilayer, the next step in the device fabrication is a photolithography process.

What is photolithography? In Greek, it literally means writing on a stone using light [Photo - light, lithos - stone]. Lithography was invented in 1796 by Aloys Senefelder. Lithography at that time was an artist's work. In the scientific world or in the IC industry photolithography is a process by which geometric shapes are transferred onto a Silicon chip.

The basic process is shown in Fig. 3.6. It involves coating the substrate with a photo-sensitive material called photoresist. The photo-resist is then baked at a certain

temperature that is characteristic of the kind of resist used. The baking process drives out the solvent from the resist and makes it photosensitive. The sample is then selectively exposed using a mask which acts like a stencil with desired features. The sample is then developed in a developer solution. If the resist belongs to “positive photo-resist” category, the exposed resist dissolves in the developer leaving the sample with unexposed resist in desired shapes and sizes. This process creates the circular resist pillars of varied dimensions on our metallic multilayer. We have experimented with different kinds of resists during the course of this experiment to find the optimum resist and the method that best suits our junction fabrication process. Details of this photolithography process using different resists are given in the Appendix-A. The resist pillars created in this step act as masks for the next two processing steps—Ion milling and  $\text{SiO}_x$  deposition.

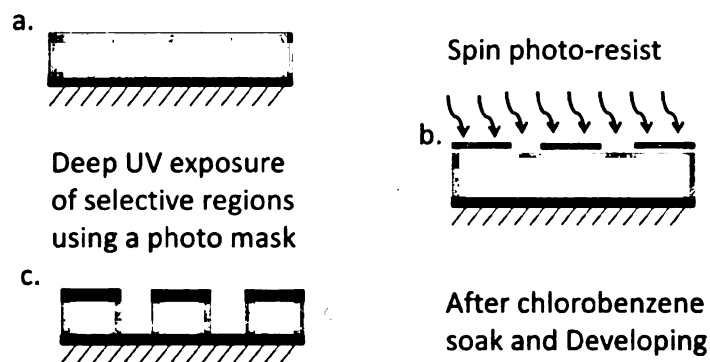


Figure 3.6: *Basic steps in the creating resist pillars are- (a) Resist coating, (b) Deep UV exposure using a photo-mask, (c) Developing in a photodeveloper.*

### 3.1.3 Ion Milling

After creating the photoresist pillars, samples are loaded into an ion mill chamber. Base pressure of  $2 \times 10^{-8}$  torr or better is achieved by pumping overnight using a turbo pump. Ion milling is done at  $2 \times 10^{-4}$  torr argon pressure using a 3”

Commonwealth Scientific Argon Ion beam source. The resist layer created via the photolithography process serves as a mask in the ion milling process. Ion milling being purely a physical process results in a high-resolution anisotropic etching of materials.

Our substrate plate is also equipped with a film thickness monitor. Prior to ion milling a sufficient amount of Au is deposited on the film thickness monitor, which later is used to measure the ion mill rate by placing it just above the ion mill gun. Test samples were made to measure the etch rates of different materials relative to Au etch rates. Knowing the Au etch rate and the relative etch rates of different materials, the milling time for our samples could be easily calculated. In order to avoid shorts due to back sputtered Nb, milling was done only until the middle of the ferromagnetic layer.

### **3.1.4 SiO<sub>x</sub> Deposition**

After ion milling, SiO<sub>x</sub> deposition is done in the same chamber without breaking the vacuum. This avoids shorts in the junctions due to exposure of substrates to the dust particles in air.

During evaporation, SiO<sub>x</sub> has a tendency of spitting and spalling, which leads to pinholes in evaporated thin films. To avoid this problem, boats in the form of “baffled boxes” are obtained from the R.D. Mathis Company. The baffled box has two cavities, of which one contains SiO<sub>x</sub> crystals and is closed, while the other is open. When heated, the SiO<sub>x</sub> travels an indirect path via a series of baffles from the closed cavity into the open cavity, which then acts like an exhaust chimney for the vapors. The substrate never sees the bulk material. This avoids particulates from the vapors and reduces the chance of pinholes in the evaporated thin films. A typical baffled-box used here is shown in Fig. 3.7.

The SiO<sub>x</sub> layer acts as an insulating layer that separates the bottom Nb layer from the top Nb layer sputtered in the end.



Figure 3.7: A typical “baffled-box” used for  $\text{SiO}_x$  deposition obtained from R.D. Mathis Company is shown here.

### 3.1.5 Liftoff

After the resist pillar fulfills its job as a mask during the ion milling and the  $\text{SiO}_x$  deposition process, it is removed by dissolving it in Remover-PG. This process is called a lift-off. The  $\text{SiO}_x$  deposition covers the substrate uniformly. To be successfully able lift off the photoresist pillar, it is important that the lift-off liquid finds a way to reach the resist pillar. Having a negative resist profile or an undercut (an umbrella like structure) in the resist profile facilitates the lift-off process. This is also shown in Figure A3 in Appendix-A.

### 3.1.6 Top Leads

After lift-off, the substrates are ion-milled to remove a thin layer of top Au ( $\sim 5$  nm). This step removes the residual-resist and the oxides from the top Au surface. 200 nm of Nb leads are then sputtered over the pillars using a shadow mask as shown in Fig. 3.8. The layout of the lithographed features is designed such that each lithographed pillar aligns well with each open window in the top mask. In the end a thin protective Au layer (15 nm) is sputtered over the top Nb leads to prevent oxidation.

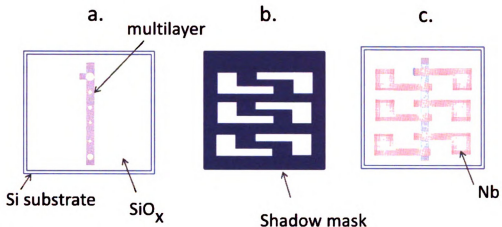


Figure 3.8: (a) The multilayer pillars (exaggerated sizes) after the lift-off step. (b) A metallic shadow mask used for the deposition of top Nb. (c) Final sample after sputtering the top Nb leads on the multilayer pillars.

## 3.2 Fabrication Issues

A successful photolithography technique is not one that merely yields a successful design transfer on to the chip, but is one in which resist can be successfully stripped off after serving its purpose. The prime factors that decide the appropriate photolithography process are undercut in the resulting resist profile, uniformity and reproducibility of the technique used, and sustainability of that structure under various experimental conditions.

### 3.2.1 Undercut

Ideally, a single layer photolithography is expected to yield a resist pattern with straight side walls that are perpendicular to the substrate. However when working with single chips of  $0.5'' \times 0.5''$ , the resist accumulation at the edge of the substrate can be as thick as  $30\text{-}40\ \mu\text{m}$ . This makes it difficult to make a hard contact between the substrate and the photomask, thus resulting in resist side walls with positive slopes. During the process of material deposition, the material gets accumulated on

the top as well as on the side walls of the resist, thus leaving no possible pathway for the lift-off liquid to reach the resist. Special techniques are therefore used to get a good undercut. The undercut structure protects the resist side walls from the deposited material ( $\text{SiO}_x$ ) and thus facilitates an easy lift-off of the resist (see Appendix A, Fig. A1-A3).

### 3.2.2 Back Sputtering

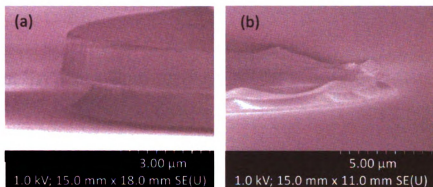


Figure 3.9: (a) The resist pillar before ion milling, (b) Back-sputtered material accumulated at the edge of a resist pillar (picture taken after an attempted lift-off).

During the ion milling process back-sputtered etched material can land on the side walls of the resist pillars and render it difficult to be dissolved in the lift-off liquid. Fig. 3.9 shows an SEM picture of the back-sputtered material at the edge of a resist pillar after the lift-off process. Using an ultrasonic process during lift-off helps in breaking off the back-sputtered material but is not guaranteed. Usually having a large undercut solved the problem of hardened resist edges. In addition, special care was taken to avoid etching the bottom Nb-layer, which if back-sputtered could lead to a short-circuit in the Josephson junction. In all the samples made during our studies, the etching process was discontinued after etching halfway through the ferromagnetic layer.

### 3.2.3 Dust particles

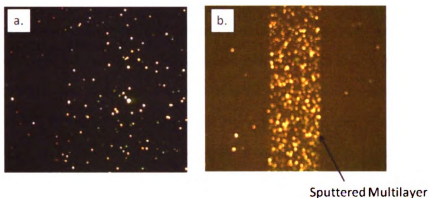


Figure 3.10: (a) Dust particles seen as seen the dark field under optical microscope. (b) A multilayer strip with dust particles.

A dark field image of samples that were not processed in the cleanroom showed dust particles as seen in the Fig. 3.10 below. This was a big step in realizing that the dust particles were the major cause of shorts in multilayers made during the initial stage of our project. After this finding, all our samples were processed in a Class-100 cleanroom.

## 3.3 Reactive Ion Etching (RIE)

One of the ways to etch materials is to use reactive ion etching (RIE) process. RIE uses a chemically reactive plasma to etch the materials. Purely physical etching processes like ion milling are anisotropic, whereas chemical etching processes like wet etching are highly isotropic. RIE implements both chemical as well as physical etching of the sample. Physical anisotropic etching processes like ion milling yield ideal sharp features, however such processes are not material sensitive which make the end-point determination difficult.

We use a PX-250 Plasma Etcher for the RIE process. It is equipped with a solid state RF generator with a fixed frequency of 13.56 MHz. The chamber consists of three Aluminum plates; the center plate acts as a powered shelf, whereas the outer two act as ground shelves. Plasma is generated under low pressure (vacuum) by an electromagnetic field. High-energy ions from the plasma attack the wafer surface and react with it. Since RIE is a chemically sensitive process, different gases can be used to etch different materials. For example, SF<sub>6</sub> gas is used to etch Nb. Prior to the actual etching process, the chamber is cleaned by running an oxygen descumming process. In the descumming process, oxygen is bled into the chamber and a pressure of 500 mtorr is obtained. RIE is turned on for 10 min with an applied power of 300 W to clean the resist debris and the other organic impurities in the system. The sample to be etched is then loaded on the powered shelf and the system is pumped to its base pressure. In order to ensure complete removal of impurity gases in the system, it is then purged with SF<sub>6</sub> gas and pumped again. This process is repeated 2-3 times prior to the actual etching of the sample. For the actual etching process, SF<sub>6</sub> is bled into the chamber at the rate of 50 sccm (220 mtorr). RIE is then turned on with a power of 65 W and the etching is performed for a fixed amount of time. After several etching attempts, we found that the etch rates varied from sample to sample as well as from run to run. Currently our RIE system is equipped with an ordinary mechanical pump that allows us to reach a base pressure of only about 20 mtorr. The possibility of contaminating gases in our system cannot therefore be ruled out. We believe this as a possible reason for our process inconsistencies. Although it is hard to identify the source of the polymeric residues found on our samples, we suspect them to be the reaction bi-products of the silicon substrate. In future, a better vacuum pump and use of quartz substrates instead of silicon substrate could possibly help in solving the current problems. However, due to the absence of any consistent results with the current set-up, we decided not to pursue this etching method any further.

### 3.4 Magnetic Force Microscopy (MFM)

In our search for odd triplet superconductivity in SFS systems, it was essential to search for appropriate ferromagnetic materials that have inhomogeneous magnetization. In as-deposited thin ferromagnetic films, the magnetic inhomogeneity could arise due to rotating magnetic moment in the domain walls or due to inhomogeneous spatial variation of the magnetization in adjacent domains. The length scale of these inhomogeneities is not known *a priori*, however various techniques can be used to probe this information. In order to understand the magnetic structure of the ferromagnetic materials, we choose to do Magnetic Force Microscopy (MFM). MFM is a technique which gives an image of magnetic structure of the sample surface. It is a form of atomic force microscopy where a sharp magnetic tip is used to scan the surface of the magnetic sample. The image taken contains information about both the topography as well as the magnetic structure of the sample; which effect dominates depends on the sample-tip separation. The strong magnetic forces that reflect the magnetic structure of the surface persists for greater tip-to-sample separations than the weaker van der Waals forces that give the topographic image of the surface.

In a standard AFM operating mode that gives the topography, the cantilever is operated near its resonance frequency. The vertical position of the scanner that corresponds to constant oscillation amplitude of the cantilever is stored to form the topographic image of the sample surface. Tip-sample interaction is maintained by using a feedback that keeps the oscillation amplitude constant. The resulting variation in the tip height forms the topographic image of the sample surface. On the other hand in MFM mode, the phase of the oscillation is measured while keeping the tip height at a constant but larger value than that of the previous scan. Typically each single line scan is first made in topographic mode, which is then followed immediately by a MFM mode scan. The information obtained in the topographic scan mode is

used to maintain the constant but longer tip-sample distance in the MFM scan mode. This prevents breaking of the tip due to strong magnetic tip-sample interaction while still exploiting the long-rang nature of magnetic forces. The phase shift thus detected can be solely attributed to magnetic interaction between tip and sample. Most of the scanning probe microscopy techniques are based on the force or force derivative detection. If the  $E_{tip-sample}$  is an energy of the tip-sample interaction, the force on the tip is given by:

$$F = \nabla_z E_{tip-sample} \quad (3.1)$$

In MFM, the phase shift is proportional to the gradient of the magnetic force in the vertical direction,

$$\Delta \varphi \propto \nabla_z F \propto \nabla_z^2 E_{tip-sample} \quad (3.2)$$

MFM was done using the cantilevers with magnetic Co-Cr coating (NSC13/Co-Cr)

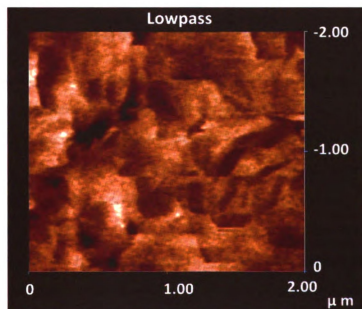


Figure 3.11: An MFM image of 7 nm thick Ni layer using a magnetic Co-Cr coated MFM tip.

obtained from MikroMasch. Fig. 3.11 shows the MFM image obtained for 7 nm of Ni deposited on 40 nm of Nb. Although it was hard to identify the orientation of magnetization in the domains walls in this picture it was clear that the domain size was no larger than a half a micron. It was not possible to find the domain wall width from the MFM study. But our calculations show that the wall thickness should be about  $\sim 12$  nm or less in Ni films at 4.2 K.

The currently housed facility allows us to do MFM only at room temperature. Since weak ferromagnetic alloys of our interest (PdNi, CuNi, etc.) have Curie temperatures that are below room temperature, a low temperature MFM measurement is necessary for such materials. The other available techniques that are not feasible in our laboratories include the Bitter method, magneto-optic Kerr method and SEMPA (Scanning electron microscopy with polarization analysis).

## 3.5 Measurements

### 3.5.1 Energy Dispersive X-ray Spectroscopy (EDS)

When a high energy beam of charged particles at 20 keV is focused onto the sample, the X-rays characteristics of the elemental composition of the sample are emitted. The elements in a sample can be determined by measuring the energy of X-rays produced. This technique is called as *Energy Dispersive Spectroscopy*. Typically an EDS system is attached to a Scanning electron microscope (SEM), Transmission electron microscope (TEM) or Scanning transmission electron microscope (STEM). The EDS system we use here is attached to a SEM system. SEM is used to create and focus a beam of electrons. A SiLi crystal detector operating at liquid nitrogen temperature is used to convert the X-ray energy into voltage signals. The signal is further processed by a pulse processor, analog to digital convertor (ADC), and a multichannel analyzer (MCA) which is then analyzed and displayed on the computer.

We have performed systematic EDAX measurement studies for weak ferromagnetic alloys like PdNi and PdFe.

### 3.5.2 Magnetic Measurements

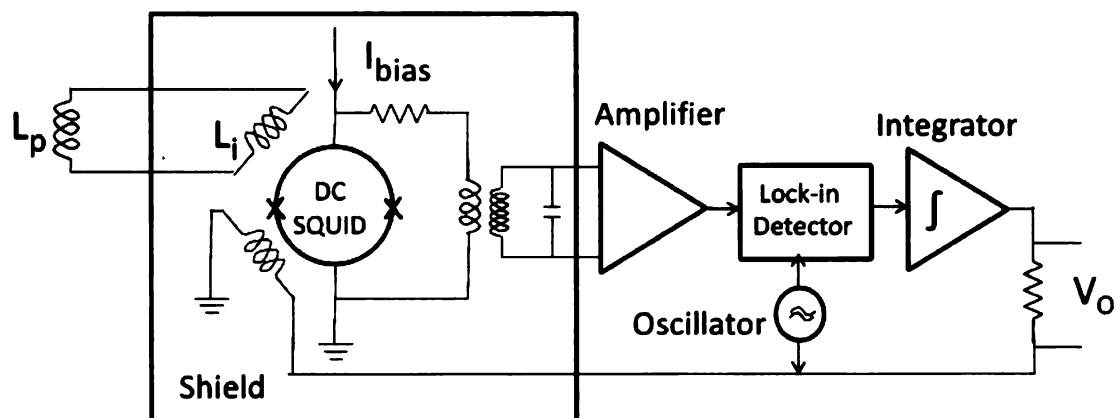


Figure 3.12: Superconducting pick-up coil couples the external flux to the input terminal of the SQUID. The SQUID acts as a linear current to voltage convertor. The magnetic moment of the sample causes the current variation in the detection coil  $L_p$  which then leads to corresponding variations in the SQUID output voltage.

For all the magnetic measurements we have used a superconducting quantum interference device (SQUID). The commercial system MPMS XL from Quantum Design provides the temperature in range from 2-400 K and magnetic fields up to 5.5 Tesla. The sample is mounted in a plastic straw and the measurement is performed by moving the sample between the superconducting detection coils. If the detection coil were a simple single or multiple-loop pick up coil (a magnetometer coil), it would be more susceptible to the environmental noise, i.e. noise due to sensitivity to the tilt in the earth's magnetic field, power line noise, RF interference, etc. Therefore the detection coil in this system is a second order gradiometer. Since magnetic fields fall off quickly (inverse cube( $1/r^{-3}$ )) with the distance, gradiometers take advantage of the fact that the field gradient due to a local source will be stronger than the field gradient due

to any distant source. The change in flux associated with the coil produces current that is inductively coupled to the SQUID via an input coil. The SQUID acts as a linear current to voltage convertor. The magnetic moment of the sample causes the current variation in the detection coil which then leads to corresponding variations in the SQUID output voltage. Fig 3.12 shows the dc-SQUID schematic used for our magnetic measurements. The sensitivity of the instrument was better than  $1 \times 10^{-8}$  emu. By changing the externally applied field, the magnetic moment of the sample changes, thereby causing a change in the SQUID response. This allows us to measure magnetization as a function of applied field (M vs. H). Measurements can be performed at any set temperature in the range from 2-400 K. In order to mimic the actual growth condition in Josephson junctions, most of the ferromagnetic thin films used for the magnetization study were also grown on thin niobium films. Care was taken to avoid the diamagnetic contribution of Nb by measuring these samples at temperatures higher than the superconducting transition temperature of the Nb.

### 3.5.3 Resistivity Measurements

The Josephson junctions studied in this work had lateral dimensions in the range of 10-40  $\mu\text{m}$  with their resistances varying in the range of 9-150  $\mu\Omega$ . They require an extremely sensitive low noise measurement technique which is provided by a SQUID.

Our sample is mounted on a Quick dipper probe, which is a long stainless steel metallic probe consisting of a sample holder with four probe leads, a superconducting magnet, a SQUID detector and a persistent switch. All the measurements are done at 4.2 K by dipping the Quick-dipper (QD) into a liquid helium dewar. Our SQUID-based resistance measurements rely on a “current-comparator” circuit which is shown in Fig. 3.13. The voltage sensitivity of our set up was about 1 pV. A small DC current,  $I_s$  ( $I_{max} = 100$  mA) is passed through an unknown sample with resistance  $R_s$ . The current through the reference resistance ( $R_{ref}$ ) is varied via the feedback circuit so as

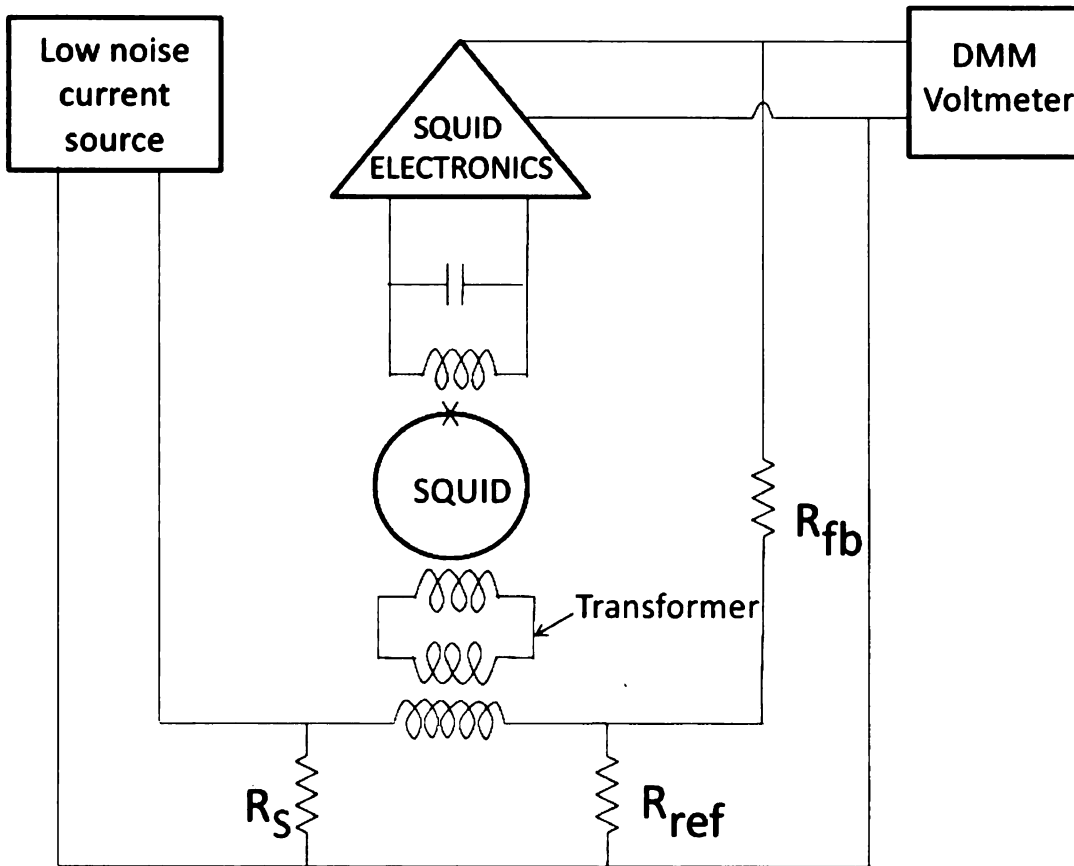


Figure 3.13: Schematic of the SQUID based current-comparator circuit used to measure resistances in the  $\mu\Omega$  range.

to balance the SQUID-based potentiometer setup. The voltage across the feedback resistance is recorded. The sample resistance can then be calculated by using the relation,

$$R_s = \left( \frac{V_o}{I_s} \right) \left( \frac{R_{ref}}{R_{fb}} \right) \quad (3.3)$$

Where  $V_o$  is the feedback output voltage of the SQUID electronics,  $R_{ref}=95 \mu\Omega$  is the reference resistor,  $R_{fb}=10 \text{ k}\Omega$  is the feedback resistance. Every sample has six Josephson junctions. Since all the Josephson junctions have a common bottom Nb layer, in order to measure any single pillar it's imperative to have three working

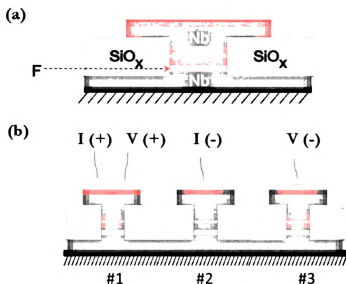


Figure 3.14: (a) Schematic of a S/F/S Josephson junction. (b) The critical current measurement of a single Josephson junction (#1) in fact requires us to make the lead connections to two of its neighbors (#2 and #3).

pillars on the sample. The Fig.3.14 shows the lead connections made to the three pillars. The contact to be measured (Pillar #1) is connected to both the current (I+) and the voltage lead (V+). The second contact (Pillar #2) is connected to another current lead (I-) and the third contact (Pillar #3) to another voltage lead (V-). The current flows from contact 1 to contact 2 without creating any voltage drop across the contact 3. Since Nb is superconducting at the temperatures we measure, the voltage leads measures only the drop across contact #1. The leads can be permuted so as to measure all the junctions on the sample.

### 3.5.4 Temperature Variation Measurements

A few experiments during this course of work were carried out to measure the critical current variation of the Josephson junction as a function of temperature.

The sample is mounted on the quick dipper rod as shown in Fig. 3.15. A vacuum-can is then sealed over the sample and pumped using a mechanical pump. The can

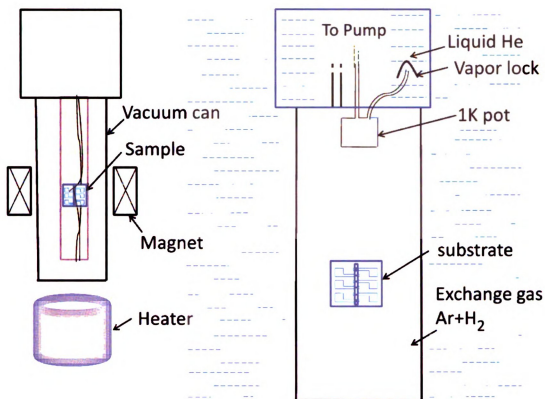


Figure 3.15: Schematic of low temperature measurement set-up. Measurements can be performed for the temperature range of 1.6-8.5 K.

is then filled with exchange gas containing Ar (90%)+ H<sub>2</sub> (10 %). The exchange gas acts as a heat exchange medium between the sample holder and the liquid helium outside the vacuum-can thus decreasing the temperature of the sample holder by the mere heat exchange process. A magnet and a heater is mounted by sliding them over the vacuum-can such that sample sits right in the middle of magnet. This heater is used during the dipping process to avoid freezing of the exchange gas. The 1K liquid He pot is then pumped and filled with He gas just before dipping the probe in liquid He so that the positive pressure prevents the air from entering the pot via the capillary connection to the He bath. When inside the liquid He, the 1K pot get filled with liquid He, and sample is at the liquid He temperature (4.2 K). To get the

temperatures lower than the liquid He temperature, the 1K pot is pumped. As the vapor pressure of the liquid He decreases, the temperature decreases. Temperatures as low as 1.6 K can be achieved by pumping on the liquid He. To work at temperatures higher than 4.2 K, a vapor lock is operated at the end of capillary connected to the 1K pot. This prevents the flow of liquid into the 1K pot. A balanced pumping and heating is used to achieve the desired temperature. Temperatures as high as 9 K can be achieved using one heater or as high as 20 K using two heaters. We have used this system to study the temperature dependence of the critical current for our S/F/S Josephson junctions.

# Chapter 4

## Spin-Singlet Superconductivity

When dealing with a fairly new physics problem, it is important to be able to separate out the known physics issues from the new unknown physics issues. Since this was our first experience working with Josephson junctions, we realized that it was important for us to establish a standard procedure that guarantees reliable Josephson junctions. In the past Ryazanov [21, 26] and his co-workers have extensively worked on Superconductor/Ferromagnet/Superconductor (S/F/S) Josephson junctions using a weak ferromagnetic CuNi alloy. Their work, apart from being a pioneering work in the S/F physics, has shown I-V characteristics and Fraunhofer patterns that are identical to the standard S/N/S (N-Normal metal) Josephson junctions. We therefore decided to take the plunge into this field by creating S/F/S junctions using a CuNi alloy and compare our results with those of Ryazanov.

### 4.1 CuNi Josephson Junctions: (Nb/CuNi/Nb)

#### 4.1.1 Characterization of CuNi Josephson Junctions

Our CuNi sputtering target consists of a 5.6 cm diameter target of pure Cu with several 6 mm diameter Ni plugs inserted into the target. This sputter target looks

identical to the one shown in Chapter 3, Fig. 3.5. CuNi alloys have been intensively studied in the past, and are known to show a transition from paramagnetic to ferromagnetic behavior with the increasing concentration of Ni. The past experiments have shown that the alloy is ferromagnetic for concentrations greater than 44 % [60]. EDAX measurements on our sample indicated Ni concentration of  $52 \pm 0.5\%$ .

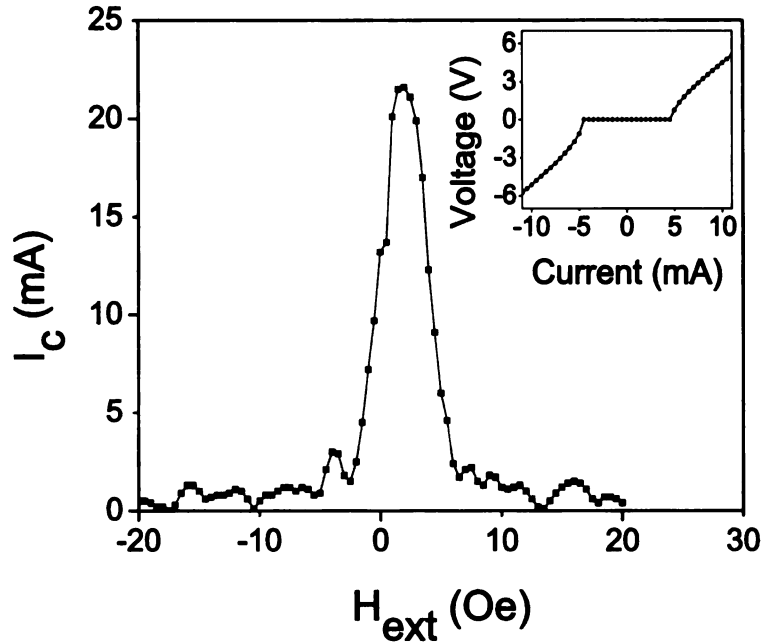


Figure 4.1: *Critical current  $I_C$  vs applied field  $H_{ext}$  for Nb/CuNi/Nb Josephson junction with  $d_{CuNi}=16$  nm. The lateral dimension of the pillar was  $50 \mu\text{m}$ . The inset shows  $I-V$  characteristics for the same junction.*

Fig.4.1 shows characteristic  $I_C$  vs  $H_{ext}$  (Fraunhofer pattern) obtained for a Nb/Cu<sub>0.48</sub>Ni<sub>0.52</sub>/Nb Josephson junction using Cu<sub>48</sub>Ni<sub>52</sub> alloy. (The inset in Fig. 4.1 shows the  $I - V$  characteristic of the junction.) The thickness of CuNi alloy was 16 nm and the lateral junction dimension (diameter of the circular pillar) was  $50 \mu\text{m}$ . The extremely low values of critical current at the minima indicate the absence of any shorts in the surrounding insulator. The qualitative nature of the Fraunhofer pattern as well as the  $I-V$  characteristic seen here is identical to what Ryazanov and co-workers have seen in Josephson junctions using CuNi alloy of a similar concentration.

### 4.1.2 Magnetizing CuNi Josephson Junctions

Since we were working with ferromagnetic Josephson junctions, we realized that it was important for us to understand the influence of the magnetic barrier on the observed Fraunhofer pattern. To study this, we decided to intentionally magnetize one of our Josephson junctions. Large in-plane magnetic field of 1000 Oe was applied to magnetize the CuNi layer at 4.2 K. To ensure that there are no trapped Abrikosov vortices in the Nb, the sample was then raised in the Helium dewar so that the temperature of the substrate was greater than the Nb transition temperature ( $T_c$ ) but less than the Curie temperature ( $T_{Curie}$ ) of the ferromagnet. The sample was then lowered back into the liquid helium dewar and  $I_c$  vs  $H_{ext}$  (Fraunhofer pattern) was then measured. We saw that the Fraunhofer pattern of thus magnetized samples shifts in field to the point where the flux due to an externally applied field cancels the intrinsic trapped flux of the magnetized layer. This is shown in Fig. 4.2.

To understand more about the observed shift, let us assume the F-layer to have a uniform magnetization  $M$  throughout the junction. The intrinsic magnetic flux in the junction is then given by,  $\Phi_F = 4\pi M d_F w$ , where  $d_F$  is the thickness of the F-layer and  $w$  is the lateral dimension junction (i.e. diameter of the circular junction). The total magnetic flux  $\Phi_{tot}$  through the F-layer is therefore the contribution from intrinsic magnetic flux  $\Phi_F$  and the flux due to an external magnetic field,

$$\Phi_{tot} = 4\pi M d_F w + H_{ext}(2\lambda_L + d_F)w \quad (4.1)$$

Since the field penetrates the London penetration length  $\lambda_L$  in the superconducting electrodes on both sides, the effective thickness seen by the magnetic field is  $2\lambda_L + d_F$ . The expected value of  $\lambda_L$  for our Nb was 86 nm.

When the sample is completely magnetized by applying a magnetic field in the positive direction, the observed peak of the Fraunhofer pattern shifts in field to a

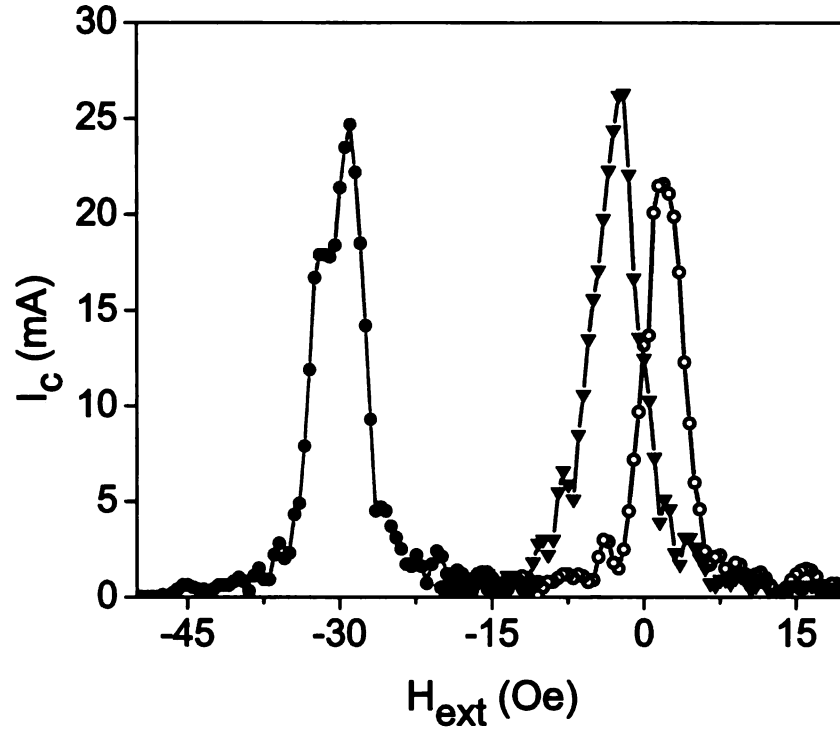


Figure 4.2: *Critical current  $I_C$  vs applied field  $H_{ext}$  for Nb/CuNi/Nb Josephson junction with  $d_{CuNi}=16$  nm. Black Triangles: Virgin State, Red Circle: After magnetizing, Blue Triangles: After demagnetizing sample*

point where the flux due to the external field cancels out the flux due to the intrinsic magnetization of the CuNi layer. This shift in the field can be calculated from the above equation by setting  $\Phi_{tot}=0$ .

$$H^{shift} = -\frac{4\pi M d_F}{(2\lambda_L + d_F)} \quad (4.2)$$

Fig. 4.2 shows 30 Oe shift in the Fraunhofer peak when CuNi is magnetized. Using the observed shift, one can then calculate the remnant magnetization ( $M_R$ ) in the junction using Eqn. 4.2. The  $M_R$  thus calculated from the observed shift was 32  $emu/cm^3$ . This value is much larger than the  $M_R$  of 10  $emu/cm^3$  seen in  $M$  vs.  $H$  measurements for an identical thickness of ferromagnet. This discrepancy may arise because the samples used in the  $M$  vs.  $H$  measurements were grown on a thin Cu layer

$\sim 5$  nm rather than on a thick Nb layer. We also observed that upon demagnetizing the sample, the Fraunhofer pattern returned close to its original position.

It is important to notice from Eqn. 4.2, that even in an absence of external magnetic field, the trapped flux in the junction can cause the Fraunhofer pattern to shift. This can cause the maxima in critical current to occur at non zero magnetic fields. Such a shift is also apparent in our virgin state Fraunhofer pattern seen in Fig. 4.2.

Our data were consistent with the work done by Ryazanov [61, 21], and this clearly demonstrates that our Josephson junction fabrication process is sound and reliable. Despite the excellent nature of the junctions, CuNi alloy was used only to test the device reliability.

### 4.1.3 Disadvantages of CuNi Alloy

Many groups have successfully studied S/F/S junctions using weakly-ferromagnetic alloys to reduce the exchange energy and consequently increase the characteristic coherence length  $\xi_F$ . Although using weakly ferromagnetic material allows us to increase the thickness of the ferromagnetic material, such alloys suffer from strong spin orbit and/or spin-flip scattering which is likely to destroy both the spin-singlet and spin-triplet correlations. In the past, Ryazanov and his co-workers [26] have worked with  $\text{Cu}_{47}\text{Ni}_{53}$  and found that the Josephson supercurrent in the CuNi layer decays over a length scale of only 1.4 nm. They also found that the supercurrent oscillates on a length scale of 3.8 nm. The fact that the length scale of decay is smaller than the length scale of oscillations indicates strong spin-flip scattering in this alloy [62, 63, 14, 33]. Several such experiments have been performed by other groups using weakly ferromagnetic alloy [22, 23, 64, 24]. Although no long range triplet corrections were seen, these experiments have successfully studied the  $0 - \pi$  transition of the critical current as a function of the F-layer thickness.

## 4.2 PdNi Josephson Junctions (Nb/PdNi/Nb)

As discussed in the previous section, there is strong spin-flip scattering in CuNi alloy [21, 26] which makes it an unfavorable candidate for the study of long range triplet superconductivity. In contrast, Kontos et. al. [23] worked with PdNi alloy and saw the same length scale of decay and oscillation ( $\xi_{F1} \approx \xi_{F2} \approx 2.8$  nm), which implied a possibility of less spin-flip and spin-orbit scattering in this material. We therefore decided to pursue this as our next possible candidate in the study of long range triplet correlations. The following sections in this chapter are based largely on our published paper Khaire *et al.*, Phys. Rev. B 79, 094523 (2009).

It's important to recognize here the different nature of magnetism in CuNi and PdNi alloy. Since Pd is “nearly” ferromagnetic itself according to the Stoner criterion it takes only a small concentration of Ni to make it ferromagnetic. By the virtue of small Ni concentration, one can expect the magnetism to be more uniform in PdNi alloy than the CuNi alloy, where the magnetism results from large clusters of Ni atoms.

In the past, Aprili [31, 23] and others [64, 65, 66, 67, 68] have extensively studied Pd<sub>1-x</sub>Ni<sub>x</sub> with Ni concentration of 12 at% but only with the PdNi thicknesses less than 15 nm. As mentioned earlier, the goal of our work is to increase the thickness of the F-layer and see the clear transition from the spin-singlet correlations to the spin-triplet correlations as the thickness of F-layer is increased. Our choice for this material was therefore governed by 2 factors: 1) A weak ferromagnetic alloy allows us to increase the thickness of the F-layer without introducing large amount of flux in the junction (Large flux in the junction can pose severe problems, this issue is discussed in detail in Chapter 6); 2) A possibility of less spin-flip and spin-orbit scattering in PdNi alloy compared to CuNi alloy allows the triplet-correlations to survive for longer distances in the F-layer.

### 4.2.1 Characterization of PdNi Alloy

The Ni concentration in our PdNi sample was confirmed by three different methods:

1. EDAX
2. Curie Temperature
3. Saturation magnetization.

Energy dispersive X-ray analysis of 1.5  $\mu\text{m}$  thick PdNi film yielded a Ni concentration of  $12\pm 0.5$  at.%. A thick film was used to ensure the large signal to noise ratio for the Ni-K peak. Similar EDAX measurements performed on a 200 nm PdNi sample yielded an identical concentration provided the signal was accumulated for long enough times to ensure large signal to noise ratio.

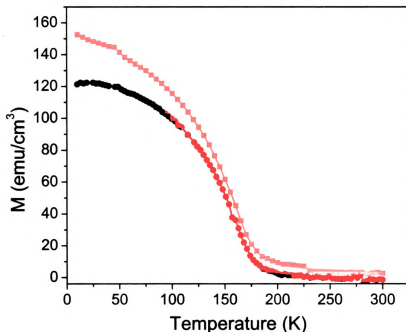


Figure 4.3: Magnetization vs. temperature for a 100 nm thick PdNi film. Then the magnetic moment was measured by applying magnetic field of 5 kOe while heating to room temperature. Black circles: In-plane field, Red squares: Out-of-plane field.

To confirm the measured concentration value, the magnetization  $M$  vs temperature of a 100 nm thick PdNi sample was measured using a superconducting quantum interference device (SQUID) magnetometer. The film was grown on 150 nm of Nb to have identical crystalline properties as our Josephson junction samples. The film was first cooled in zero field to 10 K, then the magnetic moment was measured by applying an in-plane field (or out-of-plane field) of 5 kOe while heating to room temperature. These curves are shown in Fig. 4.3. The cooling curves were also measured, and were found to follow the same curves as during heating (Not shown in Fig. 4.3). A clear change of slope is seen around the Curie temperature of the sample at around 175 K, independent of whether the field is applied in-plane or out-of-plane of the sample. According to the pervious literature published by Beille [69] and cited by Kontos [70], this Curie temperature corresponds to a Ni concentration of about 12%.

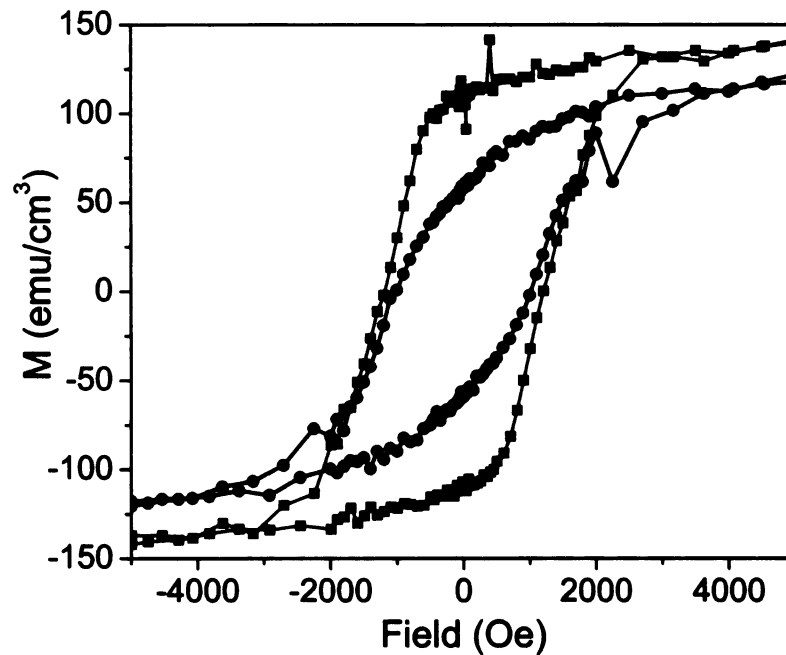


Figure 4.4: *Magnetization vs. in-plane field for 100 nm thick PdNi sample. Black circles: In-plane field and Red squares: Out-of-plane field. The measurement was done at 10 K.*

Figure 4.4 shows  $M$  vs  $H$  measured for the same 100 nm thick PdNi film at 10 K by applying field either in-plane or out-of-plane of the sample. In both cases the same saturation magnetization is obtained, but a larger field is required to attain the saturation when the field is applied in plane of the sample than when the field is applied out-of-plane of the sample. (Note: The saturation field is not visible in the field range plotted in Fig 4.4.) This indicates that the magnetic anisotropy of PdNi films is out-of-plane. Similar measurements performed on 30 and 60 nm PdNi films also indicate an out-of-plane anisotropy. Recently, similar out-of-plane anisotropy was observed in CuNi alloy [71, 72]. This is in contrast with what is usually seen in thin films. In thin films, the strong shape anisotropy dominates the magnetocrystalline anisotropy, which results in an overall in-plane magnetization of the film. The saturation magnetization of PdNi was about  $150 \text{ emu/cm}^3 = 0.23 \mu_B/\text{atom}$  (See Fig. 4.4), which according to Beille [69] and Kontos [70] corresponds to the Ni concentration of about 12%. Thus all the three methods of concentration determination indicated a Ni concentration of  $12 \pm 0.5\%$  in our samples.

#### 4.2.2 Characterization of PdNi Josephson Junctions

For a fixed thickness of PdNi, several S/F/S Josephson junctions of varying lateral dimensions (10 to 40  $\mu\text{m}$ ) were made on the same sample. Depending on the lateral dimensions, the normal state resistance of samples varied in the range from 2.4 to 152  $\mu\Omega$ . Resistance in this range require an extremely sensitive low noise measurement technique which is provided by a SQUID. All the four probe measurements were done at 4.2 K by dipping the sample into a liquid helium dewar. The measurement set-up has been described in detail in Chapter 3, section 1.5.

Figure 4.5 shows the typical  $I - V$  characteristics obtained for Nb/PdNi/Nb Josephson junction with diameter of 20  $\mu\text{m}$  and using  $d_{PdNi} = 62 \text{ nm}$  and  $H_{ext} = -19$

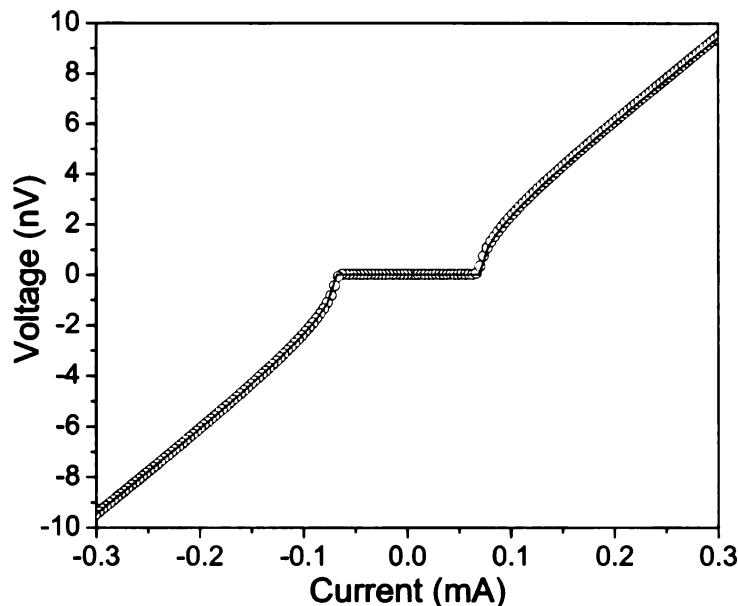


Figure 4.5: Voltage vs. Current for a PdNi Josephson junction with diameter  $20 \mu\text{m}$ ,  $d_{\text{PdNi}} = 62 \text{ nm}$  and  $H_{\text{ext}} = -19 \text{ Oe}$ . The red solid line is a fit to Eqn. 4.3

Oe. The red line is a fit to the standard I-V relation given by,

$$V(I) = \frac{I}{|I|} R_N \text{Re}[(I^2 - I_c^2)^{1/2}] \quad (4.3)$$

Occasionally, we have observed I-V curves that are shifted horizontally, so that the critical current in the positive is not exactly the same as the critical current in negative current directions. In such cases, we average the critical currents in the two current directions.

Figure 4.6 shows the typical  $I_c$  vs  $H_{\text{ext}}$  (Fraunhofer patterns) obtained for Nb/PdNi/Nb junctions with different thicknesses of PdNi (35, 50, 70, 85 nm). The extremely small values of critical current at the minima indicate absence of any shorts in the insulating material surrounding the Josephson junctions. Also it is important to note that the maxima in  $I_c$  are observed close to  $H_{\text{ext}} \approx 0$ . This indicates that the PdNi layers in the junctions have a multidomain structure which leads to a

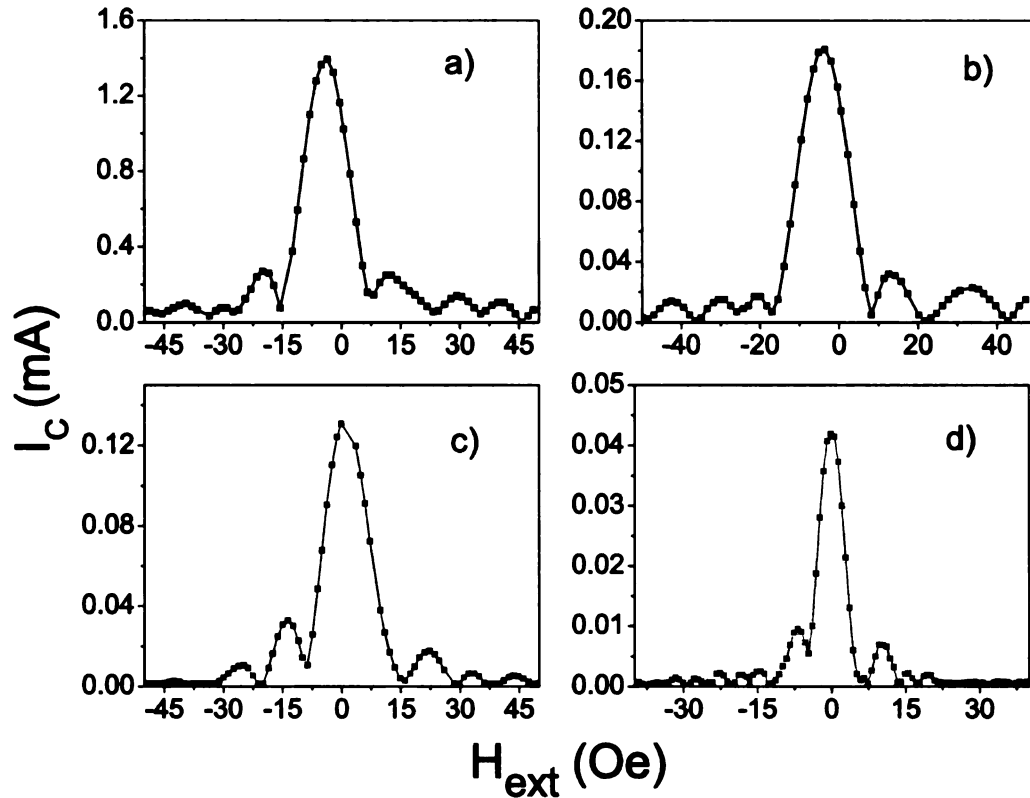


Figure 4.6: Critical current,  $I_C$  vs. applied magnetic field  $H_{ext}$  (Fraunhofer patterns) obtained for PdNi Josephson junctions with different thickness of PdNi interlayer a) 35nm, b) 50nm, c) 70nm, d) 85nm. The pillar diameters are 10, 10, 10, and 20  $\mu\text{m}$ , respectively.

highly homogeneous flow of current through the junctions. Occasionally  $I_C(H)$  was distorted or the central peak was shifted due to the residual magnetic flux trapped in the junction during the cooling process. The  $\mu$ -metal shield currently employed in shielding the sample from external fields is small and is sitting at the bottom of the dewar. When the liquid helium dewar is full, the sample undergoes a ferromagnetic transition ( $T_{Curie}$  of PdNi = 175 K) even before it reaches the  $\mu$ -metal shield, thus trapping residual magnetic flux due to extraneous sources. Usually heating it to the room-temperature (i.e. Pulling the sample to the top of the helium dewar) and re-dipping it in liquid helium, gains back the demagnetized state.

### 4.2.3 Magnetizing PdNi Josephson Junctions

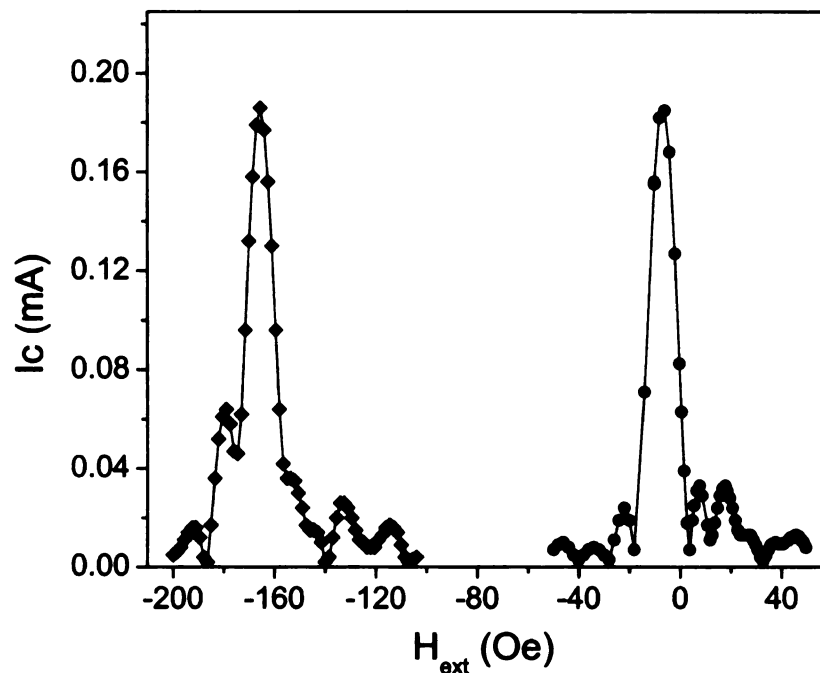


Figure 4.7: Fraunhofer pattern in the virgin state (red circles) and after magnetizing (black diamonds) a Nb/PdNi/Nb Josephson junction with diameter  $w = 10 \mu\text{m}$  and  $d_{\text{PdNi}} = 47.5 \text{ nm}$ .

$I_c$  vs  $H_{\text{ext}}$  measurements were also performed on all our samples after magnetizing the Josephson junctions. The samples were magnetized by applying a large in-plane field of 5 kOe and the sample was carefully lifted in the cryostat to just above the liquid helium level until the Nb electrodes showed a transition to the normal state. This step removed any trapped flux from the Nb electrodes or the superconducting magnet. Sample was then dipped back into liquid He and the Fraunhofer pattern was measured. As observed earlier in the case of CuNi, the peak of the Fraunhofer pattern was found to be shifted in field. One such shifted Fraunhofer pattern is shown in Fig. 4.7. The maximum critical current measured for magnetized samples matched closely with the maximum critical current obtained for virgin state samples.

Samples were magnetized by the procedure described above and the field shift

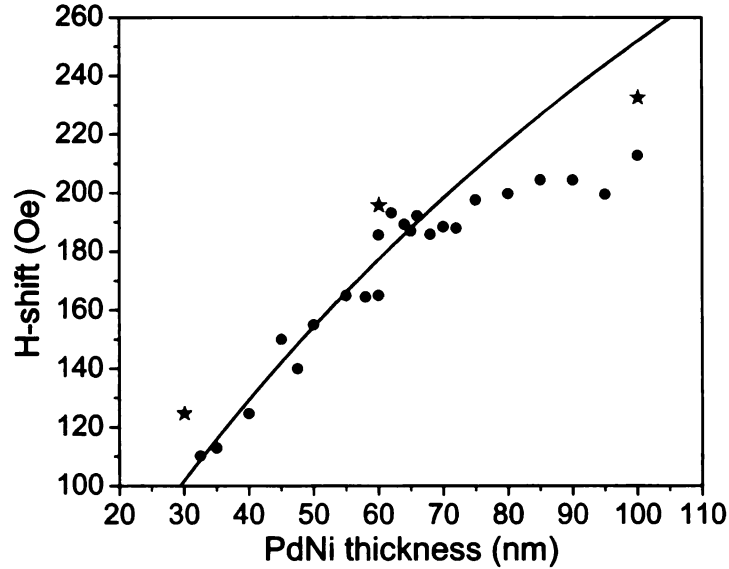


Figure 4.8: *Magnetic field shift of Fraunhofer patterns of magnetized samples vs. PdNi thickness  $d_F$ . The line is a fit of Eqn. 4.2 to the data points with  $d_F < 75$  nm, with  $\lambda_L = 86$  nm. The red stars indicate  $H_{shift}$  values calculated using the same Eqn. 4.2 but using  $M_{rem}$  values obtained directly from  $M$  vs.  $H$  data obtained for 30, 60, and 100 nm thick PdNi films.*

( $H_{shift}$ ) of the Fraunhofer pattern was measured for all our Josephson junctions with varying PdNi thickness. Fig. 4.8 shows the field shift of the Fraunhofer patterns obtained for Josephson junctions with varying thickness of PdNi layer. As the thickness of PdNi is increased, the field shift saturates at around 200 Oe. This is because, in thin films dominance of shape anisotropy leads to a strong preference for in-plane magnetization, however as the film thickness increased, dominance magnetocrystalline anisotropy over shape anisotropy leads to an increased tendency of magnetic moments to align perpendicular to the plane of the sample. This leads to a decrease in the in-plane component as the thickness is increased. Since  $H_{shift}$  is a measure of  $M_{rem}$  (in-plane component), increasing PdNi thickness leads to the saturation of the  $H_{shift}$  as seen in the Fig. 4.8. The solid line is fit to the data using Eqn. 4.2, using remnant magnetization  $M_{rem}$  as the only free parameter. The fit gives  $M_{rem} = 55$  emu/cm<sup>3</sup>. This value is comparable to the remnant magnetization

of 76 and 62 emu/cm<sup>3</sup> measured directly for PdNi films of thickness 30 and 60 nm respectively. The red stars in the figure are  $H_{shift}$  values calculated using the same Eqn. 4.2 with  $M_{rem}$  values obtained directly from the magnetization measurements done on PdNi films of thickness 30, 60 and 100 nm.

#### 4.2.4 Critical Current vs Thickness: $0 - \pi$ Josephson Junction

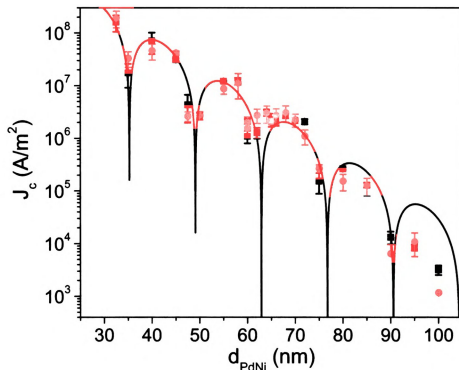


Figure 4.9: Critical current density ( $J_c$ ) vs. thickness of PdNi ( $d_{PdNi}$ ) for all of our Nb/PdNi/Nb Josephson junctions. Each data point is the average taken over multiple pillars on the same substrate and the error bars represent the standard deviation of the mean. Black points (squares) are virgin state data, while red points (circles) were measured after magnetizing the samples (see Fig. 4.8). The solid line is a fit of Eqn. 4.6 to the virgin state data, while ignoring the last two data points with  $d_{PdNi} = 95$  and 100 nm.

$I_c$  vs  $H_{ext}$  measurements as described in sections 4.2.2 and 4.2.3 were performed on several samples for which the PdNi thickness was varied from 35 to 100 nm.

The maximum critical current density ( $J_c$ ) obtained for all such devices in virgin as well as magnetized samples is plotted as a function of PdNi thickness ( $d_{PdNi}$ ) in Fig. 4.9. Each data point represents the average over multiple Josephson junctions measured on the same substrate. The error bars are the standard deviation of the measurements. The critical current density is seen to decrease exponentially over five orders of magnitude over the measured range of thickness. To our knowledge this was the widest range of ferromagnet thickness in S/F/S Josephson junctions studied to this date.

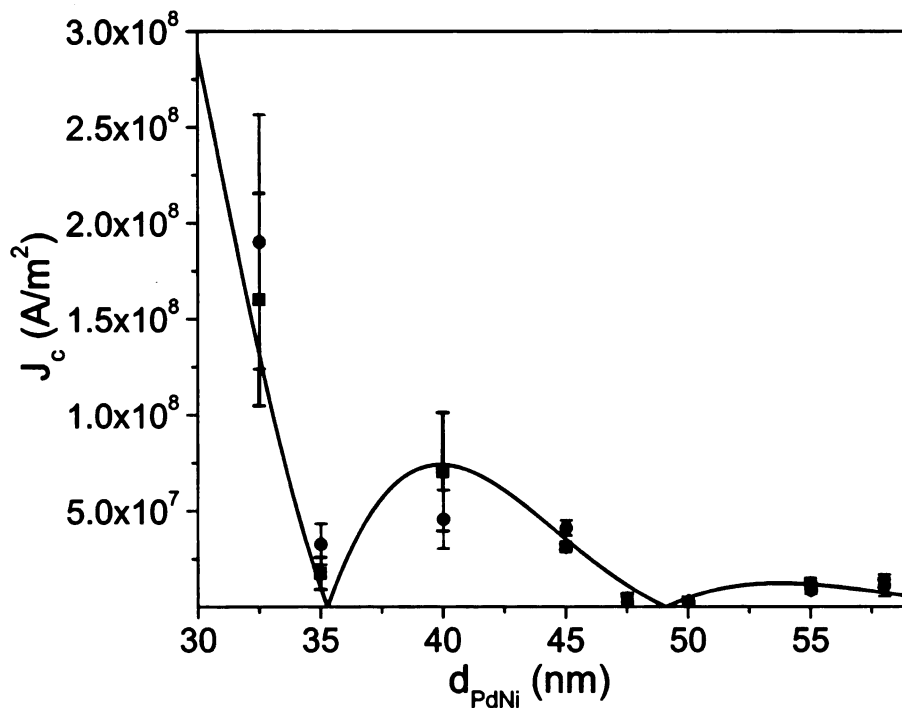


Figure 4.10: Linear plot of  $J_c$  vs.  $d_{PdNi}$  for the thickness range 32.5 to 58 nm. The line is the same fit shown in Fig. 4.9.

It is important to notice here that the critical current density,  $J_c$  does not decrease monotonically but in fact shows the oscillations that are characteristics of  $0 - \pi$  junctions. Fig. 4.10 and Fig. 4.11 show linear plots of  $J_c$  vs  $d_{PdNi}$  for the thickness ranges 32.5-58 nm and 55-85 nm respectively. The local minima are clearly seen

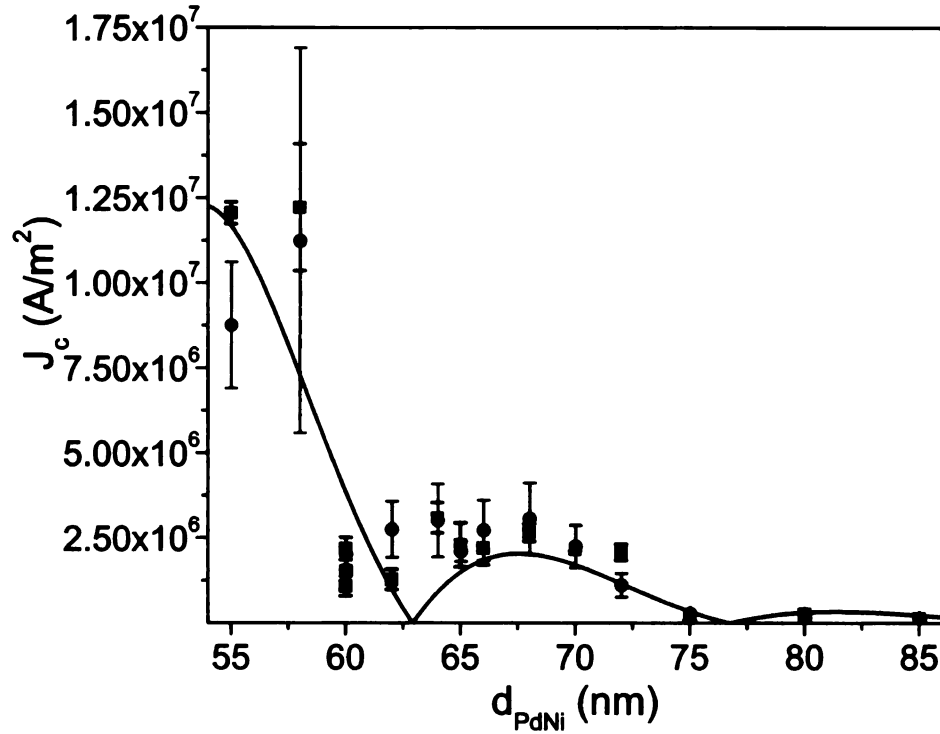


Figure 4.11: Linear plot of  $J_c$  vs.  $d_{PdNi}$  for the thickness range 55 to 85 nm. The line is the same fit shown in Fig. 4.9.

in these figures in the neighborhood of 35, 48, 60, and 75 nm. Such an oscillatory behavior representative of  $0 - \pi$  transition has been observed previously by various groups [26, 27, 23, 22, 24, 73, 29, 30] working on CuNi, PdNi, Ni, Co, etc.

#### 4.2.5 Resistivity of PdNi

Figure 4.12 shows a plot of specific resistance  $AR_N$  vs.  $d_{PdNi}$ , where  $R_N$  is the normal state resistance of our Josephson junction. The specific resistance  $AR_N$  has barrier and bulk contributions which can be written in the following form,

$$AR_N = 2AR_B + \rho_{PdNi}d_F \quad (4.4)$$

where  $R_B$  is the PdNi/Nb boundary resistance,  $\rho_{PdNi}$  is the resistivity of PdNi, and  $d_F$  is the thickness of the PdNi layer. A linear fit of the data to Eqn. 4.4 yields

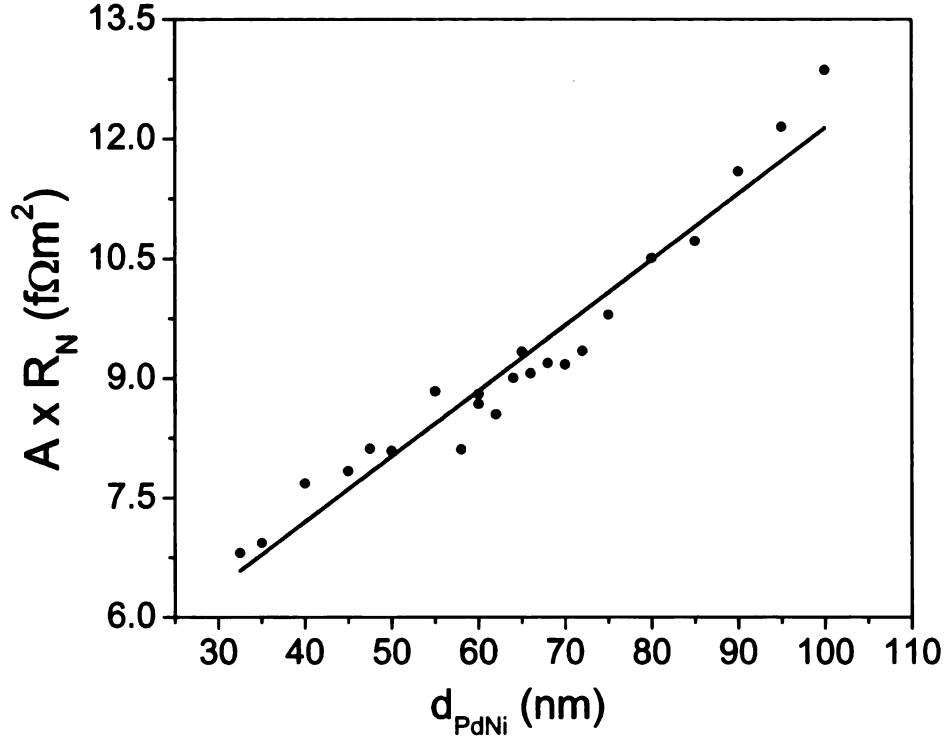


Figure 4.12: Area times normal-state resistance vs.  $d_{PdNi}$  for all of our Josephson junction samples. The slope provides the resistivity of PdNi and the y-intercept provides twice the Nb/PdNi boundary resistance

the boundary resistance of  $AR_B = 2.31 \pm 0.07 f\Omega m^2$  and the resistivity of PdNi  $\rho_{PdNi} = 68 \pm 3 n\Omega m$ . Independent in-plane Van der Pauw measurements performed on 200 nm thick PdNi film yielded a resistivity value of  $\rho_{PdNi} = 116 \pm 2 n\Omega m$ . It is possible that the in-plane resistivity could be higher than the perpendicular resistivity due to columnar growth of PdNi; although measurements on other sputtered metals often find a close agreement between these two methods of measurement.

### 4.3 Theoretical Analysis of PdNi Josephson Junctions

The three energy scales of importance in understanding S/F/S results are,  $E_{ex}$ , the exchange energy in the ferromagnet;  $\Delta$ , the superconducting gap;  $\hbar/\tau$ , where  $\tau$  is the mean time between collisions of an electron propagating in the ferromagnet. The relative magnitude of the energies determine the 3 distinct regimes. For all the known ferromagnetic materials used in S/F/S studies to this date,  $E_{ex} \gg \Delta$ . However, depending on the magnitude of  $\hbar/\tau$  relative to these two energies, the system could either be in,

1. Clean limit where  $E_{ex}\tau \gg \hbar$  and  $\Delta\tau \gg \hbar$
2. Intermediate limit where  $E_{ex}\tau > \hbar$  and  $\Delta\tau < \hbar$
3. Dirty limit where  $E_{ex}\tau \ll \hbar$  and  $\Delta\tau \ll \hbar$ .

These three regimes can also be characterized by comparing the relative length scales: the mean free path  $l_e = v_F\tau$ , the superconducting coherence length  $\xi_S = \hbar D_s/\Delta$ , clean (dirty)limit exchange length,  $\xi_F = \hbar v_F/2E_{ex}$  ( $\xi_F = \sqrt{\hbar D_F/E_{ex}}$ ).

In the dirty limit, when  $d_F$  is of an order of  $\xi_F$  or greater, the superconducting correlations decay and oscillate on a length scale given by the dirty-limit exchange length  $\xi_F^* = \sqrt{\hbar D_F/E_{ex}}$ . In this case, the thickness  $d_F$  dependence of superconducting critical current  $J_C$  is given Buzdin *et al.* [74] and is of the form,

$$I_c(d_F) = I_{co} \exp\left(\frac{-d_F}{\xi_F^*}\right) \left| \sin\left(\frac{d_F}{\xi_F^*} + \frac{\pi}{4}\right) \right| \quad (4.5)$$

In the presence of spin-flip and spin-orbit scattering, the length scale of oscillation is not equal to the length scale of decay [14, 62, 63, 33]. The general equation in that case is given by,

$$I_c(d_F) = I_{co} \exp\left(\frac{-d_f}{\xi_{F1}}\right) \left| \sin\left(\frac{d_F}{\xi_{F2}} + \phi\right) \right| \quad (4.6)$$

In general, the effect of spin-flip and spin-orbit scattering is to increase the length scale of oscillation ( $\xi_{F2}$ ) relative to the length scale of decay ( $\xi_{F1}$ ). In the past, an equation similar to this was used to fit  $I_c$  vs  $d_F$  data from S/F/S junctions containing CuNi alloy, with  $\xi_{F1} = 1.3$  nm and  $\xi_{F2} = 3.5$  nm. The smaller value of  $\xi_{F1}$  compared to  $\xi_{F2}$  indicated that the spin-flip scattering is strong. We too used the above equation as a fit to our data, and the fit is as shown in Fig. 4.9. But surprisingly we found that the length scale of oscillation ( $\xi_{F2} = 4.4 \pm 0.1$  nm) was smaller than the length scale of decay ( $\xi_{F1} = 7.7 \pm 0.5$  nm). Thus the dirty limit assumption that led us to using this equation is not valid in our case. After digging further into the experiments done in the past, we noticed the condition  $\xi_{F1} > \xi_{F2}$  has been observed in S/F/S junctions using strong ferromagnets like Ni, Fe, Co, and Ni<sub>80</sub>Fe<sub>20</sub> [27, 28]. These materials have large exchange energy and they satisfy the intermediate limit condition,  $E_{ex}\tau > \hbar$  and  $\Delta\tau < \hbar$ . Our observation of  $\xi_{F1} > \xi_{F2}$  in our S/F/S junctions using PdNi alloy suggests that PdNi may also be in the intermediate limit.

Bergeret *et al.* [8] provides a general formula for the critical current behavior in both the dirty limit as well as in the intermediate limit. When  $d_F > l_e$ , ( $l_e$  is the mean free path) the formula for the intermediate limit is given by,

$$I_c(d_F) \propto \pi T \sum_{\omega > 0} \frac{\Delta^2}{\Delta^2 + \omega^2} \frac{\sin(d_F/\xi_F)}{d_F/\xi_F} \exp\left(\frac{-d_F}{l_e}(1 + 2\omega\tau)\right) \quad (4.7)$$

where the summation is done over the positive Matsubara frequencies,  $\omega = \pi k_B T (2m + 1)$  with T as the temperature. Asymptotically at large values of  $d_F$ , Eqn. 4.7 is similar to Eqn. 4.6. The fit parameters obtained using Eqn. 4.7 are,  $\xi_F = 4.01 \pm 0.1$  nm and  $l_e = 10.6 \pm 1$  nm. Although  $\xi_F$  is comparable to  $\xi_{F2}$ ,  $l_e$  is somewhat larger than the  $\xi_{F1}$  obtained from the fit using Eqn. 4.6. The mismatch is due to the sum

over Matsubara frequencies in Eqn. 4.7. In an another theoretical approach taken by Kashuba *et al.* [75], the authors solve for the case of intermediate limit taking into account the spin-flip and spin-dependent scattering in F layer. The result thus obtained is nearly identical to Eqn. 4.7 stated above.

## 4.4 Discussion of Results

### 4.4.1 Estimate of Mean Free Path in PdNi

For many metals the product  $\rho l_e$ , which is inversely proportional to the Fermi surface area, is known and tabulated [76]. It is therefore straightforward to estimate the mean free path in metals from the measured resistivity. In the past people working on PdNi have tried to estimate its mean free path using the  $\rho l_e$  value in Pd. The reported values [66, 65, 70] vary widely in the range  $0.33 - 4.0 f\Omega m^2$ . The difficulties in getting a right estimate for  $\rho l_e$  value lies in the complex band structure of Pd. The detailed discussion of Fermi surface in Pd has been given in several papers [77, 78, 79, 80]. Pinski *et al.* [77] states that at 10 K, 97% of the transport current is carried by light electrons on  $\Gamma$ -centered sheet of the Fermi surface, whereas specific heat is dominated by heavier holes on the open portion of the Fermi surface. The lower estimate  $0.33 f\Omega m^2$  [66, 65] is a result of using Einstein's relation,  $\sigma = n(E_F)e^2 D$ , with density of states at Fermi level  $n(E_F)$  obtained from specific heat coefficient  $\gamma = (\pi^2/3)k_B^2 n(E_F)$ .

We estimate the  $\rho l_e$  product for PdNi in two ways. Since the electronic transport in Pd is dominated by the electrons on the  $\Gamma$ -centered sheet, we use the total number of carriers  $n$ , the density of states at the Fermi level  $n(E_F)$ , the effective mass  $m^*$ , and the Fermi velocity  $v_F$  on that sheet. These values have all been tabulated by Dye *et al.*[79] based on deHaas van-Alphen measurements of the Fermi surface of Pd. Using  $n = 0.375$  carriers/atom =  $2.54 \cdot 10^{28} m^{-3}$ ;  $n(E_F) = 0.189$  states/(eV atom

spin) =  $2.56 \cdot 10^{28} eV^{-1} m^{-3}$ ;  $m^* = 2.0m_e$ ;  $v_F = 0.6 \cdot (2\pi/a) \cdot (\hbar/2m) = 5.6 \cdot 10^5$  m/s and using the Drude formula,  $\sigma = ne^2\tau/m^*$ , we find  $\rho l_e = 1.55 f\Omega m^2$ , while using the Einstein relation we find  $\rho l_e = 1.31 f\Omega m^2$ . The slight difference between the two values is likely due to the non-parabolic character of the  $\Gamma$ -centered sheet. We also estimate  $\rho l_e$  product using a second method, where we use our own measured resistivity,  $\rho = 68 n\Omega m$  and the mean free path from the  $J_c$  vs.  $d_F$  fit,  $l_e = 11.2$  nm and obtain  $\rho l_e = 0.76 f\Omega m^2$ . Thus both our methods yield  $\rho l_e$  values that are comparable.

In his Ph.D. thesis [70], Kontos found that the resistivity of thin PdNi films with  $x \approx 12\%$  varied linearly with inverse thickness  $1/d$  once the films were thinner than about 8 nm, indicating that the mean free path is limited by the film thickness. The slope of the graph gives the product  $\rho d = 1.7 f\Omega m^2$  which is not very different from the estimates we have obtained from above.

#### 4.4.2 Estimate of Exchange Energy in PdNi

As shown earlier, the fit to our  $J_c$  vs.  $d_F$  indicated a longer length scale governing the exponential decay compared to the length scale governing the oscillation ( $\xi_{F1} > \xi_{F2}$ ). This suggested that our PdNi was in intermediate limit. Using  $\xi_{F2} = 4.0 \pm 0.1$  nm and the Fermi velocity of the dominant carriers,  $v_F = 5.6 \cdot 10^5$  m/s [79], gives an estimate for the exchange energy in our Pd<sub>88</sub>Ni<sub>12</sub> alloy of  $E_{ex} = \hbar v_F / 2\xi_{F2} = 44$  meV.

#### 4.4.3 Comparison to Other Experiments

It is important to mention here that a similar experiment was performed by Kontos *et al.* [23] using a PdNi alloy of similar concentration to ours. They studied S/I/F/S Josephson junctions with a PdNi alloy and found the length scale governing the decay,

$\xi_{F1}$ , was similar to the length scale governing the oscillation,  $\xi_{F2} \approx \xi_{F1} = 2.8$  nm. The values of  $\xi_{F2}$  in their experiment and ours are rather close to each other, but the values of  $\xi_{F1}$  are not. It is not clear if that discrepancy is significant or not. The thickness range covered in the earlier work was 4.5 - 14 nm, whereas the range we covered was 32.5 - 100 nm. If the mean free path in the PdNi alloy is indeed in the range of 11 nm, then the samples studied by Kontos *et al.* [23] were in the crossover regime with  $d_F \approx l_e$ , where the thickness dependence has not yet obtained the asymptotic exponential decay,  $J_c \propto \exp(-d_F/l_e)$ . But then one would expect a less steep decay of  $J_c$  with  $d_F$ , rather than a more steep decay. We believe that this could be because the PdNi films deposited in different laboratories may have different polycrystalline structures, and hence very different mean free paths. A summary of the parameters estimated by previous workers, as well as by our work, is given in Table 4.1 and 4.2.

Source	Experiment	Ni conc. (at. %)	$v_F$ ( $10^5$ m/s)	$\rho l_e$ ( $\text{f}\Omega\text{m}^2$ )	$\rho$ ( $\text{n}\Omega\text{m}$ )	$l_e$ (nm)
[31]	S/F DOS	10	2.0	4	-	$\approx d_F$
[23]	S/I/F/S	12	2.0	4	-	$\approx d_F$
[66]	$T_c$ of S/F	14	2.0	4	240	16.6
[67, 68]	$T_c$ of S/F	14	2.0	0.96	240	4
[65]	$T_c$ of S/F	15	2.0	0.3256	220	1.48
[64]	S/F/S	18	2.0	-	-	-
this work	S/F/S	12	5.6	0.76	68	11

Table 4.1: Summary of PdNi parameters,  $v_F$ ,  $\rho l_e$ ,  $\rho$  and  $l_e$  from several groups. The superconductor used in all the above experiments was Niobium.

#### 4.4.4 $0 - \pi$ Josephson Junction: Temperature Dependence

Throughout the course of this work, our aim was to search for signs of spin-triplet superconducting correlations in our samples. At first glance, the data in Fig. 4.9 show no sign of spin-triplet superconducting correlations, which if present, might manifest

Source	$\xi_{F1}$ (nm)	$\xi_{F2}$ (nm)	$E_{ex}$ (meV)	formula to extract $E_{ex}$	$T_{Curie}$ (K)
[31]	2.8	2.8	35	$(\hbar D/E_{ex})^{1/2}$	100
[23]	3.5	3.5	13	$(\hbar D/E_{ex})^{1/2}$	260
[66]	6	6	15	$(\hbar D/E_{ex})^{1/2}$	156
[67, 68]	3.4	3.4	13	$(\hbar D/E_{ex})^{1/2}$	185
[65]	3.5	3.5	13	$(\hbar D/E_{ex})^{1/2}$	260
[64]	2.4	2.4	52	$(\hbar D/E_{ex})^{1/2}$	200
this work	8.0	4.0	44	$\hbar v_F/E_{ex}$	175

Table 4.2: Summary of PdNi parameters from several groups. Note that the most workers have used the diffusive formula  $\xi_{F2} = (\hbar D/E_{ex})^{1/2}$  to extract  $E_{ex}$  from the measured value of  $\xi_{F2}$ , whereas we have used the ballistic formula,  $\xi_{F2} = \hbar v_F/2E_{ex}$ .

themselves as a crossover to a less-steep and non-oscillatory exponential decay of  $J_c$  at large values of  $d_F$ .

However, it is intriguing to find that the length scale characterizing the exponential decay of  $J_c$  in our samples,  $\xi_{F1} = 8-11$  nm, is substantially longer than that observed previously in S/I/F/S junctions with PdNi [23]. The natural question to ask ourselves was - Could it be that we are already observing the triplet Josephson effect throughout the whole range of  $d_F$  reported here? The strongest evidence against spin-triplet correlations in our Josephson junctions is the nearly-periodic set of local minima we observe in  $J_c$  vs.  $d_F$ , shown in Fig. 4.10 and Fig. 4.11. We believe that those local minima signal crossovers between 0-junctions and  $\pi$ -junctions, which are due to the effect of the exchange splitting on spin-singlet superconducting correlations. A Josephson supercurrent dominated by spin-triplet correlations would not exhibit such minima, but rather would decay monotonically with increasing  $d_F$ . However looking at the uncertainty in our data points, the next natural question to ask was whether the local minima we observe truly represent 0 -  $\pi$  crossovers than just an unlucky distribution of sample-to-sample fluctuations?

We realized that there are three ways to probe the local minima observed in our  $J_c$  vs.  $d_F$  data:

1. By a direct measurement of the current-phase relationship of the junction [81].
2. By extension of  $J_c$  vs.  $d_F$  measurements to smaller values of  $d_F$ , to see if the slope of the  $J_c$  vs.  $d_F$  semi-log plot changes to a value close to that measured by Kontos *et al.* This would require reducing the lateral size  $w$  of our junctions, so as to maintain the condition  $\lambda_J > w/4$ .
3. By measuring  $J_c$  vs. temperature  $T$  for samples very close to a  $0 - \pi$  crossover. In S/F/S junctions with very weak ferromagnets, the  $0 - \pi$  crossover has been observed in the  $T$ -dependence of  $J_c$  [21, 26, 24, 30]. As the exchange energy increases, however, the thickness range over which one can see a non-monotonic  $T$ -dependence of  $J_c$  gets progressively narrower [30].

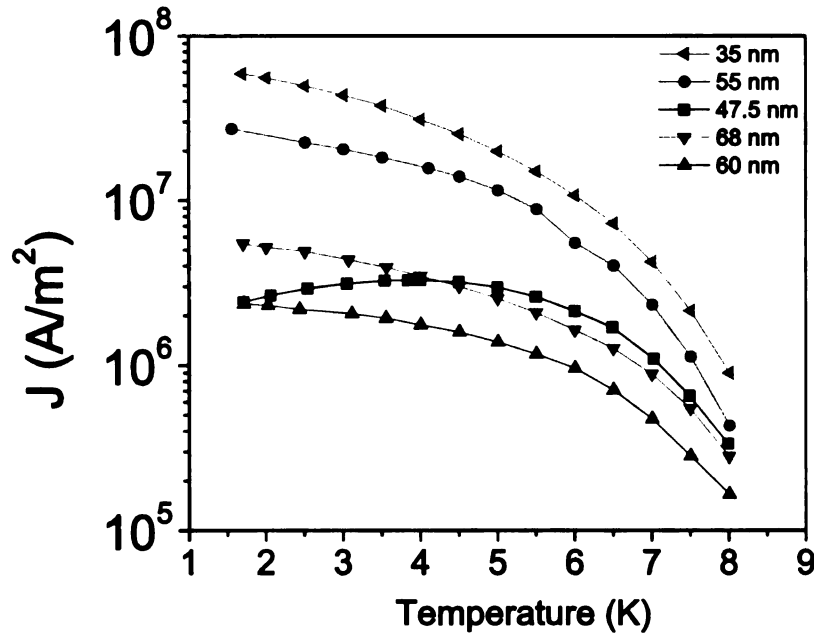


Figure 4.13: *Critical current density vs. temperature for five Nb/PdNi/Nb Josephson junctions with  $d_{PdNi}$  as listed in the figure. The anomalous temperature dependence for the sample with  $d_{PdNi} = 47.5$  nm indicates that its thickness is very close to a  $0-\pi$  transition.*

Each of these checks presents its own set of challenges. But when posed with several different possibilities, we decided to use the tool at our disposal—Prof. Pratt’s

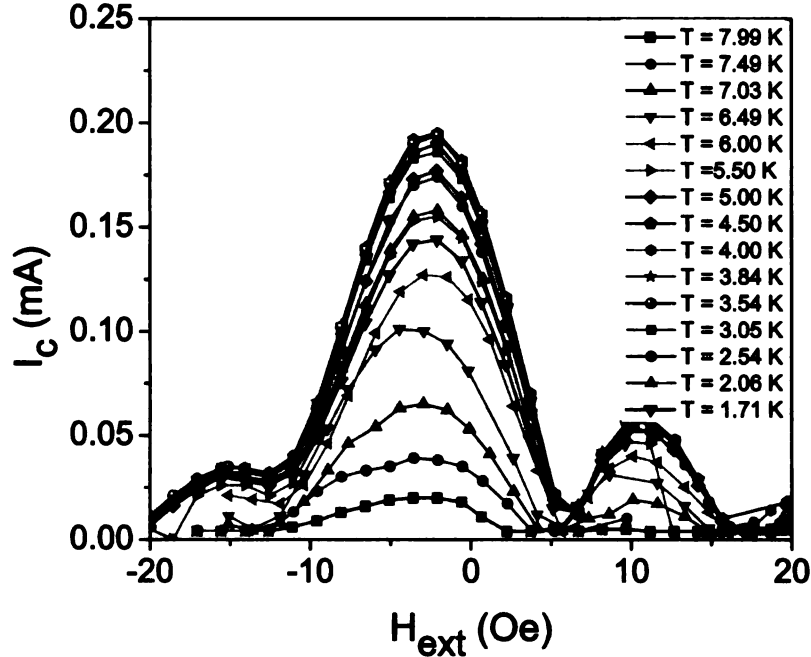


Figure 4.14: Raw data showing  $I_c$  vs.  $H$  for ferromagnetic Josephson junction with 47.5 nm thick PdNi layer. The largest critical current is seen at  $\sim 4$  K

home-built Quick-Dipper probe-III. This probe allows us to vary the temperature in the range from 1.6 to 8.0 K. The details of this experimental setup are given in Chapter 3. Section 3.5.4. We were therefore quickly able to measure  $J_c$  vs. temperature  $T$  for some of our Josephson junctions. Fig. 4.13 shows the temperature dependence of critical current for Nb/PdNi/Nb Josephson junctions with  $d_{PdNi} = 35, 55, 68, 47.5, 60$  nm. (Fig. 4.14 shows  $I_c$  vs  $H$  measured at different temperatures for a Nb/PdNi/Nb Josephson junction with 47.5 nm thick PdNi layer.) A clear non-monotonic behavior is seen for the 47.5 nm sample which was close to a  $0 - \pi$  transition. Whereas, no such behavior was seen for the 35 nm and 60 nm samples, in spite of their closeness to our anticipated  $0 - \pi$  crossover. A non-monotonic temperature dependence of the critical current observed for the 47.5 nm sample confirms  $0 - \pi$  oscillations that are characteristic of the standard singlet proximity effect in PdNi. In the past, similar non-monotonic dependence indicative of  $0 - \pi$  transition was observed by various groups[21, 26, 24] working with CuNi alloy. This led us to believe that the local

minima seen in our data (Fig. 4.9) do indeed represent  $0 - \pi$  crossovers, rather than sample-to-sample fluctuations.

## 4.5 No Sign of LRTC!

As is evident from Fig. 4.9, the critical current density in our Nb/PdNi/Nb oscillates and decays over a characteristic length scale of  $\sim 10$  nm. There is no sign of a crossover to a slower non-oscillatory decay of the type shown in Chapter 2, Fig. 2.12. Our data are therefore consistent with singlet proximity effect. There is no indication of LRTC.

The most natural question to ask here is: Why don't we see long range triplet correlations? As mentioned earlier, the weak ferromagnetic systems suffer from strong spin-flip and/or spin-orbit scattering, which could be detrimental to the observation of long range triplet correlations. To investigate the spin diffusion length ( $l_{sf}$ ) in PdNi alloy, a separate experiment was carried out using the techniques borrowed from the GMR (Giant Magnetoresistance) community. The details of this experiment are given in Chapter 5. The measured value of the spin diffusion length,  $l_{sf} = 2.8$  nm, was shorter than the length scale characterizing the decay of the Josephson supercurrent in the present work ( $\xi_{F1} \approx l_e \approx 11.7$  nm). This was surprising, since normally, one assumes that spin-flip and spin-orbit scattering processes occur on length scales much longer than the mean free path. This assumption is also the basis of the diffusive model used in discussing the spin diffusion length in Valery-Fert theory [82]. When we were dealing with this puzzling issue, we also discovered an out-of-plane anisotropy in our PdNi films. Nevertheless, we now believe that the short value of  $l_{sf}$  as well as the out-of-plane anisotropy in our PdNi films is a result of strong spin-orbit scattering in this alloy. A detailed exposition of this conclusion is given in Chapter 5. And the said discrepancy in the relative magnitude of  $l_e$  and  $l_{sf}$ , ( $l_e > l_{sf}$ ), is perhaps due to

the magnetically inhomogeneous nature of PdNi, which destroys the spin memory by rotating the spin on a length scale much smaller than the mean-free path,  $l_e$ . This possibly points to PdNi as a ferromagnetic material with the much needed magnetic inhomogeneities that are essential for generating LRTC, but which unfortunately is rendered useless because of the short spin-diffusion length. The scientific irony here is that the origin of this short spin-diffusion may perhaps lie in these inherent magnetic inhomogeneities!

Apart from having a long spin-diffusion length, it is equally important that the length scale characterizing the magnetic inhomogeneity (say  $\delta_m$ ) in PdNi should be comparable to the Cooper pair coherence length  $\xi_s$  in Nb. If  $\delta_m \ll \xi_s$ , then a Cooper pair will experience the magnetization averaged over the length  $\xi_s$ , and triplet correlations will not be produced efficiently. If  $\delta_m \gg \xi_s$ , then a typical Cooper pair experiences no magnetic inhomogeneity. Unfortunately at this point, the typical domain sizes and domain wall widths in our PdNi alloy are not known. Since the Curie temperature of PdNi is well below room temperature, obtaining information about magnetic structure requires a low temperature magnetic visualization technique, such as low-temperature magnetic force microscopy (MFM) or Bitter decoration. And even then, the former method is not well-suited to weak ferromagnets, because the magnetization of the MFM tip may influence the domain structure of the sample. Unfortunately, no such measurements have been performed on PdNi alloy, to our knowledge.

## 4.6 Conclusion

Here we have measured the critical current of Nb/PdNi/Nb Josephson junctions and have seen it drop by five orders of magnitude over a thickness range from 32 to 100 nm. We have also seen and confirmed that the periodic array of local minima, are in

fact  $0 - \pi$  oscillations that are characteristic of the standard singlet proximity effect in PdNi. We have discussed possible reasons for the absence of induced spin-triplet correlations, such as spin-flip scattering or a poor match of length scales between the magnetic domains and the superconducting coherence length. Although this experiment did not lead us to our most coveted goal of observing long spin-triplet correlations, it definitely helped us in understanding the obstacles in reaching towards it.

# Chapter 5

## GMR Experiments

### 5.1 Magnetoresistance (MR)

The term magnetoresistance (MR) refers to the change in resistance of a material when a magnetic field is applied. The MR ratio is defined as the ratio of the change in resistance in when the field is applied, to the resistance at zero field.

$$\text{MR-ratio} = \frac{R_H - R_0}{R_0} = \frac{\Delta R}{R} \quad (5.1)$$

The materials which have large resistance in the presence of field than in the absence of field are said to have positive MR, whereas, if the field reduces resistivity, the materials are said to have negative MR.

### 5.2 GMR Theory

*Giant magnetoresistance* (GMR) is seen in the so called magnetic multilayers, where layers of magnetic and non-magnetic materials are stacked on each other. It was discovered almost simultaneously in 1988 on Fe/Cr multilayers by Albert Fert [83] and on Fe/Cr/Fe trilayers by Peter Grunberg [84]. Depending on the thickness of

the non-magnetic layer, the magnetic layers either couple ferromagnetically or antiferromagnetically. Fig. 5.1a. shows the case where the magnetic layers are antiferromagnetically coupled. That is, in the absence of the magnetic field the magnetization of the ferromagnetic layers is antiparallel. The change in the resistance of the multilayer arises when the applied field aligns the magnetic moments of the successive ferromagnetic layers. This is shown in Fig. 5.1b.

### 5.2.1 Simplified GMR Model

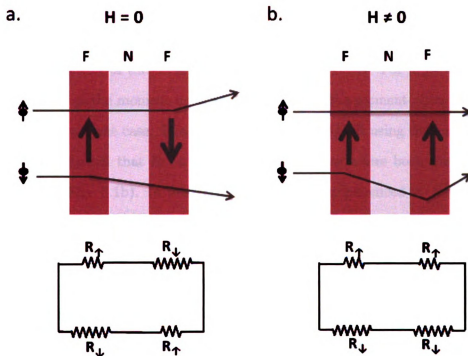


Figure 5.1: A cartoon representing GMR effect. A circuit diagram is shown at the bottom of each cartoon, where the magnetic layers are represented by resistances. If the electron moment is parallel to the direction of magnetization in the F-layer, the resistance experienced by it is given by  $R_{\uparrow}$ . Similarly, if the electron moment is antiparallel to the direction of magnetization of the F-layer, the resistance experienced by it is given by  $R_{\downarrow}$ .

As said before, GMR device consists of ferromagnetic (F) layers separated by non-magnetic (N) layers. The resistance of such a device can be explained by using Fert's simplified picture. In absence of magnetic field, the magnetization of two F-layers is such that they have the net magnetization pointing in opposite directions. Whereas, when the field is applied, the magnetization in two F layers becomes parallel to each other. This is shown in Fig. 5.1a. An electric current sent through the system is composed of two type- majority and minority spin current, without being very specific we can also refer to them as moment-up and moment-down current. In ferromagnets, the moment-up and moment-down particles have different densities of states at the Fermi level. This causes the moment-up electrons to scatter differently than the moment-down electrons both in the F-layer as well as at the F/N interface. Because of this spin dependent scattering, the resistivity of one channel of electrons is less than the resistivity of the other spin channel in the F-layer. For most ferromagnets, the resistivity of the moment-up channel is less than the moment-down channel, but this is not always the case. The Fig. 5.1 explains the GMR using the circuit diagram with an assumption that  $R_{\uparrow} \ll R_{\downarrow}$ . Consider the case where both the F-layers are parallel (See Fig. 5.1b). In this case, the resistance experienced by the moment-up electrons in first F-layer is  $R_{\uparrow}$  the same as the resistance in second F-layer, so that the total resistance experienced by moment-up electrons is  $2R_{\uparrow}$ . Similarly the resistance experienced by moment-down electrons as it traverse two ferromagnetic layers is  $2R_{\downarrow}$ . Standard addition of resistances for a parallel (P) magnetic configuration gives the total resistance for  $R_P$ ,

$$R_P = 2 \frac{R_{\uparrow} R_{\downarrow}}{(R_{\uparrow} + R_{\downarrow})} \quad (5.2)$$

Now consider the case where the magnetization in F-layers is antiparallel as shown in Fig. 5.1a. In this case the resistance experienced by moment-up electrons in

the first and second F-layers is  $R_{\uparrow}$  and  $R_{\downarrow}$  respectively, so that the total resistance experienced by the moment-up electrons as they traverse the two F-layers will be  $R_{\uparrow} + R_{\downarrow}$ . The moment-down electrons will be affected in the same but opposite way and its resistance will be  $R_{\downarrow} + R_{\uparrow}$ . The total resistance in antiparallel magnetic configuration will be  $R_{AP}$ ,

$$R_{AP} = \frac{1}{2}(R_{\uparrow} + R_{\downarrow}) \quad (5.3)$$

The difference between the two cases gives the Giant Magnetoresistance (GMR),

$$\Delta R = R_P - R_{AP} = -\frac{1}{2} \frac{(R_{\uparrow} - R_{\downarrow})^2}{(R_{\uparrow} + R_{\downarrow})} \quad (5.4)$$

The larger the scattering asymmetry for two spin channels, the larger is the difference between  $R_{\uparrow}$  and  $R_{\downarrow}$  and the larger is the magnetoresistance.

In the N layer, both the moment-up and moment-down electrons experience the same resistance and it is generally much less than the resistance in F layers and the F/N interfaces and can therefore be neglected.

### 5.2.2 Two-Current Series-Resistor Model (2CSR)

The models used for the analysis of CPP-GMR (Current perpendicular to plane-Giant magnetoresistance) data depend on the relative size of spin diffusion length,  $l_{sf}$  and the layer thickness,  $t$ . When  $l_{sf} \gg t$ , the model used for analysis is called the two current series resistor model (2CSR model) [85, 82, 86]. The extension of the model was developed by Valet and Fert [82] for  $l_{sf} \simeq t$ . The details of the Valet-Fert theory can be found in the theses written by past students [59].

The 2CSR model that we will discuss here is an extension of the simplified Fert model described in the previous section. In this model, one divides the current sent through the system into two independent moment-up and moment-down channels.

Each bulk and interface resistance can be thought of as an independent resistor. The total resistance experienced by each spin channel is therefore a series contribution of these resistors. The origin of GMR lies in the fact that the moment-down channel experiences different resistance (in bulk or at interface) than the moment-up channel. This is what gives rise to bulk scattering asymmetry or interface scattering asymmetry. To calculate the total resistance experienced by the current flowing through the multilayer, one then combines the overall channel resistances in parallel. The difference in resistance experienced by the current for parallel (P) and antiparallel (AP) magnetic configuration of the magnetic multilayers is called *Magnetoresistance* (MR),  $MR=R_{AP} - R_P$ .

Before going into the details of 2CSR model, we define several parameters used to make calculations and model the multilayer.

The resistivity of the majority and minority channels is given by  $\rho_F^\uparrow$  and  $\rho_F^\downarrow$  respectively. A useful parameter  $\rho_F^*$  is defined as,

$$\rho_F^* = \frac{\rho_F^\uparrow + \rho_F^\downarrow}{4} \quad (5.5)$$

$\rho_F^*$  is a measure of the average resistivity for moment-up and moment-down electrons. In addition, the bulk spin-scattering asymmetry is defined by the parameter  $\beta$  as follows,

$$\beta = \frac{\rho_F^\downarrow - \rho_F^\uparrow}{\rho_F^\downarrow + \rho_F^\uparrow} \quad (5.6)$$

The resistivity experienced by moment-up and moment-down channels can be written in terms of a bulk spin-scattering asymmetry parameter  $\beta$  and  $\rho^*$  using the following

equations,

$$\rho_F^\uparrow = 2\rho_F^*(1 - \beta) \quad (5.7)$$

$$\rho_F^\downarrow = 2\rho_F^*(1 + \beta) \quad (5.8)$$

One can therefore also write,

$$\rho_F^* = \frac{\rho_F}{(1 - \beta^2)} \quad (5.9)$$

where,  $\rho_F = (1/\rho_F^\uparrow + 1/\rho_F^\downarrow)^{-1}$  is the usual resistivity.

Similarly, the spin-scattering asymmetry at an interface is given by the parameter  $\gamma$ . The specific resistance of moment-up and moment-down channels, given by  $AR^\uparrow$  and  $AR^\downarrow$  can be written in terms of the spin-scattering asymmetry at interface as follows,

$$AR_{F/N}^\uparrow = 2AR_{F/N}^*(1 - \gamma) \quad (5.10)$$

$$AR_{F/N}^\downarrow = 2AR_{F/N}^*(1 + \gamma) \quad (5.11)$$

Consider the simplest case of an F/N/F spin valve. Let  $t_N$  and  $t_F$  represent the thickness of the individual N and F layers respectively. Now, if one considers the case where two ferromagnetic layers have antiparallel configuration, the specific resistivity for the moment-up channel is given by,

$$AR_{AP}^\uparrow = \rho_F^\uparrow t_F + AR_{F/N}^\uparrow + \rho_N^\uparrow t_N + AR_{F/N}^\downarrow + \rho_F^\downarrow t_F \quad (5.12)$$

Similarly, the specific resistance for the down channel is given by,

$$AR_{AP}^\downarrow = \rho_F^\downarrow t_F + AR_{F/N}^\downarrow + \rho_N^\downarrow t_N + AR_{F/N}^\uparrow + \rho_F^\uparrow t_F \quad (5.13)$$

The total specific resistance of the anti-parallel state is,

$$\frac{1}{AR_{AP}} = \frac{1}{AR_{AP}^{\uparrow}} + \frac{1}{AR_{AP}^{\downarrow}} \quad (5.14)$$

In the non-magnetic metals, both the moment-up and moment-down electrons experience the same resistance and hence the bulk spin scattering asymmetry in normal metal  $\beta = 0$  or in other words,  $\rho_N^{\uparrow} = \rho_N^{\downarrow} = 2\rho_N$

Substituting  $AR_{AP}^{\uparrow}$  and  $AR_{AP}^{\downarrow}$  from Eqn.5.12 and 5.13 and using  $\rho_N^{\uparrow} = \rho_N^{\downarrow} = 2\rho_N$ , one gets the following equation,

$$AR_{AP} = \frac{\rho_F^{\downarrow}t_F + AR_{F/N}^{\downarrow} + 2\rho_N t_N + AR_{F/N}^{\uparrow} + \rho_F^{\uparrow}t_F}{2} \quad (5.15)$$

Using Eqns. 5.7,5.8, 5.10 and 5.10, one can then write the specific resistivity for the anti-parallel case  $AR_{AP}$  in terms of  $\rho_F^*$ ,  $\gamma$ ,  $\beta$ , and  $AR_{F/N}^*$ .

$$AR_{AP} = 2\rho_F^*(1-\beta)t_F + 2AR_{F/N}^*(1-\gamma) + 2\rho_N t_N + 2AR_{F/N}^*(1+\gamma) + 2\rho_F^*(1+\beta) \quad (5.16)$$

Which after simplification gives,

$$AR_{AP} = 2\rho_F^*t_F + 2AR_{F/N}^* + \rho_N t_N \quad (5.17)$$

For the case where two ferromagnetic layers have parallel configuration,  $AR_P$  can be computed in the similar manner[85]. Finally,  $A\Delta R$  for a bilayer of F/N/F form is given by,

$$AR_{AP} - AR_P = \frac{[\beta\rho_F^*t_F + 2\gamma_{F/N}AR_{F/N}^*]^2}{AR_{AP}} \quad (5.18)$$

As explained earlier, this model holds true as long as,  $l_{sf} \gg t$ . When  $l_{sf} \approx t$ , one must then take into account the spin relaxation[82]. The 2CSR model in that case

needs to be modified, and for many cases only the numerical solution exists.

### 5.3 Spin Diffusion Length in PdNi Alloy

During the course of this project, some experiments were performed to measure the spin-diffusion length in certain ferromagnetic materials of interest to us. The experiments described here were not the primary goal of my project, and I will therefore focus my discussion only on the relevance of results obtained through them.

#### 5.3.1 Spin Valves: Py/Cu/PdNi

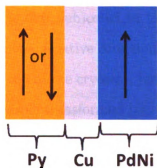


Figure 5.2: Schematic for PdNi spin valve. Because of the large coercive field of PdNi layer, it essentially acts like a pinned layer. The overall parallel (P) and antiparallel (AP) state is dominated by the low field switching action of Py layer.

Spin flip and spin orbit scattering in weak ferromagnetic alloys could be detrimental to long range triplet penetration, and hence a separate experiment to measure the spin diffusion length  $l_{sf}$  in PdNi was initiated in our group by a senior undergraduate student, Hamood Arham. Hybrid spin valves of the form Cu(10)/Py(24)/Cu(20)/PdNi( $d_{PdNi}$ )/Cu(10) were sputtered, where all the thicknesses are specified in nm. Because of the large coercive field of PdNi ( $H_c \approx 1.5$  kOe) compared to Py ( $H_c < 15$  Oe), PdNi essentially acts as a “pinned” layer, switching magnetic state only for large

applied fields. The overall magnetic state of the spin valve, parallel or antiparallel, is dominated by switching action of the “free” Py layer in small fields. Our spin valves are sandwiched between two superconducting electrodes, and measurements are performed at liquid He temperature (4.2 K) using superconducting quantum interference device (SQUID) electronics in a current comparator bridge. The details of the measurement set-up are given in Chapter 3, section 3.5.3.

The standard CPP-GMR (Current perpendicular to plane - Giant Magnetoresistance) measurements are performed, where current is passed perpendicular to the plane of the sample and the change in resistance is measured as a function of applied magnetic field. One such  $R(H)$  plot is shown in the Fig. 5.3. This figure shows the measurement performed at liquid helium temperature (4.2 K) on a spin valve with  $d_{PdNi} = 12$  nm. The sample is first subjected to large field,  $H = -5$  kOe so as to magnetize the PdNi layer in the negative direction. The field is then set to zero and the sample is pulled to the top of the cryostat, just above the liquid helium level until the NbTi wire near the sample transformed into the normal state. The sample is then lowered back into the liquid helium. This process removes any trapped flux from the Nb electrodes and the superconducting magnet. Our previous experience in magnetizing PdNi based Josephson junctions (See Chapter 4, section 4.2.3), has indicated no significant loss of  $M_{PdNi}$  in the warming up process. Once the sample was inside the cryostat the field was slowly scanned from  $H = -500$  Oe to  $H = 500$  Oe. Since the PdNi layer has large coercivity, the layer stays pinned in the negative direction when the field is slowly scanned, whereas Py which has a low coercivity switches it’s orientation relative to the PdNi layer from it’s initial parallel state to an antiparallel state. Since, the switching field of Py layer (5 Oe) is less than the field step size of 7.5 Oe, an abrupt increase in the resistance is seen very close to zero field when the Py layer switches. The field was then slowly scanned back from  $H = 500$  Oe to  $H = -500$  Oe. Figure 5.3 shows only the region between -100 to +100 Oe for

clarity. The reproducibility of data in two directions indicate that  $M_{PdNi}$  does not change significantly by applying fields as large as -500 Oe due to the large coercivity of the PdNi layer.

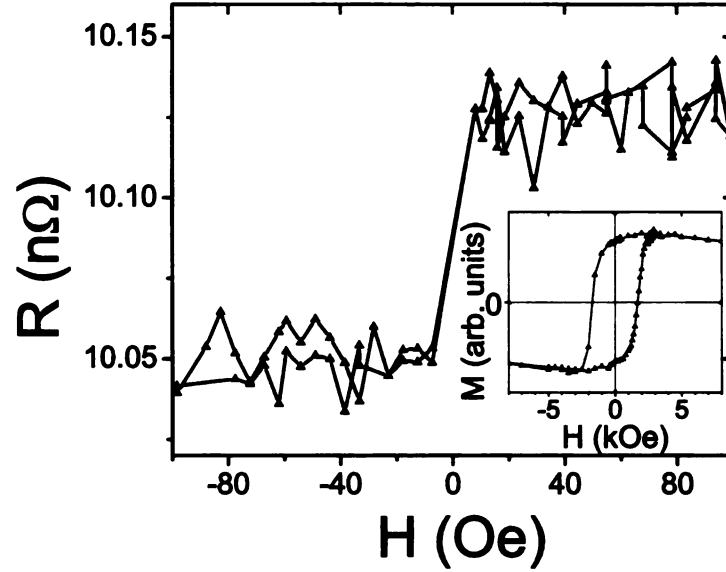


Figure 5.3:  $R$  vs.  $H$  data at 4.2 K for a Py/Cu/PdNi hybrid spin valve with  $d_{PdNi} = 12$  nm. Before starting experiment, PdNi layer is magnetized in the negative direction by applying a large field of -5 kOe. The increase in resistance is seen when the relative orientation of Py layer changes from parallel to antiparallel state. Because of the large coercivity of PdNi layer, it acts as a pinned layer. The inset shows the large coercive field of PdNi ( $H_c \approx 1.5$  kOe.)

Several such samples are measured with varying PdNi thickness and the specific magnetoresistance  $A\Delta R = A(R_{AP} - R_P)$  is plotted as a function of the PdNi thickness (See Fig. 5.4). When the thickness of the PdNi layer  $d_{PdNi}$  is much less than  $l_{sf}^{PdNi}$ , the two-current series-resistor model gives,

$$A\Delta R \propto \beta_{PdNi} \rho_{PdNi}^* d_{PdNi} + \gamma_{PdNi/Cu} A R_{PdNi/Cu}^* \quad (5.19)$$

When  $d_{PdNi} \gg l_{sf}^{PdNi}$ ,

$$A\Delta R \propto \beta_{PdNi} \rho_{PdNi}^* l_{sf}^{PdNi} + \gamma_{PdNi/Cu} A R_{PdNi/Cu}^* \quad (5.20)$$

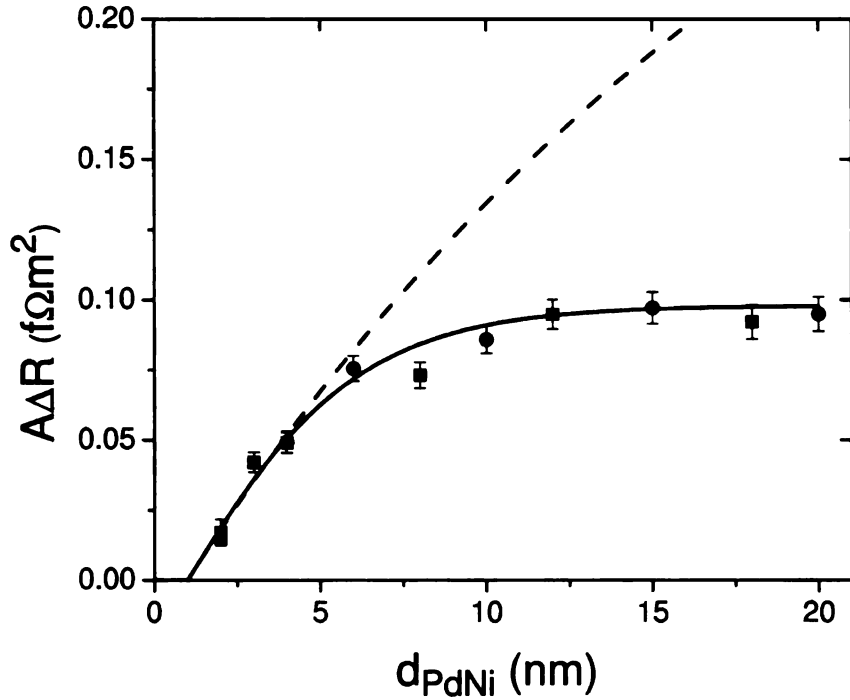


Figure 5.4:  $A\Delta R$  vs.  $d_{PdNi}$ . The solid line represents a fit to the data of the Valet-Fert equations. The fit provides an estimate of the spin memory length in PdNi of  $l_{sf}^{PdNi} = 2.8 \pm 0.5$  nm. The dashed line shows the result of a calculation assuming  $l_{sf}^{PdNi} = \infty$ .

According to the above equations, a plot of  $A\Delta R$  vs.  $d_{PdNi}$  should be linear at small values of the PdNi thickness and then saturate at large values. Valet-Fert[82] theory interpolates between these two limiting cases, and the crossover between the two behaviors is used to extract the spin diffusion length,  $l_{sf}$ . Several material parameters required for fitting the data to Valet-Fert equations were obtained from previous experiments. The resistivity of PdNi alloy,  $\rho_{PdNi} = 121 \pm 6$  nΩm was obtained by performing Van der Pauw measurements on 200 nm thick PdNi films. Also, a separate experiment performed to determine the dead layer between PdNi and Cu interface indicated,  $\delta_{dead} = 1.1 \pm 0.4$  nm [87].

Fig. 5.4 shows the specific magnetoresistance,  $A\Delta R$ , vs. PdNi thickness, for all of our samples. The data start out increasing nearly linearly with  $d_{PdNi}$ , then flatten out when  $d_{PdNi}$  exceeds about 10 nm. The solid line is a fit to the data of the

Valet-Fert equations [82]. The fit yields the spin-diffusion length of  $l_{sf} = 2.8$  nm. To illustrate the role of the finite spin memory length in the fit, the result of calculation using  $l_{sf}^{Py} = \infty$  is shown by a dashed line in Fig. 5.4.

This small value of spin-diffusion length ( $l_{sf} = 2.8$  nm) in PdNi was initially a surprise, because it was much shorter than the mean free path ( $l_e = 10.6 \pm 1$  nm) obtained through our measurements on PdNi based Josephson junctions. Whereas in a standard picture of diffusive transport in metals, the spin-flip and/or the spin-orbit scattering happens on a length scale much larger than the mean free path in that metal, i.e.  $l_{sf} > l_e$ . After this experiment was performed, Hamood graduated but this puzzle lingered on for a while. During this period, we accidentally found that our PdNi films have an out-of-plane magnetic anisotropy. This cast some doubt on our ability to attain P (parallel) or antiparallel (AP) states in Hamood's spin valve samples. This led us to believe that the small spin-diffusion length in our PdNi alloy could be a result of out-of-plane magnetic anisotropy in PdNi. We believe that the out-of-plane magnetization of PdNi can cause precession of spins initially aligned along in-plane (Py magnetization direction), thus enhancing the spin memory loss in our samples.

### 5.3.2 Spin Valves (Spoiler Geometry)

In order to suppress the influence of out-of-plane component, a new experiment was proposed by Prof. Pratt. Although Hamood had graduated by then, the accurate measurement of spin diffusion length in PdNi alloy was very crucial to our experiment. All the experiments henceforth were done by me. According to Prof. Pratt's new idea, exchange biased spin valves of the form Cu(10)/Py(24)/Cu(20)/PdNi( $d_{PdNi}$ )/Py(8)/FeMn(8)/Cu(10) were made, with  $d_{PdNi}$  varying from 0 - 15 nm. The aim was to pin the PdNi layer via the thin Py layer so that the magnetization in PdNi is forced to lie in-plane. After deposition the samples are heated

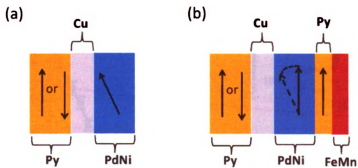


Figure 5.5: (a) Schematic for Hamood's spin valve showing the possible out-of-plane component of magnetized PdNi. (b) Schematic for our new spin valves, where PdNi layer is force-pinned "in-plane" via an exchange-biased coupling to Py/FeMn.

to 170°C, above the blocking temperature of FeMn, in a vacuum pumped pinning chamber and cooled to room temperature in an in-plane field of 190 Oe. This causes PdNi layer to be exchange coupled to the thin Py layer, which in turn is exchange biased in-plane (in the direction of the applied field) by the FeMn layer [88]. Magnetization measurements performed on PdNi/Py/FeMn show that both PdNi and Py are exchange-biased by this procedure. The in-plane magnetization of the pinned Py layer also constrains the PdNi magnetization to be in-plane. Effectively, the overall structure is such that Py layer on the left side acts as a "free" layer whereas PdNi acts as an in-plane "pinned" layer because of its proximity with a strongly exchange biased Py layer. The schematic of this geometry is shown in Fig. 5.5. We call this the *spoiler* geometry[89] because, with  $\beta_{Py} \gg \beta_{PdNi}$ ,  $A\Delta R$  is largest in the absence of PdNi layer, whereas as the PdNi thickness is increased, the signal diminishes until it finally reaches a much smaller value corresponding to that of a Py/Cu/PdNi spin valve. For  $d_{PdNi} > l_{sf}^{PdNi}$  the Valet-Fert theory approximately gives,

$$A\Delta R(d_{PdNi}) - A\Delta R(\infty) \propto \exp(-d_{PdNi}/l_{sf}^{PdNi}) \quad (5.21)$$

Figure 5.6 shows that in the spoiler geometry  $A\Delta R$  decreases rapidly with  $d_{PdNi}$

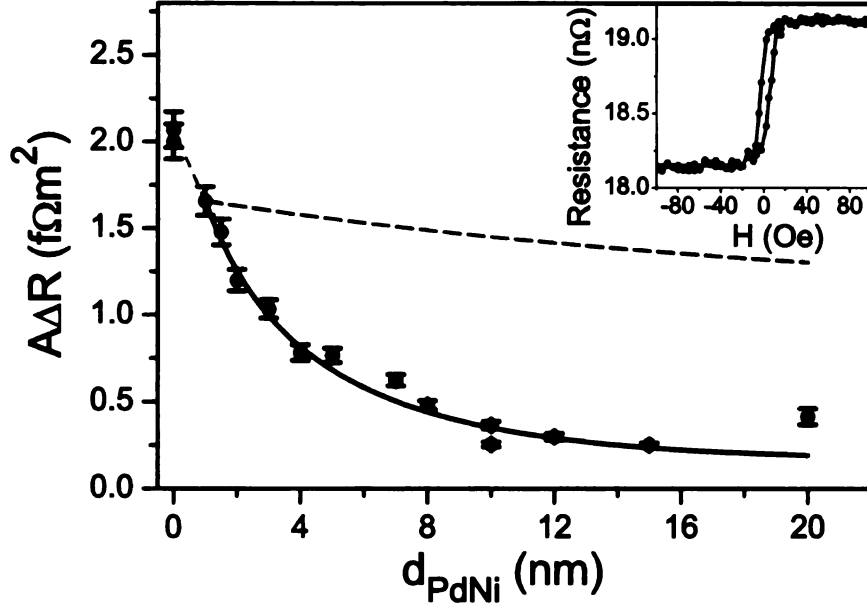


Figure 5.6:  $A\Delta R$  vs.  $d_{PdNi}$  for “spoiler” spin valves of the form  $Py/Cu/PdNi/Py/FeMn$ . Without  $PdNi$ , these are high-performance  $Py/Cu/Py$  spin valves with large  $A\Delta R$ . As the  $PdNi$  thickness increases,  $A\Delta R$  drops because of the low spin-scattering asymmetry in  $PdNi$  relative to  $Py$ , i.e.  $\beta_{PdNi} \ll \beta_{Py}$ . The black dot-dashed line shows a linear interpolation between first two points. The black solid line is a fit to the Valet-Fert equations for the rest of the points, giving  $l_{sf}^{PdNi} = 5.4 \pm 0.6$  nm. The red large-dashed line is obtained with  $l_{sf}^{PdNi} = \infty$ . Inset: Raw magnetoresistance ( $R$  vs  $H$ ) data for the sample with  $d_{PdNi} = 2$  nm.

and then saturates. The figure in the inset shows raw GMR data for the sample in spoiler geometry with  $d_{PdNi}=2$  nm. The black line shows the numerical data fit using Valet-Fert theory. The fitting is done to all the data points excluding the first point where  $d_{PdNi} = 0$ , since it does not have  $PdNi/Cu$  or  $PdNi/Py$  interface. The spin-diffusion length obtained from the fit is  $l_{sf}^{PdNi} = 5.4 \pm 0.6$  nm.

### 5.3.3 Discussion of the Results

We obtain two different values of spin-diffusion length via two different methods. Hamood’s spin-valves indicated a smaller spin diffusion length in  $PdNi$  in comparison to the spin-diffusion length measured later in the exchange-biased spin valves. The longer value of  $l_{sf}^{PdNi}$  obtained from our second experiment supports the hypothesis

that the magnetization in the first set of samples was highly non-uniform due to the out-of-plane magnetic anisotropy in PdNi films. The exchange bias in the second set of samples forced the PdNi magnetization to lie in the plane of the film, which led to a decreased inhomogeneous magnetization while increasing the spin diffusion length. The fact that  $l_{sf} < l_e$  even for the second set of samples indicate that the PdNi magnetization is still inhomogeneous even after being exchange-coupled via the Py layer.

During the course of work, we learned about the work done by Campbell and co-workers[90, 91] 30 years ago demonstrating that Ni impurities in Pd exhibit strong local orbital moment, which is indicative of strong spin-orbit coupling. This led us to believe that both the origin of out-of-plane magnetic anisotropy as well as small spin diffusion length in our PdNi alloy is a result of strong spin-orbit coupling.

#### **5.3.4 Strong spin orbit coupling in PdNi alloy**

In ferromagnets, the magnetization tends to align along certain preferred directions called ‘easy’ axes. This property of having preferred direction is called *magnetic anisotropy*. The magnetic anisotropy can have its origin in sample shape, crystal symmetry, stress or directed atomic pair ordering. Normally in thin films the shape anisotropy dominates the preferred direction of magnetization, thus causing it to lie in the plane of the film. But our magnetization studies have shown that the preferred magnetization direction in PdNi films is perpendicular to the plane of the film thus indicating that the magnetocrystalline anisotropy rather than the shape anisotropy dominates the preferred direction in PdNi alloy. To understand how the perpendicular anisotropy is indicative of strong spin-orbit coupling, it important to understand the origin of magnetocrystalline anisotropy.

##### **Origin of Magnetocrystalline Anisotropy**

What happens microscopically when fields are applied to rotate the spin system

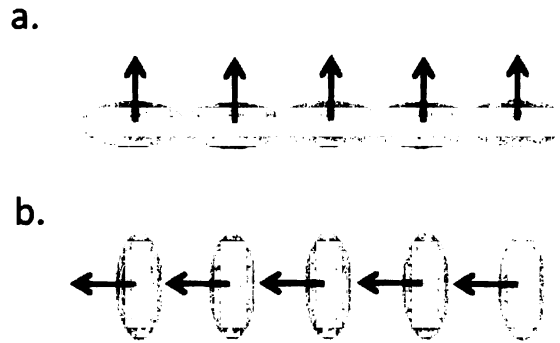


Figure 5.7: *Fig. (a) shows the magnetization pointing in the easy direction (say) with the orbital components aligned along the long axes (x-axis). The orbital components (which are no longer spherical because of the spin-orbit coupling) favor the overlap. Fig. (b) Shows the result of forcing the magnetic spins perpendicular to the easy axis. The orbital components no longer have favorable overlap with each other. Taken from Nicola Spaldin's book [92].*

of a domain away from the easy axis?

That is, microscopically when a field is applied to re-orient the direction of spins in a domain, not only the electron spin but also the orbit needs to be reoriented, because of the spin-orbit coupling. However, if the orbit is also strongly coupled to the lattice (or to the electric field created by all nearby ions-also known as “*crystal field*”), any attempt to rotate the spins is also resisted by the orbit. This is also explained by the schematic shown in Fig. 5.7. This directional nature of the bonding causes certain crystallographic directions to be more favorable than the others. It is possible in case of PdNi that the film grows with a uniform strain. It is perhaps this strain-induced crystal field along with a strong spin-orbit coupling that leads to a preferential out-of-plane magnetocrystalline anisotropy seen in this material. Most of the materials in fact have fairly weak spin-orbit coupling, and so the magnetocrystalline anisotropy is not particularly strong. The perpendicular anisotropy in PdNi thin films is therefore a strong indication of a strong spin-orbit coupling.

We believe that the strong spin-orbit coupling is not only manifested in perpendicular anisotropy seen in PdNi thin films but also in the short spin-diffusion length of the alloy. Furthermore, local inhomogeneities in the strain due to crystalline defects or grain boundaries could cause local fluctuations in the magnetic anisotropy direction, which further adds up to an enhanced spin memory loss. Our two methods of measuring spin diffusion length resulted in the values  $l_{sf}^{PdNi} = 2.8 \pm 0.5$  nm and  $5.4 \pm 0.6$  nm. The smaller of these values is a result of unpinned PdNi layer, which we now believe is a result of conflict between the shape induced in-plane anisotropy and the out-of-plane magnetocrystalline anisotropy. Nevertheless, it could be equally argued that the larger of these values (seen for the pinned PdNi layer), could be a result of enhanced in-plane homogeneity than due to the reduction of out-of-plane component.

## 5.4 Spin Diffusion Length in PdFe

In our search for the right conditions and materials needed for the survival of long-range triplet component, we realized that if we want to work with weakly ferromagnetic systems (mostly alloys), it's important to estimate the spin-diffusion length *a priori*. Measurements performed by Campbell and co-workers in the 1970's, in addition to implying strong spin-orbit coupling in PdNi alloy also showed that spin-orbit coupling in dilute PdFe alloys is comparatively weak. In fact, the past studies have described PdFe alloy with Fe concentration of 1.4% as a nearly ideal Heisenberg ferromagnet [93]. This motivated us to measure  $l_{sf}$  in PdFe, with the hope that it would be much longer than in PdNi.

### 5.4.1 Characterization of PdFe Alloy

PdFe films were sputtered using a 5.6 cm diameter Pd target with a single Fe plug of diameter 6.6 mm in the center. The Fe concentration in our PdFe sample was confirmed by three different methods:

1. EDAX
2. Curie Temperature
3. Saturation magnetization.

An energy dispersion X-ray (EDX) experiment performed on a 400 nm thick PdFe film indicated Fe concentration of about 1.6 at. %, but with a very large uncertainty due to the very small Fe concentration. In order to get accurate concentration of Fe in PdFe alloy, the magnetization  $M$  vs temperature of a 80 and 400 nm thick PdNi sample was measured using a superconducting quantum interference device (SQUID) magnetometer. This is shown in Fig. 5.8. The 80 nm film showed smaller magnetization and Curie temperature compared to the 400 nm film, which could be due to strain during growth. The Curie temperature of 44 K obtained from the 400 nm thick film provides an estimate of the Fe concentration of 1.1 at. % [93]. In yet another method, the concentration was obtained from the saturation magnetization measured for the same 400 nm sample. The measured magnetization of  $M_{PdNi} = 63 \text{ emu/cm}^3 = 0.1 \mu_B/\text{Fe atom}$ , according to ref. [93] corresponds to an Fe concentration of  $\approx 1.4$  %. These three determinations of the Fe concentration are reasonably consistent, and lead us to our best estimate of 1.3 at. %.

### 5.4.2 Magnetic Anisotropy

Samples in the form of Nb(150)/Cu(10)/PdFe(x)/Cu(10)/Nb(25), with variable thickness of PdFe layer were made for the magnetic measurements. Fig. 5.9 shows  $M$  vs.  $H$

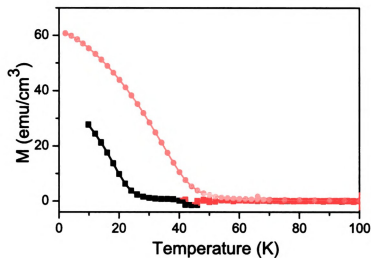


Figure 5.8: Black squares are the data points for  $M$  vs.  $T$  for samples of the form  $Nb(150)/Cu(10)/PdFe(x)/Cu(10)/Nb(25)$ , with 80 nm thick PdFe layer. Red circles are the data points for  $M$  vs.  $T$  for a 400 nm thick PdFe film. The films were zero-field cooled to low temperature and then the magnetization was measured by applying an in-plane field of 500 G. The temperature was then increased gradually to 100 K keeping the field constant. The Curie temperature of the 400 nm film indicated an Fe concentration of about 1.1%.

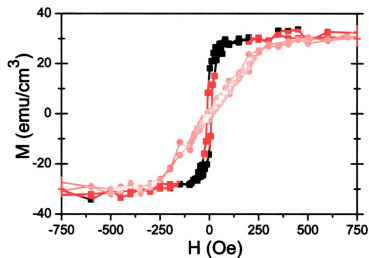


Figure 5.9:  $M$  vs.  $H$  at  $T = 10$  K for a 80 nm thick PdFe film grown as a  $Nb(150)/Cu(10)/PdFe(80)/Cu(10)/Nb(25)$  multilayer, with  $H$  pointing in-plane (black squares) and out-of-plane (red circles)

data at  $T = 10$  K for one such sample with a 80 nm thick PdFe-layer. Measurements were made with  $H$  both in-plane and out-of-plane. One can clearly see a sharp switch-

ing to the saturation magnetization when the field is applied in-plane, whereas a large field of  $\approx 300$  Oe is required to attain the same saturation magnetization when the field is applied out-of-plane. The strong preference for in-plane magnetization indicates dominance of shape anisotropy over magnetocrystalline anisotropy in these PdFe thin films. Similar results confirming in-plane magnetic anisotropy were seen in 60 nm and 400 nm thick PdFe films of similar geometry.

### 5.4.3 Double Exchange Biased Spin Valves

#### (Spin Valves of Type FeMn/Py/Cu/PdFe/Cu/Py/FeMn)

In order to measure  $l_{sf}$  of PdFe, we sputter hybrid spin valves of the form Cu(5)/FeMn(8)/Py(8)/Cu(10)/PdFe( $d_{PdFe}$ )/Cu(10)/Py(8)/FeMn(8)/Cu(5). These spin valves are sandwiched between two thick Nb electrodes. After sputtering, the two Py layers are pinned to the FeMn via exchange bias process as described in the earlier section. These samples can be thought of as two FeMn/Py/Cu/PdFe hybrid spin valves set back-to-back, with their MR signals adding. The advantage of this geometry relative to the first geometry we used with PdNi is that the magnetoresistance signal is twice as large.

Raw magnetoresistance data are shown in the inset to Fig. 5.11 for the sample with  $d_{PdFe} = 15$  nm. The coercivity of PdFe layer is  $\approx 15 - 20$  Oe, the magnetization of PdFe layer is seen to switch at small fields. A plot of  $A\Delta R$  vs.  $d_{PdFe}$  is shown in Fig. 5.11. A fitting procedure using Valet-Fert equations yields the spin diffusion length,  $l_{sf}^{PdFe} = 9.6 \pm 2$  nm. Although this value is larger than that obtained for the PdNi, it may not be long enough for our study of LRTC.

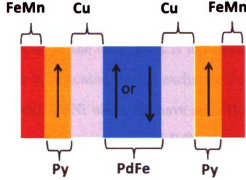


Figure 5.10: Schematic for double exchange biased spin valve of the form  $FeMn/Py/Cu/PdFe/Cu/Py/FeMn$ . An antiferromagnetic layer ( $FeMn$ ) is used to pin the outer  $Py$  layers via an exchange bias mechanism. The  $PdFe$  layer acts as a free layer.

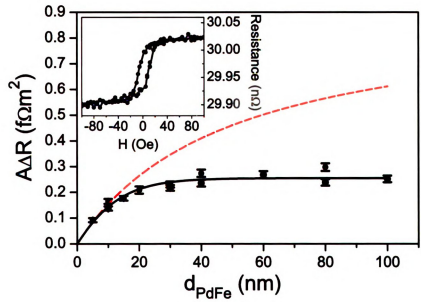


Figure 5.11:  $A\Delta R$  vs.  $d_{PdFe}$  for the double hybrid spin valves containing  $Py$  and  $PdFe$  alloy. The black solid line is a fit to the data of the Valet-Fert equations, with the spin memory length in  $PdFe$  of  $l_{sf}^{PdFe} = 9.6 \pm 2.0$  nm. The red dashed line shows the result of a calculation assuming  $l_{sf}^{PdFe} = \infty$ . Inset: Raw magnetoresistance data for the sample with  $d_{PdFe} = 15$  nm.

### 5.4.4 Discussion of Results

We chose to work with a weakly ferromagnetic alloy with the hope that it would be less detrimental to the observation of long-range triplet correlations. A clear signature

of LRTC would be the observation of Josephson current penetrating the F-layer over a distance much longer than the length scale associated with conventional spin-singlet correlations. This length scale in the clean limit is indicated by the mean free path,  $l_e$ , and in the dirty-limit it is indicated by the exchange length,  $\xi_F = \sqrt{(\hbar D/E_{ex})}$ . In our past experiments with PdNi alloy, we have seen that  $l_e > l_{sf}$ . We believe that the magnetically inhomogeneous nature of PdNi destroys the spin memory by rotating the spin on a length scale much smaller than the mean-free path  $l_e$ . This eliminated any hope of observing long-range triplet correlations in PdNi alloy. The spin-diffusion length measured in PdFe alloy  $l_{sf}^{PdFe} = 9.6 \pm 2$  nm is slightly larger than the spin diffusion length measured in PdNi alloy  $l_{sf}^{PdNi} \approx 2.8 - 5.3$  nm, however the situation is still not ideal. Even if we expect the mean free path of the 1.4% Fe alloy to be longer than that of the 12% Ni alloy, the long-range triplet penetration will be damped by any process that changes the electron spin.

## Chapter 6

# Spin-Triplet Superconductivity

In Chapter 4 we presented the results obtained for S/F/S Josephson junctions using a weakly ferromagnetic alloy PdNi. Our results show that the critical current density in our junctions oscillates and decays as the F layer thickness is increased. Both the oscillations as well as the short length scale of the decay ( $\xi_F=10$  nm) are indicative of standard spin-singlet correlations in our experiment. We concluded that the short-spin memory length in our PdNi alloy or an unfavorable domain structure were possible reasons behind lack of long range triplet correlations. A separate GMR experiment as described in Chapter 5 was performed to measure the spin memory length, the results of which indeed confirmed the short spin diffusion length in PdNi alloy ( $l_{sf}= 2.8$  nm). This directed our search towards ferromagnetic materials that will support propagation of the LRTC. Past studies have shown long spin memory length in strong ferromagnets like Ni and Co. For e.g. Pure Co has indicated a spin memory length of 40 nm [94, 95] whereas Ni gives a value of about 21 nm [89]. This led us to focus our attention towards making Josephson junctions using strong ferromagnets.

## 6.1 Ferromagnetic Josephson Junctions using Ni

Figure 6.1 shows  $I_c$  vs  $H$  obtained for a S/F/S Josephson junction using a strong ferromagnet, Ni. The pattern differs significantly from the standard Fraunhofer pattern observed earlier for Josephson junctions using weakly ferromagnetic alloys (See Chapter 4, section 4.1). Aware of our adeptness in making reliable Josephson junctions, we realized that the origin of irregularities in our Fraunhofer pattern was a result of our choice of F-material. Later, similar results were observed by my colleague Mazin when he was working on Josephson junctions using Co-layer [96]. Several other groups studying S/F/S Josephson junctions have seen similar random-looking Fraunhofer patterns [97].

### Physics Behind the Irregularities Seen in Fraunhofer Pattern

In Chapter 4, section 4.1, we studied Josephson junctions using weakly ferromagnetic alloys CuNi and PdNi. We saw nearly an ideal Fraunhofer pattern in virgin as well as magnetized state of the sample. However, the results obtained using strong ferromagnet varied drastically from our earlier observation using weak ferromagnet. To understand this better, let us refer back to the equation for critical current given in Chapter 2, section 2.6.3,

$$I_s = \int J(x, y) dx dy \quad (6.1)$$

where,

$$J(x, y) = J_c \sin \gamma = J_c \sin \left( \Delta\theta + \frac{2\pi}{\Phi_0} \int \mathbf{A}(\mathbf{x}, \mathbf{y}) \cdot d\mathbf{l} \right) \quad (6.2)$$

In macroscopic samples the magnetization breaks into domains. Due to the domains pointing in random directions, the term containing the vector potential performs a random walk as one moves across the sample. In order to solve the above equation, one must therefore integrate the current density across the area of the junc-

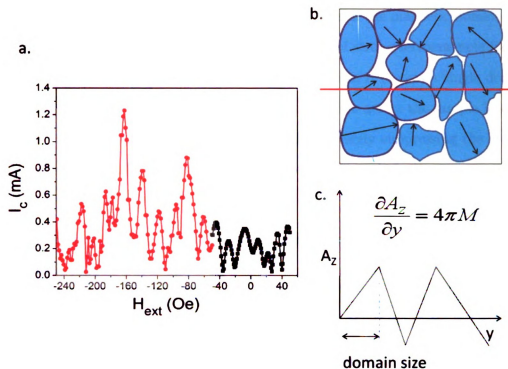


Figure 6.1: (a) Critical current  $I_c$  vs. in-plane magnetic field  $H_{ext}$  for a Nb/Ni/Nb Josephson junction of diameter  $10\ \mu\text{m}$ , with  $d_{Ni} = 11\ \text{nm}$ . The black points (squares) represent the virgin state measurement, whereas the red points (circles) are obtained after magnetizing the sample in an external field of 1000 Oe. (b) The large magnetic domains in ferromagnetic layer. (c) The vector potential taken across the red line shown in part (b). The large domain sizes cause the vector potential to deviate severely from the zero.

tion, taking into account the spatial dependence of the magnetic vector potential  $\mathbf{A}$  due to the domains. If the magnetic domains are very small and/or the magnetization is very weak as in the case with weak ferromagnetic alloys, then the vector potential term stays near zero in all parts of the junction, and the critical current is hardly affected. This leads to nearly ideal Fraunhofer patterns for Josephson junctions using weak ferromagnets like CuNi and PdNi. But if the magnetic domains are large and/or have large magnetization as in the case of strong ferromagnets like Ni or Co, the vector potential deviates far from zero even as it crosses a single domain as shown in Fig. 6.1. This large vector potential variation across the sample leads to a positive contribution to the overall phase  $\gamma$ , thus severely suppressing the critical current. This can lead to complete destruction of the Fraunhofer pattern as seen in Fig. 6.1.

In principle, a regular Fraunhofer pattern can be recovered if the sample is completely magnetized. For a sample magnetized by applying large positive field, a regular Fraunhofer pattern should be obtained when the flux due to an external magnetic field cancels the flux in the junction. This however should lead to a shift in the Fraunhofer pattern as observed earlier in the case of Josephson junction using weak ferromagnetic alloys. This shift is given by,

$$H_{shift} = \frac{-\mu_0 M d_F}{(2\lambda_L + d_F)} \quad (6.3)$$

However, the above argument holds only if the coercive field of the magnetic material is large enough. For small coercive fields the applied field can lead to variation in the magnetic domain structure even as one is attempting to measure the Fraunhofer pattern. For the case of the Ni sample shown in Fig. 6.1, the largest peak in the critical current  $I_c$  vs. field  $H_{ext}$  after magnetization is found near -160 Oe, whereas the expected shift calculated from the known saturation magnetization of Ni is  $\sim -207$

Oe. Since the coercive field in our film was expected to be around 180 Oe, we believe that the observed discrepancy is caused either by some rotation of the magnetization in the domains or some domain wall motion. [The coercive field of 180 Oe was in fact measured in a different 9 nm thick Ni film.]

## 6.2 Reduction of Flux

With the distortions seen in the case of Josephson junctions using Ni, it is difficult to get a good measure of the maximum critical current. To reduce the distortion of the Fraunhofer pattern it is important to reduce the flux in the junction. We suggest the following mode of operation to reduce the flux in the junction:

1. **Reducing Thickness of the F-layer:** Use of ultra-thin ferromagnetic layers ensures reduction in flux in the junction. Under this condition, the flux enclosed in the junction due to a single large magnetic domain can be much less than one flux quantum, and one then safely ignore the contribution to flux from the magnetization of the junction. Since a positive indication of LRTC can only be sought at thicker values of F-layer, this option was not available to us. In addition, the magnetically dead layers formed at the interfaces form an added disadvantage in working with ultra-thin ferromagnetic layers.
2. **Reducing Lateral Dimension of the Junction:** Fabricating devices with ultra small lateral dimension reduces the flux in the junction. This option was pursued by Blamire and his co-workers while working on Josephson junctions with strong ferromagnets like Ni, Co, Fe and Py [27, 28]. A similar approach was taken by Strunk and his co-workers while working with Gd [18]. This method becomes less effective as the thickness of the ferromagnetic layer is increased, and hence was not favored in our study of LRTC. In addition, working with smaller lateral dimension restricts the possibility to introduce magnetic

inhomogeneities *via* multidomain structure that is naturally present in devices of larger dimension. Such inhomogeneities may contribute to the generation of LRTC as predicted by various theory papers [8, 33, 34]. Our aim during the course of this study has been to exploit such inhomogeneities in the observation of LRTC.

3. **Use Ferromagnets with Small Domain Size and/or Small  $E_{ex}$ :** This gives another way to reduce the flux in the junction. This option was recently pursued by us using a weakly ferromagnetic alloy, PdNi. We have obtained excellent Fraunhofer patterns for demagnetized samples as well as for the uniformly magnetized samples. The latter patterns were shifted in field, but the maximum value of the critical current was nearly unchanged. This indicated that the magnetization of the PdNi layer makes very little contribution to the total magnetic flux of the sample. The details of this experiment are given in Chapter 4. The same is true for another weakly ferromagnetic alloy CuNi. However there was no indication of LRTC in our experiment. Our later measurements indicated that the short spin diffusion length ( $l_{sf} \approx 2.8$  nm) in this alloy restricted the long range propagation of spin-triplet correlations. Similar options utilizing weak ferromagnetic materials were also pursued earlier by various other groups [21, 23, 66], however no long-range Josephson effect was observed.
  
4. **Engineer the F-layer to have Zero Net Magnetic Flux:** One can engineer the F-layers such that the net magnetic flux in the junction is zero. This can be done using antiferromagnetically coupled F/N/F layers. We call this configuration, “*synthetic antiferromagnet*”. This method not only reduces flux in the junction but it also gives us an opportunity to work with strong ferromagnets. The next section will describe in detail the experiments undertaken

by our group using this method.

### 6.3 Synthetic Antiferromagnet (SAF)

The idea of using a synthetic antiferromagnet in our Josephson junction stems from the GMR expertise of Prof. Pratt working in this field for a long time. Most of the work henceforth utilizes antiferromagnetically coupled F-layers in reducing the flux in the junction. Here I will give a brief overview of the physics behind antiferromagnetically coupled F-layers.

#### Oscillatory Exchange Coupling

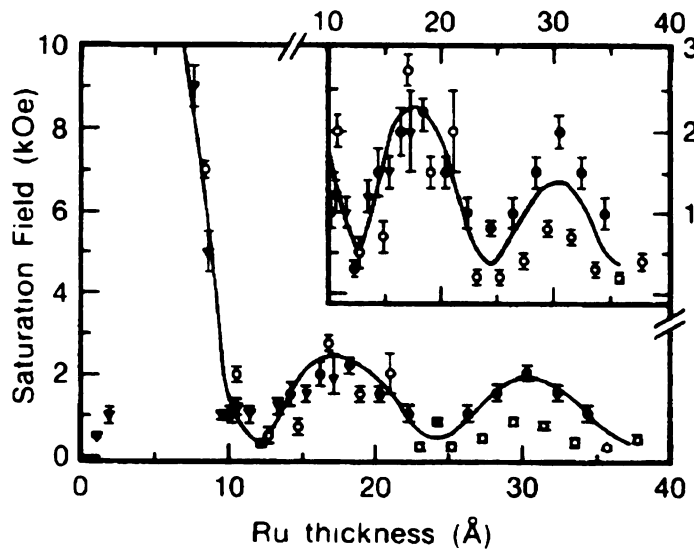


Figure 6.2: Field needed to saturate the magnetization at 4.2 K vs Ru thickness for  $Si(111)/(100 \text{ \AA}) Ru/[(20 \text{ \AA}) Co/t_{Ru} Ru]_{20}/(50 \text{ \AA}) Ru$  deposited at temperature of 40 C (filled circles), 125 C (Empty circles) and 200 C (cross). Taken from Parkin *et al.*, 1990 [98].

It has been known for a long time that when an impurity is placed in an electron gas, the background charge is redistributed to neutralize the impurity charge. This disturbance gives rise to decaying oscillations of electron density as a function of the distance from the impurity. These are called *Friedel oscillations*. It turns out

that something similar happens when a magnetic impurity atom is in a metallic surrounding. In this case, the magnetic impurity gives rise to an oscillatory spin polarization of the electron density that decays as a function of the distance from its source. As a result the magnetic coupling of the next atom placed close to the magnetic impurity can either be parallel or antiparallel to the magnetic moment of the impurity atom depending on the sign of the induced spin polarization at that particular distance. This physical mechanism leads to the long range oscillation in exchange coupling between magnetic moments. The model described here is called the *RKKY model*. Such a mechanism is known to exist in rare-earth metals like Gadolinium (Gd). In 1986, Majkrzak *et al.* [99], while working on Gd/Y/Gd found antiparallel magnetic moments in the Gd layers, the origin of which was believed to be RKKY interaction. In 1988, Baibich *et al.* [83] found a similar anti-ferromagnetic coupling in Fe/Cr/Fe structures. A detailed study of such structures later led to the discovery of oscillatory dependence of the coupling on the thickness of the central layer. In particular, Parkin *et al.*(1990) [98] observed that the coupling in  $[\text{Co}/\text{Ru}]_N$  (and  $[\text{Fe}/\text{Cr}]_N$ ) structure oscillates between ferromagnetic and antiferromagnetic as the thickness of the spacer layer Ru (and Cr), is increased. Fig. 6.2 shows the Ru thickness dependence of the field needed to saturate  $[\text{Co}/\text{Ru}]_N$  multilayers. Large fields are required to saturate the multilayer when the Ru thickness is 6, 16 or 30 Å. The large saturation fields are indicative of antiferromagnetic coupling between the Co layers, whereas small saturation fields effect imply ferromagnetic exchange coupling between the Co layers.

### 6.3.1 Josephson Junctions using SAF of the form Co/Ru/Co

In this sub-section I will talk about the results obtained by my colleague Mazin while working on Josephson junctions using a synthetic antiferromagnet. These results are published in Phys. Rev. B **80**, 020506(R) (2009). Josephson junctions of the form

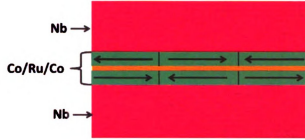


Figure 6.3: Schematic of the Josephson junction using a strong ferromagnet Co in Synthetically antiferromagnetic form (i.e. Co/Ru/Co form). In this configuration the domain in the top Co layer are antiparallel to the domains in the bottom Co layer, which leads to zero net flux in the junction. The antiparallel configuration is sensitive to the thickness of the Ru.

Nb/Cu/Co/Ru/Co/Cu/Nb were made using the techniques described earlier in this thesis. We refer to the central Co/Ru/Co trilayer as a synthetic antiferromagnet. The schematic of this junction is shown in Fig. 6.3. The magnetization of the two outer Co-layers is exchange-coupled in antiparallel direction *via* the 0.6 nm thick Ru layer in the center. As a result, the total magnetic flux in the junction is nearly zero and the junction exhibits nearly ideal Fraunhofer patterns as shown in the inset of the Fig. 6.4. The data for critical current vs. total Co thickness are shown in Fig. 6.4.

As seen from the graph,  $I_c$  decreases by four orders of magnitude as the total Co thickness varies from 2 to 23 nm. The overall decay fits well to a simple exponential decay. No discernible oscillations were seen. This is in accordance with several theory papers based on this topic [100]. However there was no indication of the LRTC, which as said earlier would manifest itself as a crossover to a slower decay at large Co thicknesses. The lack of LRTC in Mazin's experiment was attributed to two possible reasons: i) Large spin memory loss at the Co/Ru interface that restricts the long range propagation of triplets, ii) Lack of magnetic inhomogeneities in the Co layer,

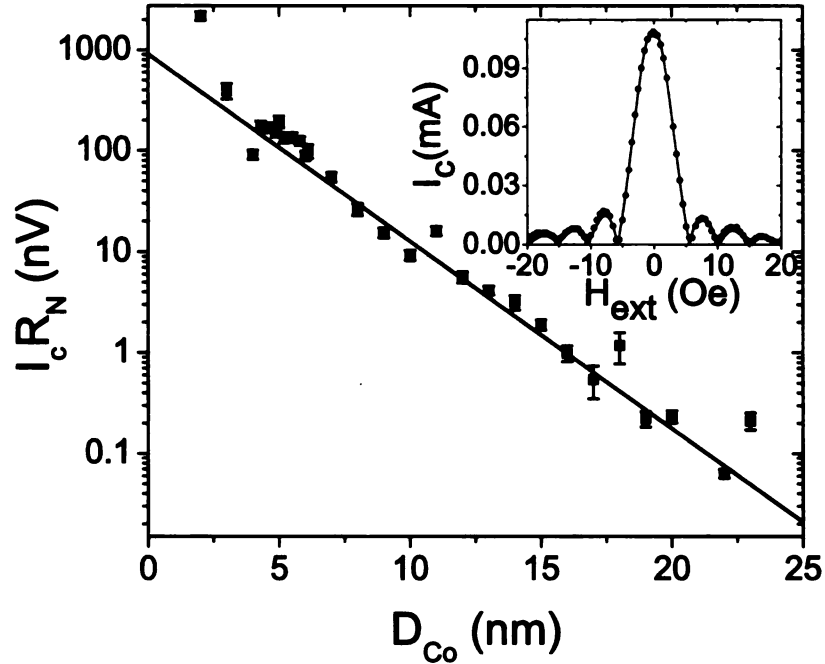


Figure 6.4: Product of critical current times normal resistance  $I_c R_N$  vs. total Co thickness  $D_{Co} = 2d_{Co}$  in the Josephson junction using SAF configuration. The solid line is a fit to an exponential decay, with the decay constant of  $2.34 \pm 0.08$  nm. The inset shows the excellent Fraunhofer obtained for Nb/Cu/Co/Ru/Co/Cu/Nb circular Josephson junction with total Co thickness  $D_{Co} = 2d_{Co} = 18$  nm. The pillar diameter is  $20 \mu\text{m}$ .

which as said earlier are essential for the generation of LRTC.

Figure 6.5 shows scanning electron microscopy with polarization analysis (SEMPA) done for a  $[\text{Co}/\text{Cu}]_N$  multilayer structure by John Unguris' group at NIST [101]. The samples used for this study were made in our sputtering system. The picture shows the magnetic domain structure with domain size  $\sim 3 \mu\text{m}$  in Co films. The domains are mostly oriented antiparallel, indicating lack of collinear magnetization needed for the generation of triplet correlations. However, when we started with this study our hope was to exploit the regions of non-collinear magnetization present in the domain walls.

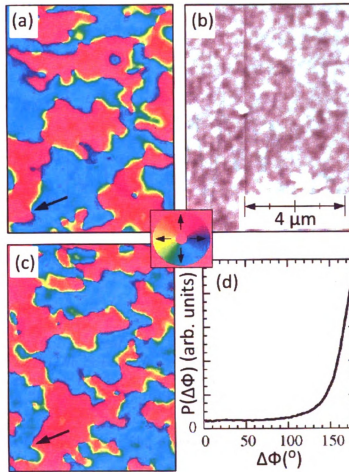


Figure 6.5: SEMPA images of the topmost Co layer magnetization (a) and topography (b) and second Co layer magnetization (c) in the  $[Co(6\text{ nm})/Cu(6\text{ nm})]_{20}$  sample. The magnetization direction is mapped into color as indicated by the color wheel in the center. A histogram of the difference in the magnetization direction between the two layers,  $\Delta\Phi$ , is shown in (d). (Figure taken from Borchers et al. [101])

### 6.3.2 Other Experiments using SAF Configuration

Not knowing if the spin memory loss is large at the Co/Ru interface, we decided to substitute Cu for Ru in our SAF Josephson junctions. We know that spin memory loss at the Co/Cu interface is only about 25% [102]. Here I report the results of the experiment identical to one performed by Mazin, but using SAF of the form Co/Cu/Co. Josephson junctions of the form Nb/Cu/Co/Cu/Co/Cu/Nb were made

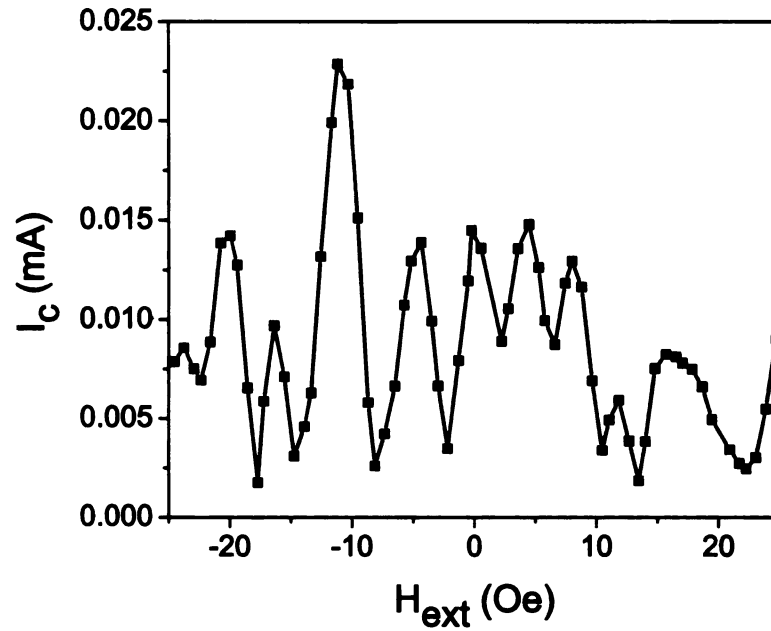


Figure 6.6: *Critical current vs. applied magnetic field obtained for Nb/Cu/Co/Cu/Co/Cu/Nb circular Josephson junction with total Co thickness of 14 nm. The pillar diameter is 20  $\mu\text{m}$ . The distortion in the Fraunhofer pattern is a result of incomplete flux cancellation in the junction.*

with the variable Co thickness. The magnetization of the two outer Co layers is exchange-coupled in antiparallel direction via the 0.6 nm thick Cu layer in the center. Fig. 6.6 shows the Fraunhofer pattern obtained for one such junction using total Co thickness  $D_{Co}$  of 14 nm.

The  $I_c$  vs  $H_{ext}$  differs significantly from the ideal Fraunhofer pattern obtained for the Josephson junctions employing the SAF of the form of Co/Ru/Co. This is because the antiferromagnetic exchange coupling in Co/Cu/Co trilayers is not as strong as in Co/Ru/Co trilayers. We also know this from magnetic measurements performed by Mazin, which showed a regular hysteretic loops with low saturation fields  $\sim 200$  Oe. This leads to an incomplete flux cancellation inside the Josephson junctions, which in turns leads to significant distortions in the Fraunhofer pattern. Past studies done by other groups have shown that the antiferromagnetic coupling strength in Co/Cu systems is sensitive to the crystalline orientation of the as grown films, which

according to the literature can be improved by implementing an appropriate buffer layer. However, we did not pursue this route any further at this time. Shortly after, Mazin performed GMR experiments to measure the spin-memory loss at the Co/Ru interface, the preliminary results (unpublished) of which indicate no more loss of spin-memory at the Co/Ru interface than at the Co/Cu interface.

Other systems including Ni/Ru/Ni, Ni/Ag/Ni were made and magnetic measurements were done to check for antiferromagnetic coupling. Our measurements of these showed regular hysteresis loops with low saturation fields indicating large ferromagnetic contribution from the coupled structure. They were therefore not found to be suitable SAF candidates in our study of LRTC.

## 6.4 Long-Range Triplet Correlations in Our Experiment

At this point, it was essential to put all the information together and realize that there are two important aspects to the study of spin-triplet correlations: the “generation” of spin triplet correlations and their “survival/propagation” in our Josephson junctions. Any further progress in this search implied a careful consideration of both aspects. Fig. 6.7 shows the basic idea behind this experiment.

### **Propagation of the LRTC (Central SAF Layer):**

Although working with a weak ferromagnet allows us to measure junctions with thicker ferromagnet materials, the spin-flip and/or spin orbit scattering in weak ferromagnetic alloys limits the survival possibility of the long-range component of the supercurrent. The current information on the spin diffusion length in PdNi, PdFe, CuNi did not look very promising. The strong ferromagnets on the other hand have long spin-memory length, however the aforementioned difficulties in getting a good Fraunhofer pattern indicate that they can be used only in Synthetic antiferromagnetic

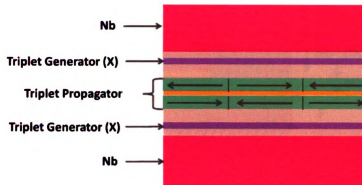


Figure 6.7: *Conceptual diagram representing the division of labor in our junction – the X-region close to the Nb interface is to facilitate the ‘generation’ of triplets, whereas the central SAF layer employing strong ferromagnet is essential in long range ‘propagation’ of the triplet correlations.*

(SAF) form. We therefore chose to rely on our SAF system as a propagator of triplet correlations. In the experiment that I will describe in this section, we have chosen to work with Co/Ru/Co as our SAF system.

#### **Generation of the LRTC (X Layer):**

Generation of the LRTC was another critical issue for this project. Although there are several theory papers that suggest different methods of generating LRTC, our approach during the course of this study was to utilize the naturally occurring magnetic domain structure in macroscopic samples. As described in earlier section, Mazin’s Josephson junctions using Co/Ru/Co failed to show any LRTCs indicating that Co may not have the right kind of inhomogeneous magnetization needed to induce the LRTC. On the other hand, although short spin diffusion length in weakly ferromagnetic alloy like PdNi and CuNi is known to limit long range propagation of LRTC, nothing conclusive could be said about their ability to generate triplet correlations. A recent experiment performed by Veshchunov *et al.* [72] on CuNi alloy revealed that the material has perpendicular magnetic anisotropy and has a small



Figure 1a. Here I will discuss the role of each layer in brief:

1. The purpose of the weakly ferromagnetic alloy PdNi or CuNi– inserted between the Co and Nb layers is to introduce magnetic inhomogeneity and thus facilitate the generation of triplet correlations.
2. The purpose of the central SAF layer, Co/Ru/Co, is to propagate the triplet correlations. The advantages of using Co-based SAF are three-fold: 1) The long spin diffusion length in Co helps in propagation of long range triplet correlations, 2) Using Co in SAF form ensures zero net flux in the junction. As a result, our data exhibit nearly-ideal Fraunhofer patterns (See Fig. 6.9) thus helping us in getting a reliable measure of the maximum critical current. 3) Co being a strong ferromagnet, destroys the spin singlet correlations on a length scale of only few nanometers, it however favors the propagation of long range triplet correlations. It therefore also acts as a filter of spin singlet correlations for large thicknesses.
3. The Cu layers between the X-layers and the Co layers serve two purposes. 1) They isolate the X and Co layers magnetically, so the magnetization of the X layers is not exchange-coupled to that of the Co layers. 2) The lower Cu layer used close to the Nb interface improves the growth quality of our sputtered Co [96].

Figure 6.10 shows the product of critical current and normal state resistance ( $I_c R_N$ ) vs. total cobalt thickness ( $D_{Co} \equiv 2d_{Co}$ ) for a series of samples with fixed PdNi layer thickness,  $d_{PdNi} = 4$  nm. For comparison, Fig. 6.10 also shows Mazin's data for identical junctions but without the PdNi layers. As the Co thickness is increased, the critical current of the Josephson junctions with the PdNi alloy decays very slowly which is in sharp contrast to the very fast decay observed in the junctions without PdNi alloy. In samples without PdNi,  $I_c R_N$  decays very rapidly with increasing  $D_{Co}$ ,

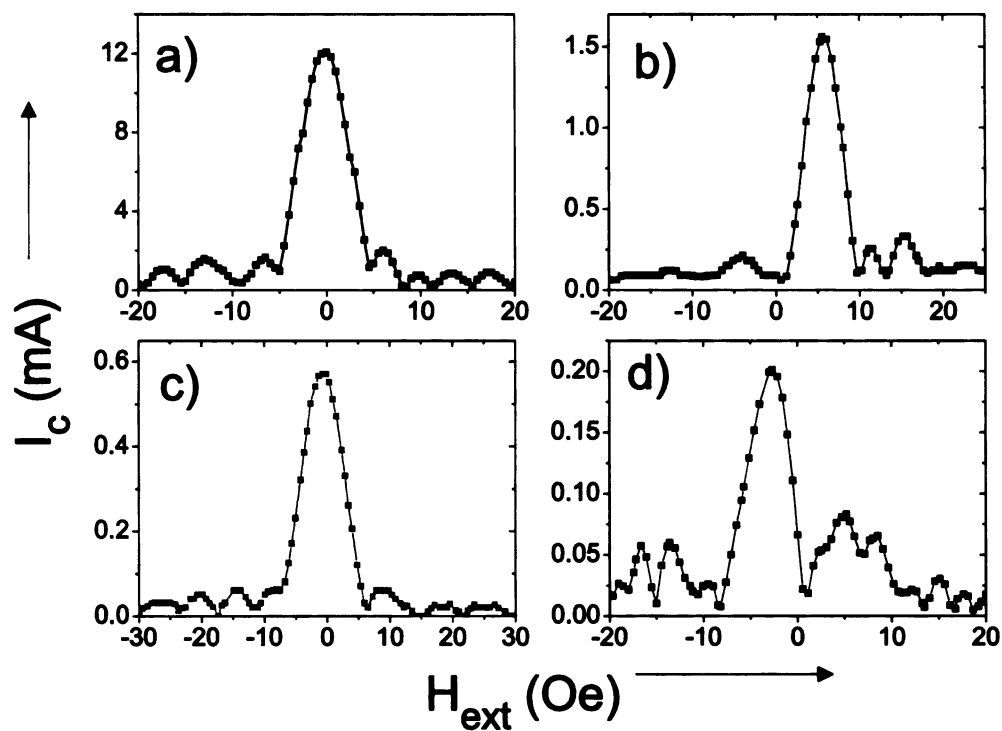


Figure 6.9: Critical current ( $I_c$ ) vs. applied magnetic field ( $H_{ext}$ ) for Josephson junctions with fixed PdNi-layer thickness  $d_{PdNi} = 4\text{ nm}$  and variable Co-layer thicknesses ( $d_{Co}$ ) a) 2nm, b) 7nm, c) 13nm, d) 18nm. The pillar diameters  $w$  are 20, 20, 10, 20  $\mu\text{m}$ , respectively.

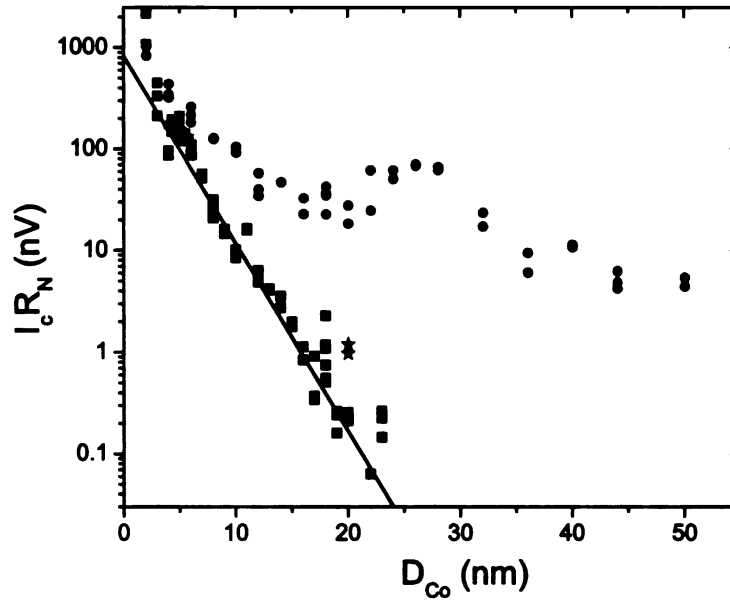


Figure 6.10: Product of critical current times normal state resistance,  $I_c R_N$ , as a function of total Co thickness,  $D_{Co} = 2d_{Co}$ . Red circles represent junctions with PdNi and  $d_{PdNi} = 4$  nm (fixed), whereas black squares represent junctions without PdNi layer (taken from Ref. [96]). (The solid line is a fit of the data without PdNi to a decaying exponential, also from Ref. [96]. In [96], data from multiple junctions with the same value of  $D_{Co}$  were represented by a single data point with an error bar; here, each device is represented by its own data point.) The blue stars represent measurements performed on Josephson junctions with triplet generator- PdNi placed only on one side of the junction.

on a length scale of just  $2.34 \pm 0.08$  nm [96]. The long-range character of the Josephson current in samples with PdNi is a strong evidence for spin triplet correlations in our system. There is a clear enhancement in critical current for the samples with PdNi over those without PdNi. For example, when  $D_{Co} = 20$  nm,  $I_c R_N$  is over 100 times larger in the samples with PdNi than in the samples without PdNi.

### 6.4.1 Strength of Triplet Correlations

#### Effect of PdNi Thickness Variation

Apart from the above mentioned clear indication of spin triplet correlations, we found that the strength of the triplet correlations can be controlled by varying the thickness of the PdNi layer.

Figure 6.11 shows  $I_c R_N$  vs.  $d_{PdNi}$  for samples with  $D_{Co}$  fixed at 20 nm. Without any X-layer,  $I_c R_N$  is very small, whereas when the thickness of PdNi is increased the  $I_c R_N$  increases until it reaches a maximum for  $d_{PdNi} \approx 3 - 6$  nm, after which it decreases again. The decrease in  $I_c R_N$  for large thicker PdNi signals the destruction of the spin-triplet correlations. This is perhaps because of the spin memory loss in the bulk of the PdNi when the layer thickness is increased. As measured in our GMR experiment, the spin memory length in PdNi was only about 2.8 nm [87]. This would therefore explain why there was no evidence for spin-triplet correlations in our Josephson junctions containing only PdNi layer [103]. However, having PdNi layer is essential in generation of triplet correlations in our experiment described above.

Additionally, we have also measured samples without the Cu buffer layer between PdNi and Co. Our measurements indicate no enhancement of the critical current in this case. The Cu buffer layer ensures magnetic isolation of layers, removing Cu leads to exchange coupling of the PdNi and Co layer. It is possible that the out-of-plane magnetization in PdNi is the source of magnetic inhomogeneity in our system. However, when PdNi is placed next to Co-layer, the exchange coupling of the layers

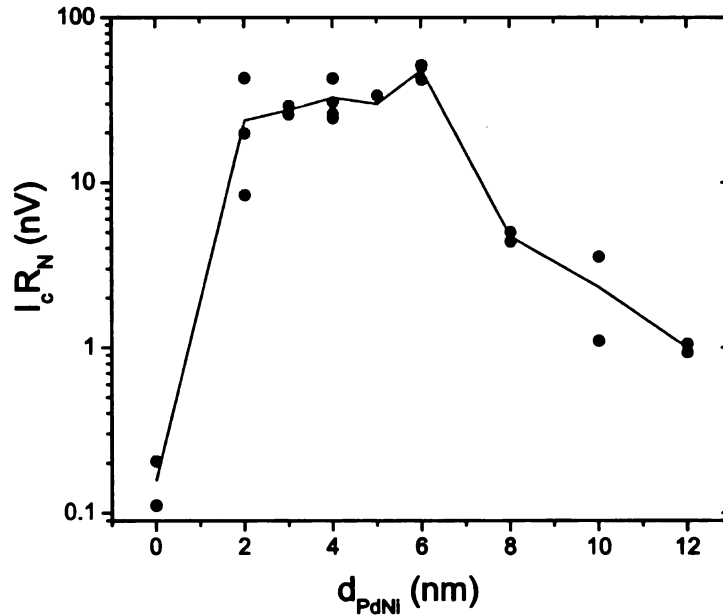


Figure 6.11:  $I_c R_N$  product as a function of  $d_{\text{PdNi}}$  for a series of junctions with fixed  $D_{\text{Co}} = 20$  nm. The  $I_c R_N$  first increases, then eventually decreases with increasing  $d_{\text{PdNi}}$ . Lines are guides to the eye.

force the PdNi moment to lie in-plane of the sample thus reducing the inhomogeneities essential for the generation of triplet correlations. However it is hard to definitively conclude anything about the microscopic mechanism that leads to triplet generation.

Since it is not possible to have Josephson current due to the interference between the singlet and triplet components, we decided to test our Josephson junctions by removing the PdNi layer from one side of the junction. These measurements are indicated by blue stars in the Fig. 6.10. We have seen an enhancement in the critical current that was five times larger than the spin-singlet current. However looking at large sample-to-sample fluctuations, it is hard to attribute this enhancement to any definite effect.

## 6.4.2 Where are the Triplets Generated?

Although a clear distinction was made in Fig. 6.7 indicating the region that generates triplet and the region which propagates triplet, in reality it is hard to strictly classify the process into two distinct events. We believe that there are two possible sources of non-collinear magnetization in our samples.

1. If the Cooper pairs experience non-collinear magnetization between adjacent domains in the X-layer, then domain size and out-of-plane magnetocrystalline anisotropy are likely to be key ingredients in generation of LRTC. Although PdNi [103] and CuNi [71, 72] alloy are known to have out-of-plane magnetic anisotropy, there is no information on the domain structure in PdNi alloy. Cu<sub>0.47</sub>Ni<sub>0.53</sub> alloy on the other hand is known to have domains that are of the order of 100 nm, which is not so different from the Nb coherence length  $\xi_S = 14$  nm [104]. It is also known that the competition between out-of-plane magnetocrystalline anisotropy and the in-plane shape anisotropy in thin films can lead to stripe domains with canted magnetization [105]. This could also be a possible cause of non-collinear magnetizations in our films.
2. It is also possible that the Cooper pairs experience non-collinear magnetization between the X layers and the Co layers. If this is true then almost any ferromagnetic layer could work in place of the X layers, provided the magnetization directions of the X and Co layers are independent. However the advantage of using weakly ferromagnetic alloys as our X-layer is to preserve good Fraunhofer patterns. Using a strong ferromagnet as the X layer increases the flux trapped in the junctions, which then leads to destruction of Fraunhofer pattern.

### 6.4.3 Temperature Dependence of the Triplet Samples

We have also studied the temperature dependence of the critical current in a couple of our samples that show long range triplet correlations. Fig. 6.12 shows  $I_c$  vs  $H$  measured at different temperatures for our Josephson junctions with  $D_{Co} = 26$  nm and  $D_{Co} = 50$  nm; for a fixed thickness of PdNi  $d_{PdNi} = 4$  nm.

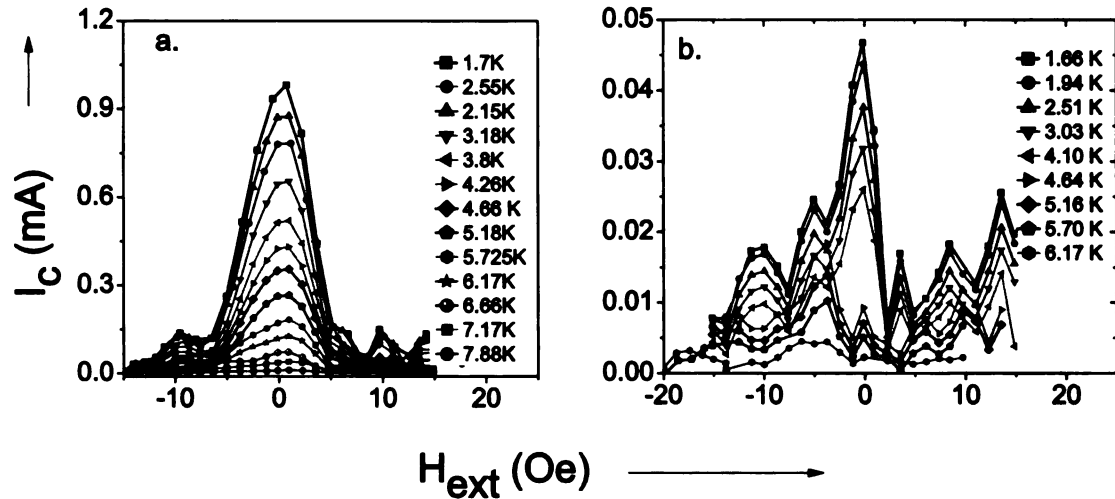


Figure 6.12:  $I_c$  vs  $H$  measured at temperatures in the range from 1.6-8 K for: (a) Josephson junction with  $D_{Co} = 26$  nm and  $d_{PdNi} = 4$  nm, (b) Josephson junction with  $D_{Co} = 50$  nm and  $d_{PdNi} = 4$  nm

Figure 6.13 shows monotonic decay of the normalized  $I_c R_N$  as a function of temperature. The nature of the decay is independent of the F-layer thickness.

According to theory for diffusive S/N/S junctions, the junctions are said to be in “short junction regime” if  $\Delta \ll E_{th}$ , or they are said to be in “long junction regime” if  $\Delta \gg E_{th}$ , where  $E_{th} = \hbar D/d^2$  is the Thouless energy,  $D$  is the diffusion constant, and  $d$  is thickness of the N-layer. In long junctions  $I_c R_N$  is limited by the value of  $E_{th}$ , or in other words it is sensitive to the change in thickness of the N-layer. However, qualitatively our measurements indicate no significant change in the nature of the decay for  $D_{Co} = 26$  nm and 50 nm, indicating that we are in the short junction regime where  $I_c R_N$  is dominated by the gap  $\Delta$ . We were therefore not able to measure

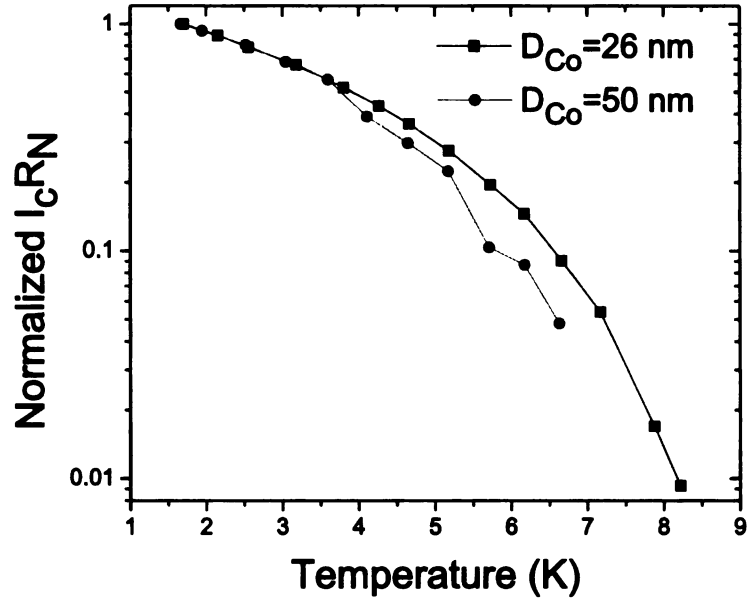


Figure 6.13: *Monotonic decay of critical current as a function of temperature. Our samples are in the short junction regime.*

the Thouless energy, which is another way to gauge the strength of our junctions. To get a reliable measure of the Thouless energy we need to measure junctions in the long limit. Such a measurement requires measuring the temperature dependence of a triplet sample with a very thick Co layer. Our measurements however indicate weak antiferromagnetic coupling for thicker samples, leading to poor Fraunhofer patterns, whence getting a reliable measure of critical current becomes difficult.

## 6.4.4 Discussion of the Results

### 6.4.4.1 Comparison between Theory and Experiment

Comparison of our results with theory is problematic because the magnitude of the spin-triplet supercurrent depends on the details of the PdNi or CuNi domain structure, while theoretical calculations exist only for idealized magnetic configurations. Nevertheless, there are three recent theory publications that are relevant to the sample geometry studied here. Our samples can be viewed as realizations of the S/F'/F/F''/S

junctions studied theoretically by Houzet and Buzdin [54], but with Cu buffer layers separating the three ferromagnetic layers. This paper assumes that the magnetization in three layers have same amplitude (same exchange energies) but different orientations and goes on to show that triplet contribution to the critical current is sensitive to: 1) The relative orientation of the magnetization in successive F-layers; 2) The thickness of outer F' and F'' layers. They predict maximum triplet supercurrent when the F' and F'' layer thicknesses are of the order of  $\xi_F$ . We do observe the predicted maxima in the triplet current for a certain thickness of outer PdNi-layer. There is an apparent qualitative agreement between the prediction and our result as seen in Fig. 6.11. More recently another two theorists, Volkov and Efetov, have worked on our sample geometry [49]. This paper assumes a sample geometry of the form S/F'/F/F''/S, but with the central F-layer composed of two domains with parallel or antiparallel magnetization. In contrast to Houzet and Buzdin paper, this paper assumes different exchange energies for central and outer F-layers. The qualitative dependence of the triplet current on the outer F-layer thickness is similar to the Houzet and Buzdin paper. Both the above mentioned papers work in the regime where  $E_{ex} < E_F$ . A third paper that is relevant to our sample geometry has just appeared in cond-mat [50]. In addition to the above geometry considerations, this paper has worked out problem in the clean limit and for moderately diffusive ferromagnets using the Eilenberger equations.

In conclusion, the comparison between theory and experiment is difficult because of the triplet sensitivity to: 1) size of domains and the domain walls, 2) orientation of magnetization in these domains and the domain walls, 3) relative orientation of magnetization between two adjacent F-layers, etc. More theoretical as well experimental work is therefore needed to understand this issue in detail.

#### 6.4.4.2 Confirmation of Triplet Correlations

In the “dirty” limit, where the mean free path,  $l_e$ , is the shortest relevant length scale in the problem, the spin-singlet supercurrent should decay on the length scale  $\xi_F = \sqrt{\hbar D_F / E_{ex}}$ , where  $D_F$  and  $E_{ex}$  are the electron diffusion constant and exchange energy in the ferromagnet. However Mazin’s Co-based Josephson junctions containing Co were in the “intermediate” limit, with  $l_e$  longer than  $\xi_F$ , but shorter than  $\xi_S$ , the superconducting coherence length. In that limit, the spin-singlet supercurrent decays on the length scale  $l_e$ . Mazin’s data gives an estimate of this length scale to be  $\sim 2.4 - 3.0$  nm; which is agreement with previous measurements done by Blamire and his co-workers [27]. This rapid decaying spin-singlet supercurrent for Mazin’s samples is also shown in Fig. 6.10. In contrast, when the PdNi-layer was added close to the Nb interface, we observed a huge enhancement in the critical current—for example, when  $D_{Co} = 20$  nm, the observed critical current was about 100 times larger in samples with PdNi than for the samples without PdNi. This gives us a clear confirmation of triplet supercurrent in our Josephson junctions. However, it is important to note how our samples shows no discernible decay until  $\sim D_{Co} = 30$  nm, which then is followed by large sample-to-sample fluctuations for thicker samples. This is because for the samples with larger  $D_{Co}$ , the Fraunhofer patterns were poor, which made it difficult to get an accurate measure of maximum critical for those junctions. We believe that this is because the antiferromagnetic coupling of the Co/Ru/Co trilayer is less effective for thicker Co layers. As said earlier, the spin-triplet supercurrent should decay over a much longer length scale given by the smaller of the normal metal coherence length,  $\xi_N = \sqrt{\hbar D_F / 2\pi k_B T}$ , or the spin memory length,  $L_{sf} = \sqrt{\hbar D_F / \tau_{sf}}$ , where  $\tau_{sf}$  is the mean time between spin-flip or spin-orbit scattering events. However the large fluctuations seen in our samples makes it impossible to get an accurate measure of the triplet decay constant for our samples.

Looking back, there were hints of long-range proximity effects in S/F hybrid systems, some of them as early as 10 years ago [5, 106, 7, 107, 10, 32], but there was no way to control the observed effects. For a long time the main problem in obtaining definitive and reproducible evidence of LRTC was to identify and invent a mechanism that creates LRTC. Our results give a strong evidence of induced spin-triplet correlations, the magnitude of which can be controlled by varying thickness of the PdNi layer.

The spin-triplet pair correlations observed here and discussed in Ref. [11] are quite different from those believed to occur in materials such as  $\text{Sr}_2\text{RuO}_4$  [3]. The Cooper pairs responsible for the LRTC effect seen in this experiment are believed [9, 8] to be a result of unusual s-wave triplet pairing mechanism that is odd under time reversal, or odd in frequency. Nevertheless, the observation of enhanced supercurrent in itself does not provide a conclusive evidence of this unusual symmetry of the pair correlations. More experiments need to be done to affirm the symmetry of observed long-range pair correlations.

# Chapter 7

## Discussion and Further Work

### 7.1 Our Aim

The main aim of our project was to present an irrefutable, reproducible indication of LRTC in our S/F/S Josephson junctions. According to the theory, such spin-triplet correlations are known to generate in a system only in the presence of magnetic inhomogeneities [9, 8]. In the absence of magnetic inhomogeneities, only spin-singlet and short-range triplet correlations exist which cause the critical current to decay and oscillate on a length scale given by  $\xi_F^{Singlet} = \sqrt{\hbar D/E_{ex}}$  in the dirty limit. Because of the large exchange energy,  $E_{ex}$ , this length scale is only of order of a few nanometers. However, if the system has magnetic inhomogeneities, then apart from the singlet correlations, long range triplet correlations can be induced. These LRTC correlations are known to decay (without oscillations) on a length scale given by  $\xi_F^{Triplet} = \sqrt{\hbar D/2\pi kT}$  in the dirty limit. Since this length scale is independent of  $E_{ex}$ , and is only governed by the temperature, this causes the critical current to exist for a length scale as long as few hundreds of nanometers at low enough temperatures.

## 7.2 Overview of Our Work

During the initial stages of the project, it was important for us to separate the fabrication challenges from the real physics problems. A well known CuNi-based Josephson junction served as our working template during the fabrication stage. After gaining sufficient confidence in our fabrication technique, we ventured into this field by creating S/F/S Josephson junctions using a weakly ferromagnetic PdNi alloy as the F-layer. Our junctions showed an oscillatory short length decay of the critical current as a function of PdNi thickness. This short length oscillatory decay was indicative of spin singlet correlations in our junction. The lack of LRTC in this experiment was attributed to a short spin memory length in PdNi alloy, measured later in a separate GMR experiment. Our further efforts in this field therefore concentrated on working with strong ferromagnets which are known to have a long spin memory length. As soon as we started working on Josephson junctions using strong ferromagnets, we realized that the large flux contribution from strong ferromagnets made it impossible to get an accurate measure of the maximum critical current. We therefore decided to use them in a SAF configuration. A separate experiment was therefore conducted by my colleague Mazin using Co/Ru/Co as a SAF layer in a Josephson junction. The results of his measurement also showed a short length decay of the critical current as a function of Co layer thickness. We suspected lack of inhomogeneities as a possible reason behind the lack of LRTC in this experiment.

At this point we realized that the ferromagnetic materials helpful for the generation of LRTC may or may not support its long range propagation. A new device was therefore designed where the role of LRTC generation was assigned to a thin ferromagnetic X layer placed close to the Nb interface, and a central SAF layer consisting of a Co/Ru/Co trilayer, because of the virtue of long spin memory length in Co, was used for the long range propagation of thus generated LRTC. Our resulting

junction was a multilayer of the form Nb/Cu/X/Cu/Co/Ru/Co/Cu/X/Cu/Nb. We observed that our junctions with X=PdNi layer showed a huge enhancement in the critical current over the junctions without the X-layer, thus confirming the generation of triplet correlations as a result of an added PdNi layer. A similar effect was seen when Mazin replaced PdNi alloy with a CuNi alloy [108].

### 7.3 Future Directions

After the successful observation of triplet correlations in our experiment, much of our research efforts were directed towards understanding the exact mechanism behind the generation of long range triplet correlations in our experiment. As discussed in Chapter 6, we speculate two possible sources of non-collinear magnetization in our junctions. 1) Non-collinear magnetization experienced by the Cooper pairs in the PdNi layer, 2) Non-collinear magnetization experienced by the Cooper pairs in between the PdNi and the Co layer.

It is possible that the out-of-plane magnetic anisotropy and the small scale domain structure in the PdNi (or CuNi) alloy are the key ingredients providing the non-collinear magnetization that lead to the generation of LRTC in our experiment. To rule out this possible role of PdNi (or CuNi) alloy, we decided to replace PdNi layer with a strong ferromagnet such as Ni or Co. These strong ferromagnets, apart from having a large scale domain structure, are also known to have in-plane magnetization. Currently Caroline Klose, a summer visiting student from Germany, has started working on this problem. The S/F/S Josephson junctions of the form of Nb/Cu/X/Cu/Co/Ru/Co/Cu/X/Nb, with X=Ni are currently being measured in the lab. In the past, the flux contribution from the strong F-layer had led to destruction of the Fraunhofer pattern, however, we believe that if the Ni layer is kept thin, the large destructive flux contribution can be avoided. Another way to avoid the large

flux contribution, is to use a SAF multilayer as the X-layer rather than using a strong F-layer. With this issue in focus, Caroline will also be working on S/F/S Josephson junctions using  $\text{Co}(t_{\text{Co}})/\text{Ru}/\text{Co}(t_{\text{Co}})$  as a X-layer, where  $t_{\text{Co}}$  is the thickness of the Co layer. If Caroline observes LRTCs in her samples, it would be a strong indication refuting PdNi or CuNi alloy as the sole generators of the LRTC in our experiment. In that case, our second speculation, the non-collinearity experienced by the Cooper pairs in between the X layer and the Co layer holds a strong ground.

Another way to ameliorate the effect of non-uniformity introduced by PdNi alloy is to magnetize the PdNi-layer by applying a large in-plane magnetic field. This will decrease the magnetic inhomogeneities arising in the structure due to the out-of-plane magnetic component. The central Co/Ru/Co layer being strongly exchange coupled is known to remain unaffected by fields as large as 5 kOe. We plan to do a systematic study of magnetized Josephson junctions by varying the magnetizing fields, and measuring the resultant change in the maximum critical current of the junction.

My colleague Mazin has been working on Josephson junctions similar to the ones mentioned above, but with Co-platelets as the X-layer. The Co-platelets are formed as result of deposition of extremely thin Co/Cu multilayers, so that the Co-atoms interdispersed in the Cu form Co-platelets. It would be interesting to see if such an unusual configuration can lead to the generation of triplet correlations in the system.

Another group member William Martinez is working on making the triplet samples using a lateral geometry. He will be making samples identical to our triplet samples described in Chapter 6, however, instead of using antiferromagnetically coupled Co-layers to reduce the flux in the junction, his geometry implements the use of a thin narrow Co wire in order to reduce flux. One can therefore expect to see an ideal Fraunhofer pattern for his samples even for longer Co lengths. As indicated in Chapter 6, section 1.4.3, our attempts to measure the temperature dependence of

the critical current were restricted to the short-regime because of the destruction of the Fraunhofer pattern for thicker Co-layers; we believe that William's geometry will allow such measurement in the long regime. Additionally, this sample geometry will also help Bill to measure the temperature dependence of the resistance.

Apart from knowing the microscopic origin of triplet correlations in our experiment and finding the different X materials that can generate long range triplet correlations, a new Birge group member Kurt Boden is also working on measuring the density of states (DOS) of the samples with triplet correlations, using tunneling spectroscopy.

## 7.4 A Year of Triplet Correlations!

Apart from our experiment, this year saw several other publications in this field. It is several years since Keizer *et al.* [10] reported the evidence of triplet correlations in CrO<sub>2</sub> based Josephson junction that the Aarts group in Leiden finally decided to revisit the problem [109]. Their experiments confirm the observation of triplet correlations in CrO<sub>2</sub> based Josephson junctions. However, the authors of this paper also indicate a low success of their junctions, attributing it to the complicated nature of CrO<sub>2</sub> that is sensitive to the growth conditions. Interestingly another group at Penn State also reported an observation of proximity induced superconductivity in Co-nanowires [110] that are hundreds of nm long. Similar evidence for triplet superconductivity in Josephson junctions with ferromagnetic Cu<sub>2</sub>MnAl-Heusler [111] barriers was also reported recently. All these experiments support the generation of proximity-induced long-range triplet correlations in S/F systems. It really nice to see so many positive results in this field after a long time.

# Appendix A

## Appendices

### A.1 Photolithography Recipes

This section will describe various ways of doing optical lithography, also known as photolithography. The basic process involves coating the substrate with a photosensitive material called photoresist. The resist is then baked at a certain temperature that drives out the solvent from it and makes it photosensitive. It is then selectively exposed using a mask. If the resist used is a positive photoresist, the exposed resist can be dissolved in a developer thus leaving the unexposed resist features on the sample. Instead if it is a negative photoresist, the unexposed resist can be dissolved in the developer thus leaving the exposed resist features on the sample. The mostly widely used S1800 series resist is a positive tone photoresist.

Every resist attenuates the light passing through it so that the top layer develops faster than the bottom resist. This causes the sidewalls of positive resist to have positive slope (80/90 degrees) unless special techniques are used. The use of chlorobenzene in single layer photolithography, LOR (lift-off resist) layer in bilayer photolithography, a metal layer in trilayer photolithography, or using a special image reversal (IR) resist AZ 5214-E ensures either a well defined sharp undercut or a

negative sloped resist profile.

This section will give recipes for different kinds of photolithography techniques used during the course of this work.

### A.1.1 Single Layer Photolithography

Single layer photolithography is the fastest of all the processes described here. Obtaining a guaranteed, well-defined large undercut is difficult using this process. The undercut obtained using this method is nominal and it strongly relies on having a good contact between the substrate and the mask as well as a the exposure timing. Since the desired features needed were relatively large (10-80  $\mu\text{m}$ ) compared to the minimum features sizes possible using the photolithography process (1-2  $\mu\text{m}$ ), using a higher exposure time ensured sufficient exposure of the resist without compromising on the expected dimensions.

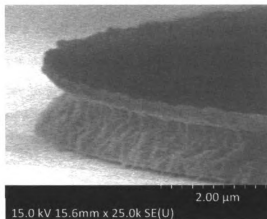


Figure A.1: SEM image of a resist pillar obtained using single layer photolithography

1. Spin coat S1813 resist at 5000 RPM for 40 sec.
2. Bake it at 100°C on hotplate for 1.5 min or 95°C in oven for 45 minutes.
3. UV expose with a mask for 10 sec.

4. Soak in chlorobenzene for 5 min and rinse with DI water.
5. Bake it at 95°C on hotplate for 1 min.
6. Develop in Microposit 352/452 for about 30-45 sec and rinse it with DI water.

*Important note:* In order to increase the robustness of photoresist against the harsh ion milling process, the sample with photoresist features was baked on hotplate for 2 min at 95°C and flood exposed for ~ 100 sec.

### **A.1.2 Bilayer Photolithography**

A bilayer photolithography process uses two different kinds of photoresist. Since the solvent liquids in the two resists are different, the layers don't intermix and can be treated independently. The bottom layer of resist is Lift-Of-Resist (LOR). As the name suggests, this resist does not need an UV exposure for its development. The second/top layer can be a resist of user's choice. We have worked with both S1813 and S1805. The development time of LOR resist is sensitive to its bake temperature; higher bake temperatures yield slower development rate.

It was found that LOR is sensitive to the ion milling process even when it was protected by the top resist. It is therefore advised that this resist should not be used as a ion mill mask; it can but be safely used for metallization processes. This photolithography process therefore had to be ruled out in our experiments.

1. Spin coat the substrate with LOR-5A at 5000 RPM for 40 sec.
2. Bake in oven at 170°C for 45 min.
3. Spin coat S1813 at 3000 RPM for 40 sec.
4. Bake in oven at 95°C for 30 min.

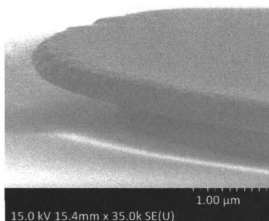


Figure A.2: SEM image of a resist pillar obtained using bilayer photolithography. The bottom layer is Lift off resist (LOR) and the top layer is a S1805 resist.

5. UV expose the pattern for 10 sec.
6. Develop in Microposit 352/452 for about 20-30 sec and rinse it with DI water.

### A.1.3 Trilayer Photolithography

The resist survival posed a big problem with the large undercuts obtained in the bilayer lithography process. A trilayer photolithography process was therefore optimized to get large undercuts. This process implements use of S1800 series resist as the top and the bottom layer, where the layers themselves are separated by a thin metallic Au layer. The scheme takes into consideration the fact that the solvents of top and bottom layer being same, a thick enough Au layer can be used to avoid the intermixing of the two layers.

1. Spin coat the substrate with S1813 at 5000 RPM for 40 sec. This acts as layer-1.
2. Bake on hotplate at 100°C for 1.5 min or in oven at 95°C for 45 min.
3. Flood expose the resist for 4.5 sec.
4. Evaporate 10 nm Au. This acts as layer-2.

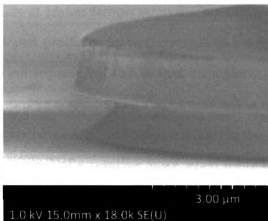


Figure A.3: SEM image of a resist pillar obtained using trilayer photolithography. The two layers of resist (S1813) is separated by a 10 nm of Au layer.

5. Spin coat the substrate with S1813 at 5000 RPM for 40 sec. This acts as layer-3
6. Bake on hotplate at 100°C, for 1.5 min or in oven at 95°C for 45 min.
7. UV expose the pattern for 4.5 sec.
8. Develop in Microposit 352/452 for about 30 sec and rinse it with DI water. This develops the layer-3.
9. Etch the exposed Au using Standard Gold Etchant ( $KI+I_2+H_2O$ ). This removes layer-2.
10. Develop in Microposit 352/452 for about 30 sec and rinse it with DI water. This develops the bottom layer, layer-3.

#### A.1.4 Image Reversal Photolithography

Since every resist attenuates the light passing through it, it is hard to obtain a negative resist profile or a sharp undercut unless one the the above techniques are implemented. But this very disadvantage can be turned into an advantage if one uses an image reversal technique. Image reversal process uses a special kind of positive tone resist

which after a second bake at higher temperature can act like a negative tone resist. It reverses the positive sloped profile to leave the opposite—a negative sloped profile on the sample. A natural consequence of this is that an underexposure which normally causes a positive resist profile now acts as an advantage when using an image reversal process. This is can also be clearly understood from Figure A.4. This also meant using a negative mask instead of a positive mask when using image reversal process.

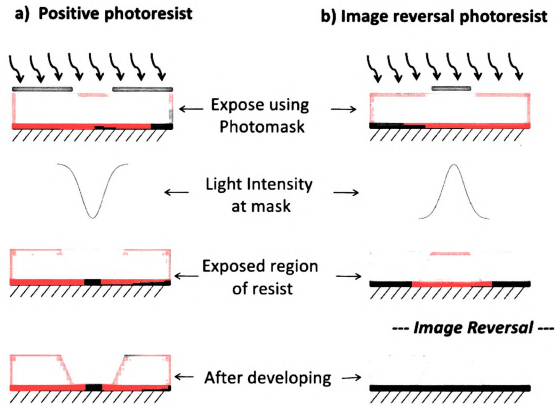


Figure A.4: A comparison of how the light attenuation in resist layer can be used to advantage in an image reversal process.

1. Spin coat AZ 5214-E at 4000 RPM, 40 sec.
2. Bake on hotplate at 95°C for 1 min.
3. UV expose the pattern using a dark-field mask for 2.5 sec. [An underexposure

in this step gains a large negative slope in the resist profile!]

4. Bake on hotplate at 120°C for 1.5 min.
5. Flood expose the substrate for 20 sec.
6. Develop AZ Developer 352 for 40 sec and rinse it with water.

Of all the methods given above, it was found that the bilayer method was incompatible with our process. Of all the methods studied here, the trilayer photolithography process gave the largest undercuts. Nevertheless because the trilayer method was the most time consuming method, we preferred to work with a single layer method or sometimes an image reversal method.

# BIBLIOGRAPHY

- [1] J. Bardeen, L. Cooper, and J. Schrieffer, Phys. Rev. **108**, 1175 (1957).
- [2] J. G. Bednorz and K. A. Muller, Z. Phys. B **64** (2), 189 (1986).
- [3] I. Eremin, D. Manske, S. G. Ovchinnikov, and J. F. Annett, Ann.Phys-Berlin **13**, 149 (2004).
- [4] V. Berezinskii, JETP Lett. **20** (9), 287 (1974).
- [5] M. Giroud, H. Courtois, K. Hasselbach, D. Mailly, and B. Pannetier, Phys. Rev. B **58**, R11872 (1998).
- [6] M. Lawrence and N. Giordano, J.Phys: Cond. Matt. **11**, 1089 (1999).
- [7] V. Petrashov, I. Sosnin, I. Cox, A. Parsons, and C. Troadec, Phys. Rev. Lett. **83**, 3281 (1999).
- [8] F. Bergeret, A. Volkov, and K. Efetov, Phys. Rev. Lett. **86**, 4096 (2001).
- [9] A. Kadigrobov, R. Shekhter, and M. Jonson, Europhys. Lett. **54**(3), 394 (2001).
- [10] R. S. Keizer, S. Goennenwein, T. Klapwijk, G. Xiao, and A. Gupta, Nature (London) **439**, 825 (2006).
- [11] F. Bergeret, A. Volkov, and K. Efetov, Rev. Mod. Phys. **77**, 1321 (2005).
- [12] H. Kamerlingh-Onnes, Comm. Phys. Lab. Univ. Leiden **122**, **124**, (1911).
- [13] G. Deutscher and P. de Gennes, in *Superconductivity*, edited by R. Parks (Marcel Dekker, Inc., New York, 1969), Vol. 2, p. 1005.
- [14] E. Demler, G. Arnold, and M. Beasley, Phys. Rev. B **55**, 15174 (1997).
- [15] M. Velez, M. Cyrille, S. Kim, J. Vincent, and I. Schuller, prb **59**, 14659 (1999).
- [16] Y. Obiand, M. Ikebe, T. Kubo, and H. Fujimori, Physica C **317-318**, 149 (1999).
- [17] T. Muhge, N. Garif'yanov, Y. Goryunov, G. Khaliullin, L. Tagirov, K. Westerholt, I. Garifullin, and H. Zabel, Phys. Rev. Lett. **77**, 1857 (1996).

- [18] C. Strunk, C. Surgers, U. Paschen, and H. Löhneysen, *Phys. Rev. B* **49**, 4053 (1994).
- [19] H. K. Wong, B. Jin, H. Q. Yang, J. B. Ketterson, and J. E. Hillard, *J. Low Temp. Phys.* **63**, 307 (1986).
- [20] J. Jiang, D. Davidovic, D. Reich, and C. Chien, *Phys. Rev. Lett* **74**, 314 (1995).
- [21] V. Ryazanov, V. Oboznov, A. Rusanov, A. Veretennikov, A. Golubov, and J. Aarts, *Phys. Rev. Lett.* **86**, 2427 (2001).
- [22] Y. Blum, A. Tsukernik, M. Karpovski, and A. Palevski, *Phys. Rev. Lett.* **89**, 187004 (2002).
- [23] T. Kontos, M. Aprili, J. Lesueur, F. Genêt, B. Stephanidis, and R. Boursier, *Phys. Rev. Lett.* **89**, 137007 (2002).
- [24] H. Sellier, C. Baraduc, F. Lefloch, and R. Calemczuk, *Phys. Rev. B* **68**, 054531 (2003).
- [25] A. Bauer, J. Bentner, M. Aprili, M. L. D. Rocca, M. Reinwald, W. Wegscheider, and C. Strunk, *Phys. Rev. Lett.* **92**, 217001 (2004).
- [26] V. Oboznov, V. Bol'ginov, A. Feofanov, V. Ryazanov, and A. Buzdin, *Phys. Rev. Lett.* **96**, 197003 (2006).
- [27] J. Robinson, S. Piano, G. Burnell, C. Bell, and M. G. Blamire, *Phys. Rev. Lett.* **97**, 177003 (2006).
- [28] J. Robinson, S. Piano, G. Burnell, C. Bell, and M. G. Blamire, *Phys. Rev. B* **76**, 094522 (2007).
- [29] M. Weides, M. Kemmler, E. Goldobin, D. Koelle, R. Kleiner, H. Kohlshedt, and A. Buzdin, *Appl. Phys. Lett.* **89**, 122511 (2006).
- [30] A. Bannykh, J. Pfeiffer, V. Stolyarov, I. Batov, V. Ryazanov, and M. Weides, *Phys. Rev. B* **79**, 054501 (2009).
- [31] T. Kontos, M. Aprili, J. Lesueur, and X. Grison, **86**, 304 (2001).
- [32] I. Sosnin, H. Cho, V. Petrashov, and A. Volkov, *Phys. Rev. Lett.* **96**, 157002 (2006).
- [33] Y. V. Fominov, A. F. Volkov, and K. B. Efetov, *Phys. Rev. B* **75**, 104509 (2007).
- [34] F. Volkov and K. B. Efetov, *Phys. Rev. B* **78**, 024519 (2008).
- [35] A. F. Volkov, A. Anishchanka, and K. B. Efetov, *Phys. Rev. B* **73**, 104412 (2006).

- [36] T. Champel, T. Lofwander, and M. Eschrig, Phys. Rev. Lett. **100**, 077003 (2008).
- [37] G. B. Halasz, J. W. A. Robinson, J. F. Annett, and M. G. Blamire, Phys. Rev. B **79**, 224505 (2009).
- [38] M. Alidoust, J. Linder, G. Rashedi, T. Yokoyama, and A. Sudbo, Phys. Rev. B **81**, 014512 (2010).
- [39] A. Volkov, F. Bergeret, and K. Efetov, Phys. Rev. Lett. **90**, 117006 (2003).
- [40] Y. Asano, Y. Sawa, Y. Tanaka, and A. A. Golubov, Phys. Rev. B **76**, 224525 (2007).
- [41] M. Eschrig, J. Kopu, J. C. Cuevas, and G. Schon, Phys. Rev. Lett. **90**, 137003 (2003).
- [42] A. V. Galaktionov, M. S. Kalenkov, and A. D. Zaikin, Phys. Rev. B **77**, 094520 (2008).
- [43] M. S. Kalenkov, A. V. Galaktionov, and A. D. Zaikin, Phys. Rev. B **79**, 014521 (2009).
- [44] A. Cottet, D. Huertas-Hernando, W. Belzig, and Y. V. Nazarov, Phys. Rev. B **80**, 184511 (2009).
- [45] J. Linder and A. Sudb, Phys. Rev. B **76**, 064524 (2007).
- [46] G. Eilenberger, Z. Phys. **B214**, 195 (1968).
- [47] K. Usadel, Phys. Rev. Lett. **25**, 507 (1970).
- [48] A. Buzdin, Rev. Mod. Phys. **77**, 935 (2005).
- [49] A. Volkov and K. Efetov, Phys. Rev. B **81**, 144522 (2010).
- [50] L. Trifunovic and Z. Radovic, arXiv:1005.1867v1 .
- [51] F. Bergeret, A. Volkov, and K. Efetov, Phys. Rev. Lett. **86**, 3140 (2001).
- [52] Crouzy, S. Tollis, and D. A. Ivanov, Phys. Rev. B **75**, 054503 (2007).
- [53] I. B. Sperstad, J. Linder, and A. Sudbo, Phys. Rev. B **78**, 104509 (2008).
- [54] M. Houzet and A. I. Buzdin, Phys. Rev. B **76**, 060504(R) (2007).
- [55] J. Clarke and A. I. Braginski, *SQUID Handbook: Fundamentals and Technology of SQUIDs and SQUID Systems (Vol. 1)* (Wiley-VCH Verlag GmbH & Co. KGaA, Weinheim, Germany, 2004).

- [56] A. Barone and G. Paterno, *Physics and Applications of the Josephson Effect* (John Wiley & Sons, Inc., ADDRESS, 1982).
- [57] L. Bulaevskii, V. Kuzii, and A. Sobyenin, *JETP Lett.* **25**, 290 (1977).
- [58] I. Moraru, Ph.D. thesis, Michigan State University, USA, 2006.
- [59] A. Sharma, Ph.D. thesis, Michigan State University, USA, 2008.
- [60] J. C. Ododo and B. R. Coles, *J. Phys. F* **7**, 2393 (1977).
- [61] V. Ryazanov, *Physics-Uspekhi* **42**, 825 (1999).
- [62] M. Faure, A. Buzdin, A. Golubov, and M. Kupriyanov, *Phys. Rev. B* **73**, 064505 (2006).
- [63] F. Bergeret, A. Volkov, and K. Efetov, *Phys. Rev. B* **68** (6), 064513 (2003).
- [64] A. Bauer, J. Bentner, M. Aprili, M. L. D. Rocca, M. Reinwald, W. Wegscheider, and C. Strunk, *Phys. Rev. Lett.* **92**, 2004 (2004).
- [65] K. Matsuda, H. Niwa, Y. Akimoto, T. Uemura, and M. Yamamoto, *IEEE Trans. Applied Superconductivity.* **17**(2), (2007).
- [66] C. Cirillo, S. Prischepa, M. Salvato, and C. Attanasio, *Journal of Physics and Chemistry of Solids* **67**, 412 (2006).
- [67] C. Cirillo, J. Aarts, and C. Attanasio, *Phys. Stat. Sol. (c)* **3** **9**, 3015 (2006).
- [68] C. Cirillo, S. L. Prischepa, M. Salvato, C. Attanasio, M. Hesselberth, and J. Aarts, *Phys. Rev. B* **72**, 144511 (2005).
- [69] J. Beille, Ph.D. thesis, Université Joseph Fourier, Grenoble, USA, 1975.
- [70] T. Kontos, Ph.D. thesis, Université Paris XI, Orsay, France, 2002.
- [71] A. Ruotolo, C. Bell, C. Leung, and M. Blamire, *Journal of Applied Physics* **96** (1), (2004).
- [72] I. Veshchunov, V. Oboznov, A. Rossolenko, A. Prokofiev, L. Vinnikov, A. Rusanov, and D. Matveev, *Pis'ma Zh. Eksp. Teor. Fiz.* **88**, 873 (2008).
- [73] V. Shelukhin, A. Tsukernik, M. Karpovski, Y. Blum, K. Efetov, A. Volkov, T. Champel, M. Eschrig, T. Löfwander, G. Schön, and A. Palevski, *Phys. Rev. B* **73**, 174506 (2006).
- [74] A. Buzdin, B. Bujicic, and B. M. Y. Kupriyanov, *Sov. Phys. JETP* **74**, 124 (1992).
- [75] O. Kashuba, Y. Blanter, and V. Falko, *Phys. Rev. B* **75**, 132502 (2007).

- [76] J. Bass, *Metals: Electronic Transport Phenomena* (Landolt-Börstein Tables, New Series, **III/15a**, pp. 1-288, Springer-Verlag (1982), ADDRESS, 2000).
- [77] F. Pinski, P. Allen, and W. Butler, *Phys. Rev. B* **23**, 5080 (1981).
- [78] J. Vuillemin, *Phys. Rev.* **144**, 396 (1966).
- [79] D. Dye, S. Campbell, G. Crabtree, J. Ketterson, N. Sandesara, and J. Vuillemin, *Phys. Rev. B* **23**, 462 (1981).
- [80] I. Mazin, E. Savitskii, and Y. Uspenskii, *J. Phys. F: Met. Phys.* **14**, 167 (1984).
- [81] S. Frolov, D. V. Harlingen, V. Oboznov, V. Bolginov, and V. Ryazanov, *Phys. Rev. B* **70**, 144505 (2004).
- [82] T. Valet and A. Fert, *Phys. Rev. B* **48**, 7099 (1993).
- [83] M. Baibich, J. Broto, A. Fert, F. N. V. Dau, and F. Petroff, *Phys. Rev. Lett.* **61**, 1988 (1988).
- [84] G. Binasch, P. Grnberg, F. Saurenbach, and W. Zinn, *Phys. Rev. B* **39**, 4828 (1989).
- [85] S.-F. Lee, W. Pratt, Q. Yang, P. Holody, R. Loloee, P. Schroeder, and J. Bass, *J. Magn. Mater.* **118**, L1, (1993).
- [86] S. Zhang and P. Levy, *J. Appl. Phys.* **69**, 4786 (1991).
- [87] H. Arham, T. Khaire, R. Loloee, W. Pratt, and N. Birge, *Phys. Rev. B* **80**, 174515 (2009).
- [88] J. Nogués and I. Schuller, *J. Magn. Mater.* **192**, 203 (1999).
- [89] C. Moreau, I. Moraru, N. Birge, and W. Pratt, *Appl. Phys. Lett.* **90**, 012101 (2007).
- [90] L. Khoi, P. Veillet, and I. Campbell, *J. Phys. F* **6**, L (1976).
- [91] S. Senoussi, I. Campbell, and A. Fert, *Sol. St. Comm.* **21**, 269 (1977).
- [92] N. Spaldin, *Magnetic Materials: Fundamentals and Device Applications* (Cambridge University Press, ADDRESS, 2003).
- [93] Z. Wang, H. Kunkel, and G. Williams, *J. Phys.: Condens. Matter* **4**, 10385 (1992).
- [94] A. Reilly, W. Chiang, W. Park, S. Hsu, R. Loloee, S. Steenwyk, W. Pratt, and J. Bass, *IEEE Trans. Mag.* **34(4)**, 939 (1998).
- [95] L. Piraux, S. Dubois, C. Marchal, J. M. Beuken, L. Filipozzi, J. F. Despres, K. Ounadjela, and A. Fert, *J. Mag. Magn. Mat.* **156**, 317 (1996).

- [96] M. Khasawneh, W. Pratt, and N. Birge, *Phys. Rev. B* **80**, 020506(R) (2009).
- [97] O. Bouregois, P. Gandit, J. Lesueur, A. Sulpice, X. Grison, and J. Chaussy, *Eur. Phys. J. B* **21**, 75 (2001).
- [98] S. Parkin, N. More, and K. Roche, *Phys. Rev. Lett.* **64**, 2304 (1990).
- [99] C. F. Majkrzak, J. W. Cable, J. Kwo, M. Hong, D. B. McWhan, Y. Yafet, J. V. Waszczak, and C. Vettier, *Phys. Rev. Lett.* **56**, 27002703 (1986).
- [100] Y. M. Blanter and F. W. J. Hekking, *Phys. Rev. B* **69**, 024525 (2004).
- [101] J. Borchers, J. Dura, J. Unguris, D. Tulchinsky, M. Kelley, C. Majkrzak, S. Hsu, R. Loloee, W. Pratt, and J. Bass, *Phys. Rev. Lett.* **83**(13), 2796 (1999).
- [102] K. Eid, D. Portner, J. Borchers, R. Loloee, M. Darwish, M. Tsoi, R. Slater, K. O'Donovan, W. Kurt, W. Pratt, and J. Bass, *Phys. Rev. B* **65**(2), 054424 (2002).
- [103] T. Khaire, W. Pratt, and N. Birge, *Phys. Rev. B* **79**, 094523 (2009).
- [104] J. Gu, C.-Y. You, J. Jiang, J. Pearson, Y. Bazaliy, and S. Bader, *Phys. Rev. Lett.* **89**, 267001 (2002).
- [105] T. Koikeda, K. Suzuki, and S. Chikazumi, *Appl. Phys. Lett.* **4**, 160 (1964).
- [106] M. Lawrence and J. H. Giordano, *J. Phys.: Condens. Matter* **11**, 1089 (1999).
- [107] V. Pea, Z. Sefrioui, D. Arias, C. Leon, and J. Santamaria, *Phys. Rev. B* **69**, 224502 (2004).
- [108] T. Khaire, M. Khasawneh, W. Pratt, and N. Birge, *Phys. Rev. B* **104**, 137002 (2010).
- [109] M. S. Anwar, M. Hesselberth, M. Porcu, and J. Aarts, arXiv:1003.4446v1 (2010).
- [110] J. Wang, M. Singh, M. Tian, N. Kumar, B. Liu, C. Shi, J. K. Jain, N. Samarth, T. E. Mallouk, and M. H. W. Chan, *Nature Phys.* **6**, 389 (2010).
- [111] D. Sprungmann, K. Westerholt, H. Zabel, M. Weides, and H. Kohlstedt, arXiv:1003.2082 (2010).

MICHIGAN STATE UNIVERSITY LIBRARIES



3 1293 03063 7312